Investigations of Different Methods to Promote Drug Mixing in the Eye

Thesis by
Jinglin Huang

In Partial Fulfillment of the Requirements for the
Degree of
Doctor of Philosophy

CALIFORNIA INSTITUTE OF TECHNOLOGY
Pasadena, California

2020
Defended September 25th, 2019

© 2020

Jinglin Huang
ORCID: 0000-0003-0760-4950

All rights reserved

ACKNOWLEDGEMENTS

Years at Caltech have changed me a lot in many ways. The pursuit of my PhD degree was only possible with the support and assistance from the Caltech faculty, scientists, engineers, friends, and family. There are many people that I would like to thank.

First and foremost, I would like to acknowledge my advisor, Professor Morteza Gharib. He is always warm, supportive, and funny sometimes. I am very grateful for his help throughout the time at Caltech. It has been a great privilege to work with him. His inspiring ideas always guide me to think outside of box, and his fantastic scientific intuition is extremely precious. I have received enough guidance as well as sufficient freedom during my PhD to explore subjects that I'm interested in. What I learned from him is far beyond the knowledge of fluid dynamics. In addition to his academic guidance, he has supported me during the emotionally tough times and gave me moral support. I wish one day I could be a mentor like him.

I want to express my sincere gratitude to my thesis advising committee, Professor Yu-Chong Tai, Professor Wei Gao, Professor Dan Schwartz, and Professor Danny Petrasek, for the time they dedicated to my thesis and research progress. I would also like to thank Professor Choo and Professor Tim Colonius for their great insights during our discussions.

I am fortunate to have joined the Gharib Research Group with a group of wonderful people. Thank you Cong, Chris, and Nathan for all your help along the way.

It's an honor for me to have joined the Medical Engineering as the first class with three other amazing engineers. We worked together for classes and fought through qualification exams. Thank you Colin, Di, and Alessandro for cheering for my every single achievement, small or big, and keeping me accompanied during the tough times.

I want to thank my parents and Yu Su for always being on my side. Thank you for always supporting me in whichever path I choose to take and inspiring me to keep pursuing my passions. I am very grateful for all your love, understanding, and encouragement. I love you all.

In the end, I would like to thank the Resnick Institute at Caltech for making it possible for me to explore subjects outside of Medical Engineering. During my two years of research work on ocean desalination, I met a lot of great people and learned a lot about sustainability science.

ABSTRACT

Age-related macular degeneration (AMD) is the leading cause of central vision loss in the developed world. In the case of wet AMD, it can be managed through serial intravitreal injections of anti-vascular endothelial growth factor (anti-VEGF) agents. However, sometimes the treatment is ineffective. Given that half-life time of the drug is limited, one possible cause of the ineffective treatment is inefficient drug mixing in the eye. Here, we focus on the understanding of drug mixing in vitreous chamber and parameters that could potentially influence mixing profiles. Both movement-driven method and thermal-driven method are explored. The in-vitro study outcomes will not only be useful for achieving fundamental understandings of fluid dynamics in the eye, but also helpful in developing a better strategy for intravitreal injection and improving the quality of care for patients.

TABLE OF CONTENTS

Acknowledgements iii
Abstract v
Table of Contents vi
List of Illustrations vii
List of Tables xiv
Chapter I: Introduction 1
1.1 Background 1
1.2 Organization of the thesis 8
Chapter II: Drug Delivery in The Eye Under Lateral Movements 9
2.1 Introduction 9
2.2 Experimental Design Methods 14
2.3 Results 24
2.4 Discussion 38
Chapter III: Thermal Effects on Fluid Mixing in the Eye 43
3.1 Introduction 43
3.2 Materials and Methods 45
3.3 Results 52
3.4 Discussion 86
Chapter IV: Conclusion and Future Works 95
Bibliography 97

LIST OF ILLUSTRATIONS

Number *Page*

1.1 Anatomy of the eye (figure adapted from verywellhealth.com) The solid arrow indicates the space filled with vitreous humor; the dashed arrow indicates the typical location of macula. 2

1.2 A typical image that a patient with AMD disease sees (figure adapted from Bausch.com) As it is shown in the image, the patient would experience blurred vision, and a dark spot in the center of the vision, as well as distortion of straight lines. 3

1.3 Intravitreal injection procedure (Source: Karl Brasse, MD, Eyeland Design) Drugs injected into the vitreous chamber exit near the front of the eye. 3

1.4 wo drug elimination routes for drug in vitreous chamber: anterior (left) vs posterior (right) Maurice and Mishima, 1984 Anterior route (labeled in blue) is for drugs to diffuse in the vitreous to enter aqueous humor and then reach the blood stream; posterior route (numbered in 2, 3, and 4) is for drugs to diffuse in the vitreous and then cross the blood-retinal and blood-aqueous barriers. 4

1.5 Diffusion coefficients of molecules and particles in the vitreous. (Source (Del Amo Eva et al., 2017)) 6

1.6 Schematic drawings of various drug delivery methods for treatment of AMD (Holz, Schmitz-Valckenberg, and Fleckenstein, 2014) The target area (macula) can be reached by administrations via various routes: topical delivery to the surface of the eye, trans-scleral delivery underneath the conjunctiva, direct injection (injection or implant), and systematical delivery via oral tablets. 7

2.1 Variations in concentrations in the vitreous ((Purves et al., 2001)) As it is demonstrated in the figure, hyaluronic acid and collagen are not uniformly distributed within the vitreous. The highest concentration is in vitreous cortex, which is the region that is the closest to retina. The central area (central vitreous) is more liquid like, followed by basal vitreous. 10

2.2 Anatomy of eye Note that 3 to 4 mm posterior to limbus is very close to the front of the eye. 13
2.3 Desired voluntary lateral movement in this study (Picture (a) demonstrates an eye looking to the left and the orange arrow indicates the center of the eye globe in (a); Picture (b) demonstrates the eye looking to the right and the green arrow indicates the center of the eye globe in (b); During this voluntary lateral movement, the eye moves back and forth between left (a) and right (b) at 1 Hz. The sweep angle is 45 degree, which is demonstrated in (c)) 15
2.4 Eye model in our study Fabricated at Caltech glass shop. The diameter is 1 inch. 16
2.5 Various injection sites (The orange arrow represents needle tip; the front of the eye is labeled in (a) and will be the same for (b) and (c)) . 17
2.6 Schematic Demonstration of PIV Visualization Setup (from left to right: direction of rotation, the eye model mounted on top of a motor, a concave lens, and a laser.) 19
2.7 Actual PIV Visualization Setup (from left to right: motor-magnet coupler with the eye model, a concave lens, and a laser) 20
2.8 Motor-Magnet Coupler Setup (The four orange columes indicate the positions of the four magnets; the eye model (sphere) sits on the top is immersed in a water tank. 22
2.9 Example of a plot of the actual motor trajectory (5 cycles rotations) . 22
2.10 Example of an image captured during a PIV visualization session . . 25
2.11 Average Velocity Field Obtained from PIV analysis (5 cycles) 25
2.12 First Sets of Vorticity Plots: 5 cycles vs 10 cycles (Note these were taken right after the movements stopped) 26
2.13 PIV analysis can generate a series of files that contain flow property information in a sequential manner 28
2.14 Detailed explanation of pathline visualization algorithms (Blue circles indicates particles at different instances of time.) 28
2.15 Particle pathline demonstration (The beginning of the time is color-coded in dark blue, then green, and finally light blue) 29
2.16 Four circulations and one in each quadrant 30
2.17 Dye visualization images from varying injection sites (From top to bottom: bottom injection, center injection, and side injection) 32

2.18 Dye visualization images (It shows observations over the course of 30 mins. Image sequence is taken immediately after injection, the moment after rotation stops, and every 10 mins afterwards.) 34
2.19 Fluorescent particle concentration reaching the target tissue (This quantifies the amount of fluorescein (drugs) that reaches the target tissue over the course of 30 mins after 10 cycles of lateral rotation) . . 34
2.20 Particle pathline tracking after 10 cycles of rotation (glycerol/water mixture) 36
2.21 Particle pathline tracking after a second 10 cycles of rotation (observation continued from2.20 36
2.22 Particle pathline tracking after 200 continuous rotations (Using glycerol/water mixture) 37
2.23 Highlighted particles in the center, bottom, and side regions. (Pink color labels particles in the center region; blue color labels particles in the side and bottom regions) 39
2.24 Demonstration of the simulation methodology (The first velocity field is projected throughout the rest of the instances of time.) 39
2.25 Particle pathline if the circulation doesn't decay (The velocity field is taken from the first instance of time from the PIV analysis results; particle pathline starts from dark blue to green and finally light blue.) 40
3.1 Five heating positions around the eye (Upper, center, and lower positions are defined in terms of a person sitting upright; the heads-up position simulates the scenario of a person who lays on the chair with his/her head facing upwards, whereas the heads-down position means the opposite. 44
3.2 Key components of the heating source (There are three major components: the solid blue part represents the steel stick; the yellow part represents polyimide flexible heater which sits on top of the steel stick, the two cables are connected to the power box, and the hollow blue part represents the customized aluminum piece.) 46
3.3 Heating element assembly wrapped with black tapes 46
3.4 Heating element at the "center" heating location 47

3.5 Stratified silver-coated particles/glycerol/water mixture The heaviest particles stay at the bottom whereas the lightest ones float in the top region. Only the middle portion is suitable for visualization purpose as particles in this region share approximately the same density with the glycerol/water mixture. 48
3.6 Pixel intensity quantification using the image tool in MATLAB (The purple box highlighted in the picture on the right defines the area of interests for pixel intensity quantification. When fluorescein is excited by the laser, it becomes bright/white in the image. In this image, fluorescein is distributed in the top right region.) 49
3.7 Pathline visualization from 5-celsius temperature difference (center heating) These 100 images were taken from 5 mins to 5 mins and 10 secs. Note that most of the flow behavior was happening on the left half of the eye model. 53
3.8 Pathline visualization from 10-celsius temperature difference (center heating) These 100 images were taken from 5 mins to 5 mins and 10 secs. Note that the flow was stronger compared with the one in Figure 3.7a, although circulation was relatively weak at the very bottom of the eye model. 53
3.9 Pathline visualization from 10-celsius temperature difference (lower heating) These 100 images were taken from 5 mins to 5 mins and 10 secs. Note that circulations were fully activated across all regions in the eye model. 54
3.10 Pathline visualization from 10- Celsius temperature difference (upper heating) These 100 images were taken from 5 mins to 5 mins and 10 secs. Note that most of the flow behavior was happening on the top part of the eye model. 54
3.11 Pathline visualization from 10- Celsius temperature difference (heads-up heating) These 100 images were taken from 5 mins to 5 mins and 10 secs. Note that the overall flow behavior was not quite strong. . . . 55
3.12 Pathline visualization from 10-Celsius temperature difference (heads-down heating) These 100 images were taken from 5 mins to 5 mins and 10 secs. Note that the flow behavior was very strong. It's very hard to describe a distinct pattern from this image. 55
3.13 Pathline visualization before the heat source was applied. These 100 images were taken for a duration of 10 seconds. 56

3.14 Circulation represents the rotational motion of flow in the eye model. Here, we took the absolute value of circulation in each case. 57
3.15 An example of pathline visualization using MATLAB. (The position of heat source is marked in the plot.) 58
3.16 Average vorticity plot from $\delta T = 5$ Celsius (center heating) 59
3.17 Pathline visualization from $\delta T = 5$ Celsius (center heating) 59
3.18 Average vorticity plot from $\delta T = 10$ Celsius (center heating) 60
3.19 Pathline visualization from $\delta T = 10$ Celsius (center heating) 60
3.20 Average vorticity plot from $\delta T = 10$ Celsius (lower heating) 61
3.21 Pathline visualization from $\delta T = 10$ Celsius (lower heating) 61
3.22 Average vorticity plot from $\delta T = 10$ Celsius (upper heating) 62
3.23 Pathline visualization from $\delta T = 10$ Celsius (upper heating) 62
3.24 Average vorticity plot from $\delta T = 10$ Celsius (heads-up) 63
3.25 Pathline visualization from $\delta T = 10$ Celsius (heads-up) 63
3.26 Average vorticity plot from $\delta T = 10$ Celsius (heads-down) 64
3.27 Pathline visualization from $\delta T = 10$ Celsius (heads-down) 64
3.28 Individual particle tracking for $\delta T = 5Celsius$, heating from the center. The blue circle indicates the initial position of the particle; dark blue line indicates particle movements during the first 200 seconds; green line indicates particle movements during the second 200 seconds, and light blue line indicates particle movements during the last 200 seconds. Heating position is marked in red along the circular boundary. 66
3.29 Individual particle tracking for $\delta T = 10Celsius$, heating from the center. The blue circle indicates the initial position of the particle; dark blue line indicates particle movements during the first 200 seconds; green line indicates particle movements during the second 200 seconds, and light blue line indicates particle movements during the last 200 seconds. Heating position is marked in red along the circular boundary. 66

3.30 Individual particle tracking for for $\delta T = 10 Celsius$, heating from the lower position. The blue circle indicates the initial position of the particle; dark blue line indicates particle movements during the first 200 seconds; green line indicates particle movements during the second 200 seconds, and light blue line indicates particle movements during the last 200 seconds. Heating position is marked in red along the circular boundary. 67
3.31 Pixel Intensity Quantification Results from LIF Visualization: Heavier drug and center heating during the first 10 mins. 69
3.32 Pixel Intensity Quantification Results from LIF Visualization: Heavier drug and center heating during the last 10 mins. 69
3.33 Pixel Intensity Quantification Results from LIF Visualization: Heavier drug and lower heating during the first 10 mins. 70
3.34 Pixel Intensity Quantification Results from LIF Visualization: Heavier drug and lower heating during the last 10 mins. 70
3.35 Pixel Intensity Quantification Results from LIF Visualization: Lighter drug and center heating during the first 10 mins. 71
3.36 Pixel Intensity Quantification Results from LIF Visualization: Lighter drug and center heating during the last 10 mins. 71
3.37 Pixel Intensity Quantification Results from LIF Visualization: Lighter drug and lower heating during the first 10 mins. 72
3.38 Pixel Intensity Quantification Results from LIF Visualization: Lighter drug and lower heating during the last 10 mins. 72
3.39 $\delta T = 5 Celsius$ center heating (experimental results) at 2.5 min 74
3.40 $\delta T = 5 Celsius$ center heating (experimental results) at 5 min 74
3.41 $\delta T = 5 Celsius$ center heating (experimental results) at 7.5 min 74
3.42 $\delta T = 5 Celsius$ center heating (simulation results) at t=0.009 75
3.43 $\delta T = 5 Celsius$ center heating (simulation results) at t= 0.0185 75
3.44 $\delta T = 5 Celsius$ center heating (simulation results) at t = 0.037 75
3.45 $\delta T = 10 Celsius$ center heating (experimental results) at 2.5 min . . . 76
3.46 $\delta T = 10 Celsius$ center heating (experimental results) at 5 min 76
3.47 $\delta T = 10 Celsius$ center heating (experimental results) at 7.5 min . . . 76
3.48 $\delta T = 10 Celsius$ center heating (simulation results) at t=0.0009 . . . 77
3.49 $\delta T = 10 Celsius$ center heating (simulation results) at t=0.00185 . . . 77
3.50 $\delta T = 10 Celsius$ center heating (simulation results) at t=0.0037 . . . 77
3.51 $\delta T = 10 Celsius$ lower heating (experimental results) at 2.5 min . . . 78

3.52 $\delta T = 10 Celsius$ lower heating (experimental results) at 5 min 78
3.53 $\delta T = 10 Celsius$ lower heating (experimental results) at 7.5 min . . . 78
3.54 $\delta T = 10 Celsius$ lower heating (simulation results) at t=0.0009 79
3.55 $\delta T = 10 Celsius$ lower heating (simulation results) at t=0.00185 . . . 79
3.56 $\delta T = 10 Celsius$ lower heating (simulation results) at t=0.0037 79
3.57 $\delta T = 10 Celsius$ upper heating (experimental results) at 2.5 min . . . 80
3.58 $\delta T = 10 Celsius$ upper heating (experimental results) at 5 min 80
3.59 $\delta T = 10 Celsius$ upper heating (experimental results) at 7.5 min . . . 80
3.60 $\delta T = 10 Celsius$ upper heating (simulation results) at t=0.009 81
3.61 $\delta T = 10 Celsius$ upper heating (simulation results) at t=0.0185 81
3.62 $\delta T = 10 Celsius$ upper heating (simulation results) at t=0.037 81
3.63 $\delta T = 10 Celsius$ heads-down heating (experimental results) at 2.5 min 82
3.64 $\delta T = 10 Celsius$ heads-down heating (experimental results) at 5 min . 82
3.65 $\delta T = 10 Celsius$ heads-down heating (experimental results) at 7.5 min 82
3.66 $\delta T = 10 Celsius$ heads-down heating (simulation results) at t = 0.009 83
3.67 $\delta T = 10 Celsius$ heads-down heating (simulation results) at t = 0.0185 83
3.68 $\delta T = 10 Celsius$ heads-down heating (simulation results) at t = 0.037 83
3.69 $\delta T = 10 Celsius$ heads-up heating (experimental results) at 2.5 min . 84
3.70 $\delta T = 10 Celsius$ heads-up heating (experimental results) at 5 min . . 84
3.71 $\delta T = 10 Celsius$ heads-up heating (experimental results) at 7.5 min . 84
3.72 $\delta T = 10 Celsius$ heads-up heating (simulation results) at t=0.009 . . . 85
3.73 $\delta T = 10 Celsius$ heads-up heating (simulation results) at t=0.0185 . . 85
3.74 $\delta T = 10 Celsius$ heads-up heating (simulation results) at t=0.037 . . . 85
3.75 Physical model setup and coordinate system in (Shu and Pop, 1997) . 90
3.76 Transformation of the physical model in our study 91
3.77 Representative velocity profiles for $R_a = 10^3$ 93

LIST OF TABLES

Number *Page*

1.1 is adapted from source: (Milo and Phillips, 2015). The diffusion coefficient of water molecule in water is approximately 2000 $\mu m^2/s$; the diffusion coefficient for protein of 30kDa in water is approximately 100 $\mu m^2/s$. 5

2.1 Change in gel and liquid volume of the human vitreous with age (Source: (E. Balazs, 1993),(E. A. Balazs, 1982)) The vitreous is more gel-like in childhood; the liquid vitreous occupies almost half of the vitreous by 70s. 11

2.2 Comparison of Material Properties 12

2.3 Intravitreal injection protocol performed in the clinic vs. modified protocol in this study 17

2.4 Parameters used in PIVview software for Particle Image Velocimetry (PIV) analysis 20

2.5 Specified camera settings in LYNX GigE Application 20

3.1 Maximum Pixel Intensity in Each Heating Method 73

3.2 Corresponding physical property values for each solution 87

3.3 Values of dimensionless numbers in each scenario (Note: L = 5 mm and delta T = 5 for the characteristic length and temperature difference in Rayleigh number calculation) 88

3.4 Maximum Velocity Reading Near the Wall from PIV Analysis 94

Chapter 1

INTRODUCTION

1.1 Background

Anatomy of the eye

Human eye is a very delicate structure, with 80% of its space between the lens and retina filled with a fluid-like gel, vitreous humor. Vitreous humor is composed of approximately 98–99% water with trace amounts of hyaluronic acid, glucose, anions, cations, ions, and collagen (K. S. Scott and Oliver, 1999). It is a very important space for eye disease treatments as well because a lot of the treatment processes occur in this space. In the center of the retina, there is a small but important area called the macula. It is a very critical structure as it allows us to see details of objects in front of us. (American Academy of Ophthalmology) The macula encounters diverse issues as people get older. When it happens, patients usually experience severe vision loss if they don't receive proper treatment. To name a few macula-related diseases: branch retinal vein occlusion, macular degeneration (dry or wet), retinal detachment, retinitis pigmentosa, etc. In this study, we focus on investigating how drugs travel/mix in the vitreous chamber to reach the macula and treat macula-related eye diseases. A detailed demonstration of the anatomy of the eye can be found in Figure 1.1 below.

Eye Disease Background and Treatment Challenges

As mentioned earlier, many eye diseases are macula-related. In this study, we would like to start with improving the treatment efficacy for age-related macular degeneration (AMD), since it is the leading cause of central vision loss in the developed world. The primary treatment for AMD, intravitreal injection, is a very representative treatment method for many other eye diseases as well. Therefore, the study outcome can make a broader impact.

Patients with AMD see a dark spot in the center of their vision. There are two forms of the disease. The "dry" form of the disease is characterized by yellow deposits or

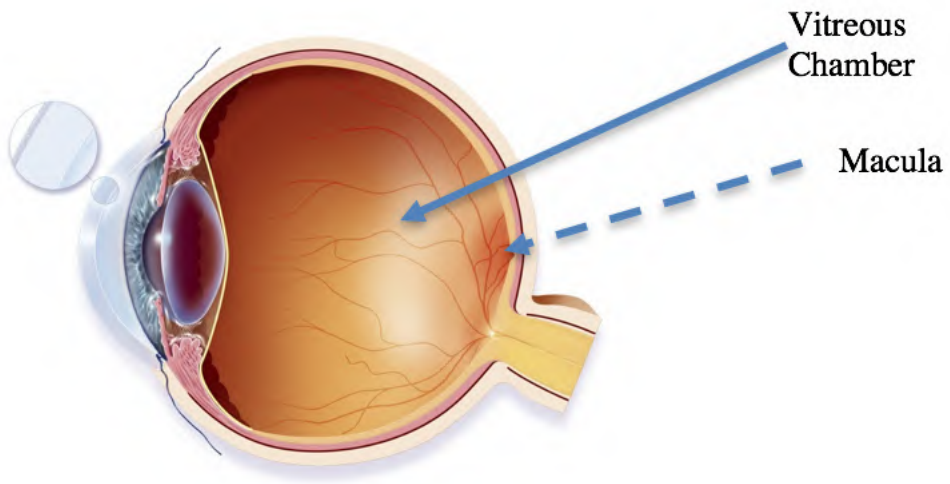

Figure 1.1: Anatomy of the eye (figure adapted from verywellhealth.com) The solid arrow indicates the space filled with vitreous humor; the dashed arrow indicates the typical location of macula.

choroidal neovascularization that develops underneath the retinal pigment epithelium. Fluid and blood leak through these abnormal vessels, creating scar tissues. In the "wet" form, normal macular tissues are lost which also cause severe vision loss. A typical vision of a patient with AMD disease is shown in Figure reffig:amd below.

In the case of wet AMD, it can be managed through serial intravitreal injections of anti-vascular endothelial growth factor (anti-VEGF) agents. During such an injection, an ophthalmologist injects 50 microliters of the drug into the vitreous chamber of a patient every four weeks. These anti-VEGF injections are effective at stabilizing, often improving visual acuity in patients with wet AMD. A similar treatment method can also be used to treat diseases such as diabetic macular edema, retinal vein occlusion, and other vascular disorders.

The injection interval usually takes about four weeks. Ophthalmologists observe changes in patients' visual acuity to determine if another injection is needed. For each injection, the ophthalmologist uses a 27 Gauge or 30 Gauge needle to inject 50 microliters of drug solution into the vitreous chamber. Although effective, intravitreal injection is not a perfect solution for every patient, and it potentially causes many complications such as intraocular inflammation, retinal detachment, traumatic lens damage, and sustained ocular hypertension. To reduce the frequency

of injections but still maintain the treatment efficacy, a possible strategy is to increase drug delivery efficiency during each injection. The focus of this study is to explore various ways to increase drug delivery efficiency.

Figure 1.2: A typical image that a patient with AMD disease sees (figure adapted from Bausch.com) As it is shown in the image, the patient would experience blurred vision, and a dark spot in the center of the vision, as well as distortion of straight lines.

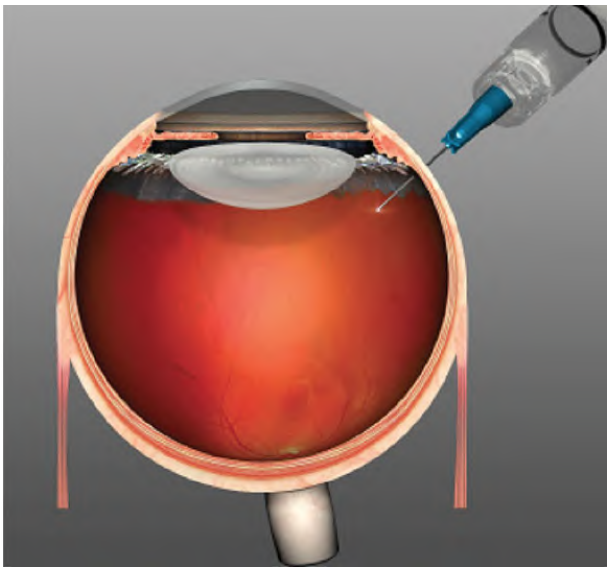

Figure 1.3: Intravitreal injection procedure (Source: Karl Brasse, MD, Eyeland Design) Drugs injected into the vitreous chamber exit near the front of the eye.

During an injection process, the needle tip is positioned at 3 to 4 mm posterior to limbus. Therefore, the drug usually exits the syringe tip at a position that is closer to the front of the eye. Figure 1.3 demonstrates a typical intravitreal injection process. Once the drug enters the vitreous chamber, there are two elimination routes, as indicated in Figure 1.4: anterior and posterior. For anterior elimination, the drug must diffuse in the vitreous to gain further access to the aqueous humor. This would then allow the drug to enter the blood stream. The posterior route requires that the drug must diffuse in the vitreous and then cross the endothelia and epithelia of blood-ocular barriers. These barriers are quite selective in determining the type of molecules that can pass. The exact sites of action for VEGF binding activity of the drug are still not known. However, it is anticipated that both diffusion routes (anterior and posterior) can be involved in the drug transport activities. The diffusion speed depends largely on the individual's physiological condition as well as drug molecule weight. As a result, drugs usually have very different delivery speeds in the vitreous humor: small molecule drugs can diffuse much faster, whereas the mobility is restricted for large molecule drugs.

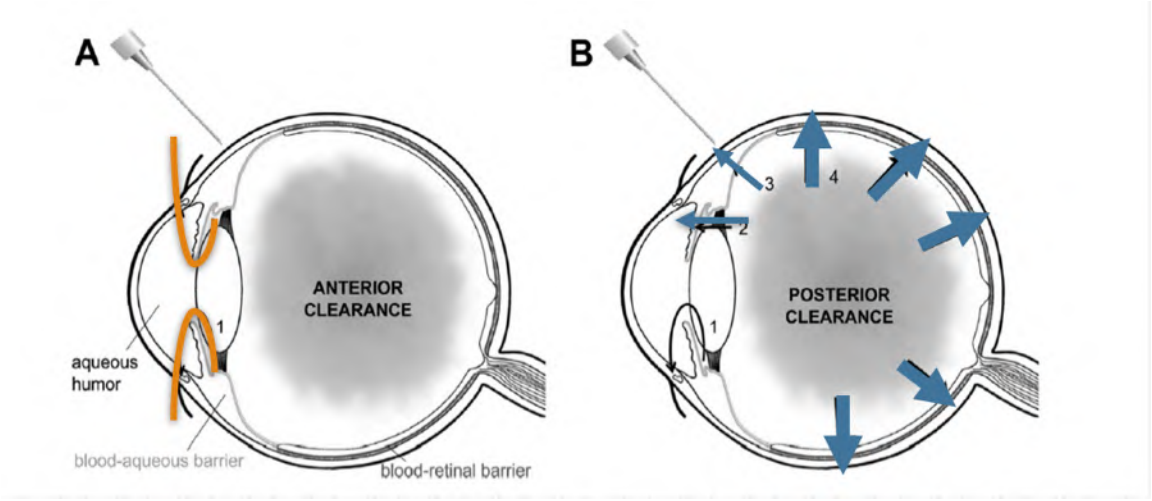

Figure 1.4: wo drug elimination routes for drug in vitreous chamber: anterior (left) vs posterior (right) Maurice and Mishima, 1984 Anterior route (labeled in blue) is for drugs to diffuse in the vitreous to enter aqueous humor and then reach the blood stream; posterior route (numbered in 2, 3, and 4) is for drugs to diffuse in the vitreous and then cross the blood-retinal and blood-aqueous barriers.

To deepen our understanding of the challenge in drug mixing process via diffusion, it is helpful to understand the meaning of anti-VEGF agents first. There are a few different anti-VEGF agents that are used for treating eye diseases. Taking bevacizumab

as an example, bevacizumab is a recombinant humanized monoclonal IgG1 antibody that contains human framework regions and murine complementarity-determining regions. Bevacizumab has an approximate molecular weight of 149 kDa (RxList, Avastin). Avastin is the brand name for bevacizumab. Avastin (bevacizumab) is a colorless to pale brown solution and is usually supplied in 100 mg and 400 mg preservative-free single-dose vials. For a 100 mg product, it is formulated in 240 mg α,α-trehalose dihydrate, 23.2 mg sodium phosphate (monobasic, monohydrate), 4.8 mg sodium phosphate (dibasic, anhydrous), 1.6 mg polysorbate 20, and Water for Injection, USP. Therefore, water is the main carrier of the drug in the delivery process. Since the majority of the AMD patients are among the older population, their vitreous are usually more fluid-like than gel-like. More details regarding the change in vitreous properties with aging process will be explained in the following sections. Overall, the time it takes for drugs to deliver to target tissue via pure diffusion can be approximately estimated by calculating the time it takes for water to diffuse in water. Table 1.1 below shows a list of empirical diffusion constants. ((Yorston, 2014a),(Miller, 1924))

molecule	measured context	diffusion coefficient ($\mu m^2/s$)	BNID
water	water	2000	104087, 106703
oxygen	water	2000	104440
tRNA ($\approx 20kDa$)	water	100	107933,107935
protein ($\approx 30kDa$ GFP)	water	100	100301
protein ($\approx 30kDa$ GFP)	eukaryotic cell (CHO) cytoplasm	30	101997
protein ($\approx 30kDa$ GFP)	rat liver mitochondria	30	100300

Table 1.1: is adapted from source: (Milo and Phillips, 2015). The diffusion coefficient of water molecule in water is approximately 2000 $\mu m^2/s$; the diffusion coefficient for protein of 30kDa in water is approximately 100 $\mu m^2/s$.

To estimate the time scale τ for a particle to travel distance x, we can use $\tau \approx x^2/D$. Since the average size of a human eye is 24.5 mm in diameter, $\tau \approx (24.5mm)^2/(2000\mu m^2/s) = 83$ hrs, which is approximately 4 days. This theoretical calculation is consistent with our experimental observations. In our experiment, we injected water-dissolved dye into water and observed how long it took for the

dye/water mixture (1 : 50 ratio) to travel 10 mm vertical distance. It took about 20 hrs in total, which was as expected.

Based on this calculation result, it raises a concern that drug delivery by pure diffusion might be taking too long, given that the vitreous half-life of anti-VEGF is quite limited and can range from a few hours to a few days. ((Stewart, 2018),(Kim, Robinson, and Csaky, 2009)) In addition, the diffusion coefficient of protein of molecular weight $30kDa$ is $100\mu m^2/s$ in water, which is much slower than water diffusion in water. Anti-VEGF agents are usually large molecules ($> 150kDa$). The diffusion rate can be much slower since the mobility of large molecules is usually restricted. This is also confirmed by various research studies summarized in (Del Amo Eva et al., 2017). Figure 1.5 below summarizes diffusion coefficients of molecules and particles in vitreous, liquefied vitreous, and water.

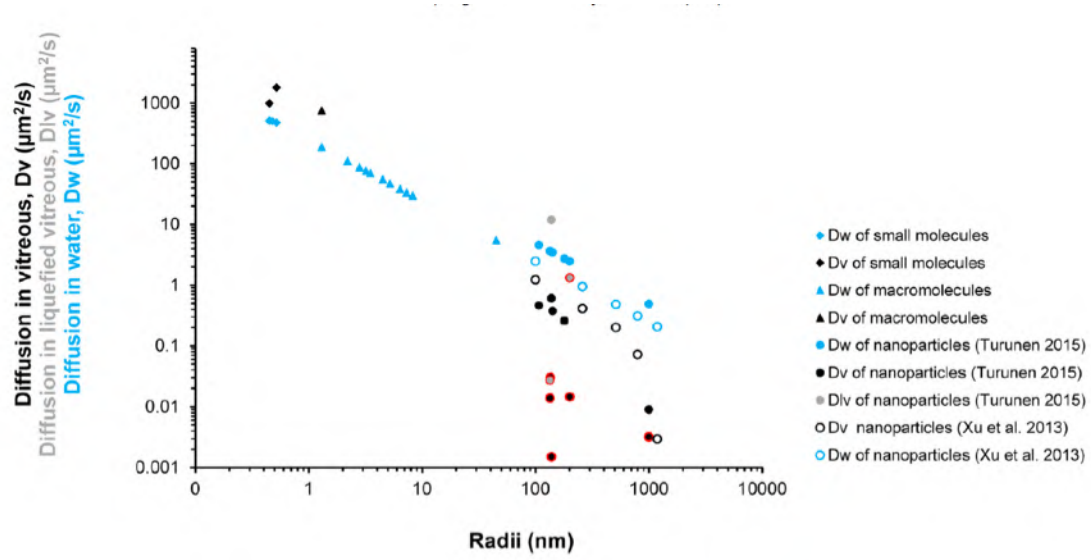

Figure 1.5: Diffusion coefficients of molecules and particles in the vitreous. (Source (Del Amo Eva et al., 2017))

Therefore, to effectively increase injection efficiency, drugs cannot solely rely on diffusion via anterior or posterior diffusion routes, and convection needs to be introduced into the scenario. Additionally, another goal of this study is to promote fluid mixing in the eye in a minimally invasive manner. To summarize the two objectives, they are to 1) effectively induce convection in the drug delivery process in the eye to accelerate drug transport efficiency, 2) and promote flow circulation in the eye to facilitate better drug mixing for improved treatment efficacy. It is worth noting that there hasn't been much study of the role of convection flow in promoting

drug distribution in the eye in the past. (Del Amo Eva et al., 2017) Our study outcome can offer great insights to be incorporated into the clinical procedure for improved patient care.

Previous Treatment Efforts and Previous Research Efforts

Several different ways to increase drug delivery efficacy in the eye have been explored both clinically and academically. Clinically, there are four delivery alternatives and they are summarized in Figure 1.6 below. These alternative methods are topical, systemic, implants, and trans-scleral. These various methods are either designed in an attempt to bypass the two diffusion routes in the eye, or to alleviate the potential side effects.

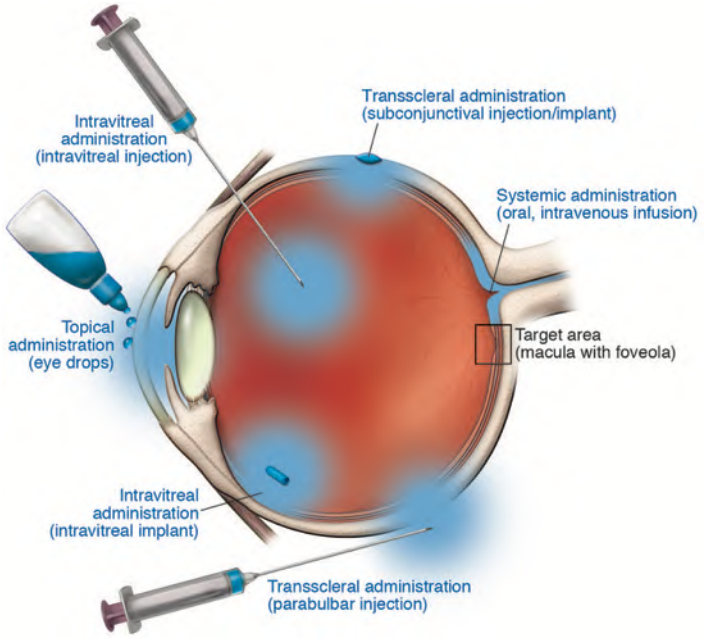

Figure 1.6: Schematic drawings of various drug delivery methods for treatment of AMD (Holz, Schmitz-Valckenberg, and Fleckenstein, 2014) The target area (macula) can be reached by administrations via various routes: topical delivery to the surface of the eye, trans-scleral delivery underneath the conjunctiva, direct injection (injection or implant), and systematical delivery via oral tablets.

Topical drops must diffuse across a few layers to reach the target tissue, these layers include tear film, cornea, iris, ciliary body, and vitreous. This can severely dilute the fraction of drug reaching the target issue. Systemic delivery such as tablets can result in a poor dose-response profile. (Geroski and Edelhauser, 2000) Ocular implant takes the same idea as intravitreal injections and thus can also benefit from our study

outcomes. Trans-scleral administration injects drugs via a region surrounding the eye and experiences the same issue that exist in topical administration: the overall retinal bioavailability is very low (in the range of 0.1%) after such an administration, which is not an ideal choice for retinal drug delivery. (E.M. del Amo et al. 2017) Overall, intravitreal injection is so far the mostly practiced as well as the most effective treatment for retinal drug delivery.

In the research field, scholars have also made great efforts in understanding fluid flow in the eye from both animal study and computational perspectives. In the animal studies, experiments were performed using bovine or rabbit eyes. However, these structures are not physiologically identical to human eyes. Moreover, some of the eye functions might change once vitreous humor is sampled from a deceased animal. Therefore, these study results are insightful but not straightforward.

1.2 Organization of the thesis

The first part of the thesis focuses on the introduction and discussion of eye disease background, various treatment methods, and previous studies. In the following sections, two different methods for driving convective flow in the eye are introduced: one through lateral movements (motional-driven) and one through heating/cooling (thermal-driven). The detailed experimental setup, results, and implications will be discussed in their respective sections.

Chapter 2

DRUG DELIVERY IN THE EYE UNDER LATERAL MOVEMENTS

2.1 Introduction

Various eye movements and their corresponding functions

There are four basic types of eye movements: saccades movements, smooth pursuit movements, vergence movements, and vestibule-ocular movements.
1) Saccades movements are rapid movements and the eyes abruptly change the point of fixation during such movements. In daily life, saccades movements of the eye happen in many scenarios, ranging from small movements made during reading and large movements made when a person is simply looking around. It can also occur during sleep.
2) Smooth pursuit is much slower compared with saccades movement. It facilitates voluntarily tracking a moving stimulus.
3) Vergence movement is quite different than the other two in the sense that it is disconjugate, which means eyes can move in different directions.
4) Vestibule-ocular movements compensate for head movements so the eyes are stabilized relative to the external world, which can help with stabilizing visual images on the surface of the retina when the head moves. These four movements can essentially be broken down into three fundamental motions: rapid lateral motion, rotating motion, and slow lateral motion.

Eye Model

The human eye has a complicated structure. Instead of trying to reproduce every single detail in the eye, it is important to grasp the most important features to acquire critical insights experimentally. The content below explains the main structural challenges that people see in human eyes as well as selection criteria when the eye model was built for our study.

1) Liquid concentration is not uniformly distributed in the eye. Vitreous humor is

composed of 98% to 99% water and 1% other ingredients. This 1% other ingredients, the majority of which are collagen and hyaluronan, has various distribution in different regions of the eye. (Figure 2.1) For the drug to reach the retina via the posterior route, it must first travel across the central vitreous chamber and then pass the vitreous cortex to reach the back of the eye. Further, even by considering the anterior route, the drug still needs to diffuse through the vitreous to join the aqueous flow. Therefore, effectively promoting drug mixing in the eye can potentially facilitate drug eliminations via both routes.(Gaudana et al., 2010)

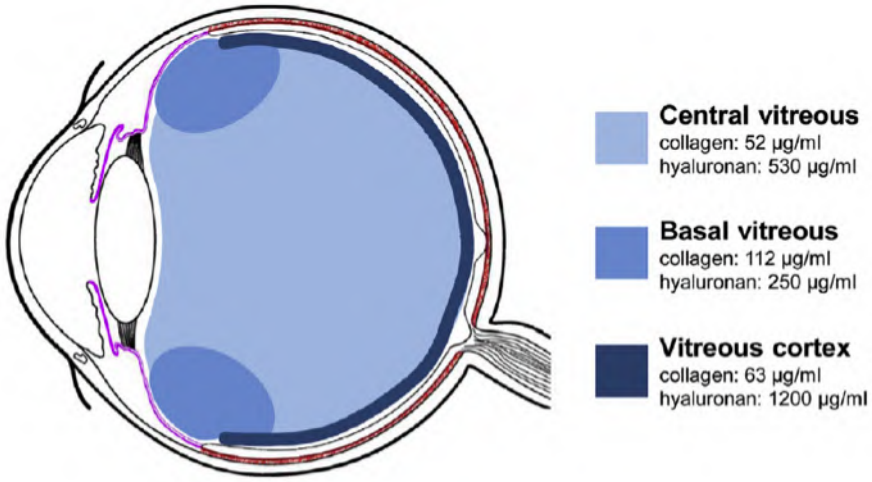

Figure 2.1: Variations in concentrations in the vitreous ((Purves et al., 2001)) As it is demonstrated in the figure, hyaluronic acid and collagen are not uniformly distributed within the vitreous. The highest concentration is in vitreous cortex, which is the region that is the closest to retina. The central area (central vitreous) is more liquid like, followed by basal vitreous.

2) Components of human vitreous change consistently as people age. As shown in Table 2.1, vitreous is a 100% gel solution when we are born and liquefaction gradually happens as we get older. This is one factor that explains the discrepancy in treatment efficacy among various individuals. Many other factors include ethnicity, genetics, and special procedures performed (for example, vitrectomy).

Age (years)	Gel Volume (cm^3)	Liquid Volume(cm^3)
Birth	1.6	0
5	3.3	0
10	3.5	0.7
30	3.9	0.9
50	3.5	1.3
70	2.8	2
90	2.2	2.6

Table 2.1: Change in gel and liquid volume of the human vitreous with age (Source: (E. Balazs, 1993),(E. A. Balazs, 1982)) The vitreous is more gel-like in childhood; the liquid vitreous occupies almost half of the vitreous by 70s.

Based on the two above-mentioned structural challenges, one interesting parameter to look at is the effect of density/viscosity difference between the injected drug and the vitreous to understand how drug flow proceeds in various environments. Since regional distributions of liquid and gel components are unclear and it obviously differs case by case, we start with a vitreous model of uniform density/viscosity distribution to get a generalized understanding.

To determine the range of physical properties values of human vitreous, we refer to the analysis conducted by (K. R. Murthy et al., 2014). It states that the viscosity of human vitreous is two to four times greater than water, which gives vitreous humor a gelatinous consistency. This conclusion is derived based on a study conducted by John Locke, M.D. and Ross Morton, M.D. (Locke and Morton, 1965) The measurements were performed based on 177 samples obtained post-mortem from 97 donors at the Institute of Pathology, McGill University. In addition, during a vitrectomy operation, vitreous humor of the patient being treated is replaced by 0.9% saline solution. Furthermore, AMD usually affects populations of age 50 and older, whose vitreous humor is more liquid-like than gel-like. Based on these facts, it was decided that both 0.9% saline and glycerol/water mixtures at various ratios were used to make “vitreous humor” in our study. A summary of these material properties can be found in Table 2.2 below.

Material Type	Viscosity ($mPa \cdot s$)	Density(kg/m^3)
Water at 25 Celsius	0.9	1000.0
Saline (0.9% NaCl)	1	1063.3
Human Vitreous	1-3.6	1005.3–1008.9
Glycerol/Water Mixture (1:5)	1.7	1046.8
Glycerol/Water Mixture (2:5)	2.7	1081.5
Glycerol/Water Mixture (1:10)	1.3	1024.5

Table 2.2: Comparison of Material Properties

Variations on Injection Sites

As mentioned earlier, during an intravitreal injection session, an ophthalmologist uses a 27 gauge or 30 gauge needle to inject 50 microliters of drugs into the vitreous chamber of a patient's eye. The injection position is usually 3 to 4 mm posterior to limbus (Figure 2.2) and target at the central region.((Wilson and A. Scott, 2013),(Yorston, 2014b)) Given that the average diameter of the eye is around 24-mm, the injection spot is quite close to the front of the eye. Therefore, it might not be an ideal entry spot for effective drug delivery in the eye. Furthermore, human eye size varies case by case, so if the same protocol is performed for every individual, the treatment efficacy could certainly vary. ((Akinkunmi, Jahn, and Giovambattista, 2015),(Cristancho et al., 2011),(Frederick, David, et al., 2015))

Therefore, besides lateral movements, another objective for this motion-drive study was to explore the effects of varying injection sites on drug mixing profiles. These three injection sites were studied: side injection (which is similar to the actual intravitreal injection process), center injection (which is more towards the center and more in depth), and bottom injection (which is the deepest among the three). More details can be found in the experimental design methods section.

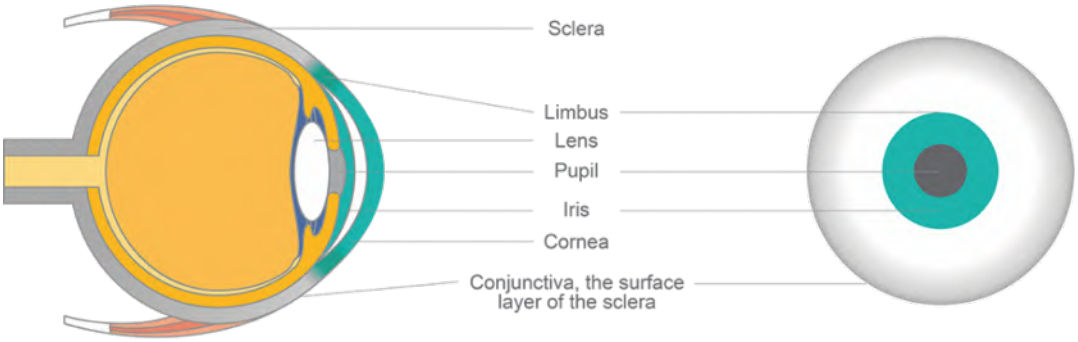

Figure 2.2: Anatomy of eye Note that 3 to 4 mm posterior to limbus is very close to the front of the eye.

2.2 Experimental Design Methods

Choice of Voluntary Eye Movement

In the previous sections, we already discussed a few physiological challenges that are associated with human eyes, including variations in concentrations across different parts of the eye, changes to eye composition with aging, multiple clearance routes, etc. It's important to keep those challenges in mind when selecting features of interest to be included in the eye model design.

In terms of choice of eye movements, there are four types of basic eye movements, as mentioned earlier: saccades movements, smooth pursuit movements, vergence movements, and vestibule-ocular movements. Details about their respective motions and functions were explained in the introduction section and will not be repeated. Essentially, there are three major types of motions involved in all the movements: rapid lateral motion, rotating motion, and slow lateral motion.

Consciously inducing voluntary eye movements could potentially agitate vitreous humor in the eye. Further, this could facilitate fluid flow in the eye and thus promote drug delivery to the back of the eye. In addition, since patients are likely to experience great discomforts right after injection procedures, a good eye exercise procedure would require patients to move their eyes minimally. Thus, the lateral eye movement at a low frequency is the target eye motion in this study.

Lateral movement is essentially moving eyes horizontally back and forth between left and right. Movement magnitude and frequency are usually based on voluntary decisions. In this study, the lateral movement is determined to be 45 degree in its sweep angle 1 cycle per second (1 Hz) for the movement frequency. (Figure 2.3) This motion is slow enough for a post-surgery patient to perform in a comfortable manner. Of course, it is possible to select a higher movement frequency which means the patient will need to move his/her eye in a much faster manner. However, based on our experimental observations, simply increasing the eye movement frequency does not necessarily facilitate a better drug mixing outcome. Rather, factor such as eye morphology plays a more critical role. We will discuss about it in more details in the discussion section.

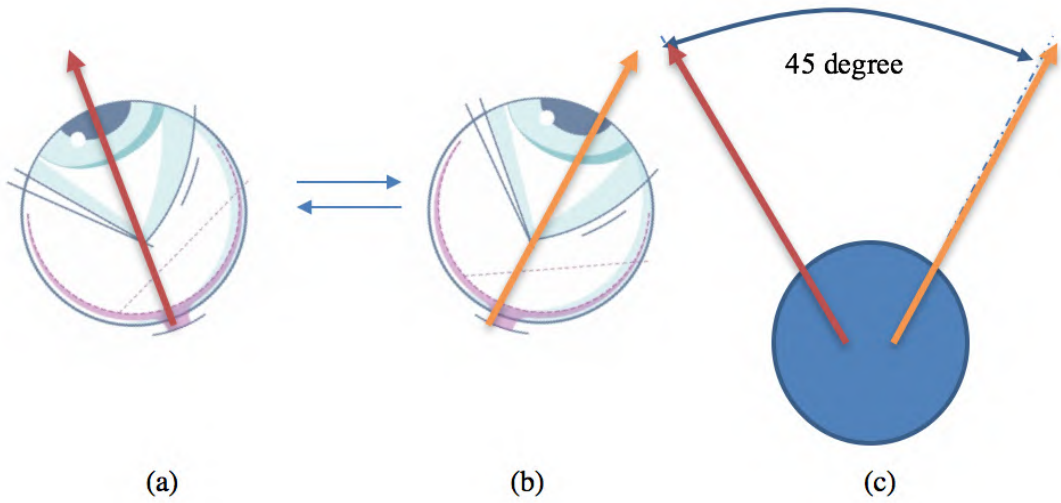

Figure 2.3: Desired voluntary lateral movement in this study (Picture (a) demonstrates an eye looking to the left and the orange arrow indicates the center of the eye globe in (a); Picture (b) demonstrates the eye looking to the right and the green arrow indicates the center of the eye globe in (b); During this voluntary lateral movement, the eye moves back and forth between left (a) and right (b) at 1 Hz. The sweep angle is 45 degree, which is demonstrated in (c))

Vitreous Humor Preparation

Our eye model was made from glass in the form of a 1-inch (24.5 mm) diameter globe (Figure 2.4). Its size is the same as the average size of a human eye. As the vitreous medium, the DI water and salt mixture (0.9% saline) was chosen. As mentioned before, on one hand, this mixture resembles general eye properties among older populations whose vitreous are more fluidic than gel-like; on the other hand, for operations that involve vitrectomy, it's a standard procedure for ophthalmologists to replace patients' vitreous with 0.9% saline. The saline solution was prepared in a large bulk (1 L) and stored at room temperature overnight. This assumes that the solution property is consistent across all the experiments. In addition, the bottle was shaken well before each use to ensure an even distribution of salt in the solution. (Kummer et al., 2007)

As the second choice for vitreous humor, glycerol and water were mixed at 1 to 5 ratios to study the viscosity effect on the fluid mixing pattern. Table 2.2 should be revisited for material properties.

(a) Actual picture of an eye model with openings for injection

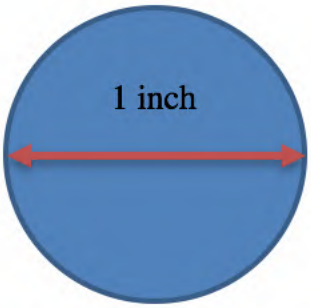

(b) The diameter of the eye model is 1 inch.

Figure 2.4: Eye model in our study Fabricated at Caltech glass shop. The diameter is 1 inch.

Various Injection Sites of Eye Model

A typical intravitreal injection procedure performed by ophthalmologists in the clinic as well as the modified protocol in our study is summarized in Table 2.3 below. The detailed position of each injection site is demonstrated in Figure 2.5. As mentioned

before, the side injection is the closest to an ophthalmologist's injection behavior, whereas the center and bottom injection positions are more in-depth.

Item	Our Protocol	Ophthalmologist's Protocol
Needle	21 Gauge needle	27 Gauge or 30 Gauge needle
Injection duration/frequency	100 μl injection over the course of 1 min	50 μl injection every 4 weeks
Injection site	bottom, center, and side (Figure 10)	3 to 4 mm posterior to limbus, avoid meridian horizon, target the central region

Table 2.3: Intravitreal injection protocol performed in the clinic vs. modified protocol in this study

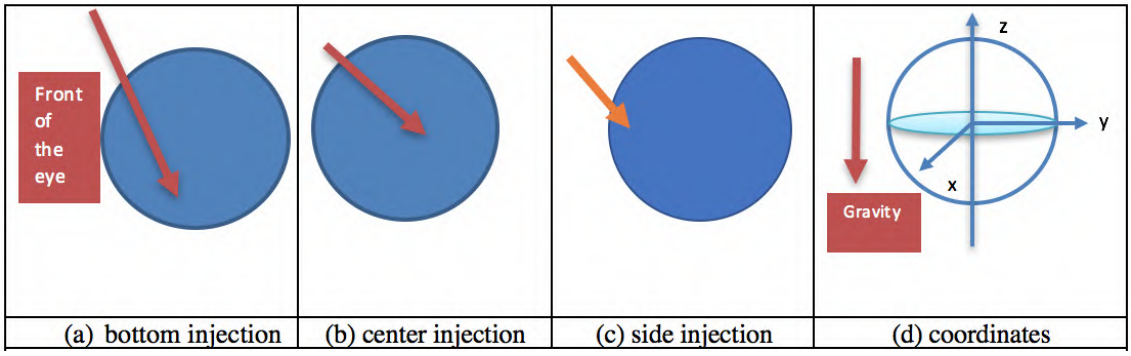

Figure 2.5: Various injection sites (The orange arrow represents needle tip; the front of the eye is labeled in (a) and will be the same for (b) and (c))

Imaging Technique -Overview

Digital particle imaging velocimetry (DPIV) technique was used to quantitatively map the fluid field. In summary, fluorescence materials were mixed with the solution of interests to assist with flow visualization. A series of flow images were taken during a visualization session and the resulting images were cross correlated using commercial software PIV3CView (PIVTEC). Quantitative results such as velocity field could thus be obtained.

To set up the equipments, as shown in Figure 2.6, convex lens was used to spread the laser beam vertically so that the camera was visualizing only a thin sheet of the entire globe. The laser beam was carefully calibrated to pass through the center of the eye model. Essentially, flow profiles on a 2D plane of a 3D object were observed. In our study, a 445-nm blue laser was used to illuminate the particle laden flow field (laser model: Skye 100-mW handheld 445-nm focusable blue laser pointer with dual lock). The flow images were captured by a camera with a resolution of 640 by 480 pixel (IPX-VGA210-L; 90 mm Tamron Lens, Saitama, Japan; Sony Alpha-7) at 10 frame per second (fps). The camera setting was adjusted using the free software, LYNX GigE Application. A majority of the parameters were set at their default values, with a few modifications summarized in Table 2.4.

There were two types of fluorescence materials used in this experiment: fluorescence particle and laser-induced fluorescence (LIF, which is a dye). Both materials can be excited by a laser of a given wavelength. Mixing fluorescence particles (manufactured by Kodak Company) with the solution of interests can mark the fluid flow motion. Fluid flow images were then captured and PIV analysis was performed on the resulting images to obtain velocity profiles. These velocity profiles were later analyzed for making particle pathlines visualizations. Using LIF (fluorescein) for visualization allowed us to observe the dynamic mixing process in the eye model. Solution that carries fluorescein was injected into the solution without fluorescein. By quantitatively analyzing fluorescein light intensities, the amount of drugs that reached the target issue at different time stamps was quantified.

Before a visualization, the two fluorescence materials were mixed with either 0.9% saline or glycerol/water mixture. Fluorescence particles were carefully selected to have the same density and diffusivity as the solution so the particle movements were representative of flow motion. In this motion-driven study, fluorescence particles manufactured by the Kodak company were selected since density of these particles

were very close to 0.9% saline. Fluorescein was added to 0.9% saline or glycerol/water mixture at the ratio of 1:50 (fluorescein to solution ratio). This assumes that any possible changes to physical properties of the solution due to addition of fluorescein were negligible.

Summary of PIV Visualization Set Up

In summary, there were a few major equipments to complete a PIV visualization setup: a blue-violet laser (wavelength = 445 nm) for exciting fluorescence materials, a convex lens to spread the laser beam into a laser sheet, a camera (IPX-VGA210-L) for capturing flow images, an eye model, and a motor-magnet coupler to induce lateral movements at a fixed pattern. (Figure 2.6 and 2.7)

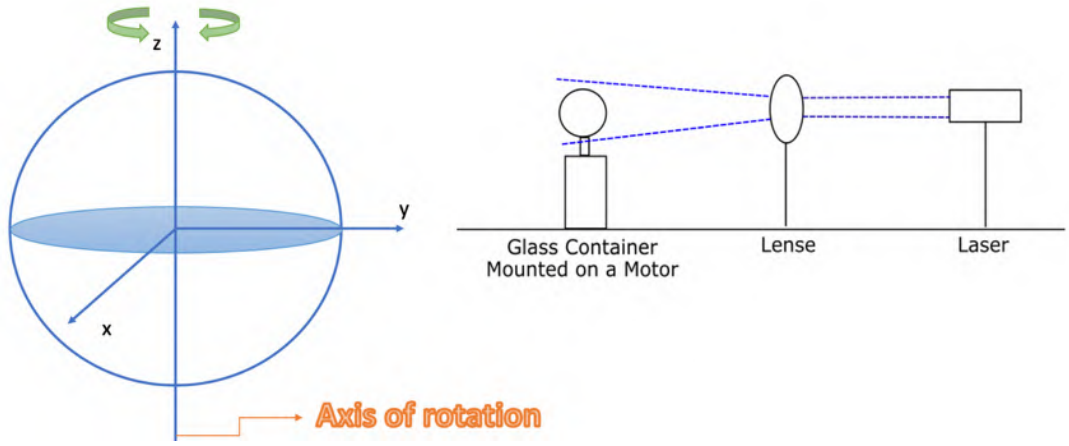

Figure 2.6: Schematic Demonstration of PIV Visualization Setup (from left to right: direction of rotation, the eye model mounted on top of a motor, a concave lens, and a laser.)

After a visualization session, the resulting raw images were analyzed using PIVview software (PIVtech, Gottingen, Germany) with the following parameters as summarized in 2.4 below. The camera settings (LYNX GigE Application) that were changed from their default values are summarized in 2.5 below. The flow measurement was valid up to approximately 1 mm/s, which was the velocity at which an object moved one pixel during the exposure time.

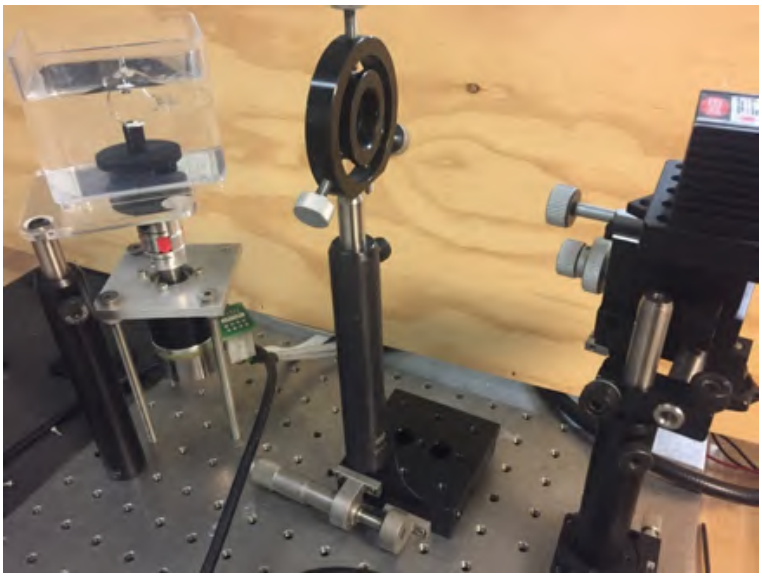

Figure 2.7: Actual PIV Visualization Setup (from left to right: motor-magnet coupler with the eye model, a concave lens, and a laser)

Image Pair Offset	3
Window Size [Pixel]	32 by 32
Step Size [Pixel]	16 by 16
Fast Fourier Transform Correlation	Standard
Maximum Displacement Test[Pixel]	10
Normalized Median Test (thresh)	5
Interrogation	multi-pass

Table 2.4: Parameters used in PIVview software for Particle Image Velocimetry (PIV) analysis

Exposure Time	10 fps
Shutter Time	5000

Table 2.5: Specified camera settings in LYNX GigE Application

Motor-magnet coupler

The motor magnet coupler was composed of three major components: motor (Maxon DC Motor EC 90 Flat Series), a 3D printed holder set for holding the eye model and magnets, and four magnets. (Figure 2.8) The top part of the 3D printed holder set held the eye model and was entirely immersed in a small fluid tank. Fluid that was added into the tank was the same as the fluid that filled the eye model. This ensured that both fluids had the same refractive index and thus no distortions when laser beam passed through the curvature of the eye model.

The bottom part of the holder set sat on top of the motor, which was controlled by EPOS motor controller and LabVIEW. LabVIEW program sent out signals to control the movement of the motor, which also drove the motion of the bottom part of the holder set. (Again, for lateral movements in our study: 45 degree sweep angle at 1 Hz.) The two magnets that were fixed on the bottom holder drove the motions of the two magnets that were fixed on the top holder, and thus the movement of the eye model. The actual motor movement was recorded throughout the experiment. This allowed for tracking and checking the actual motor trajectory during and after each experiment (Figure 2.9).

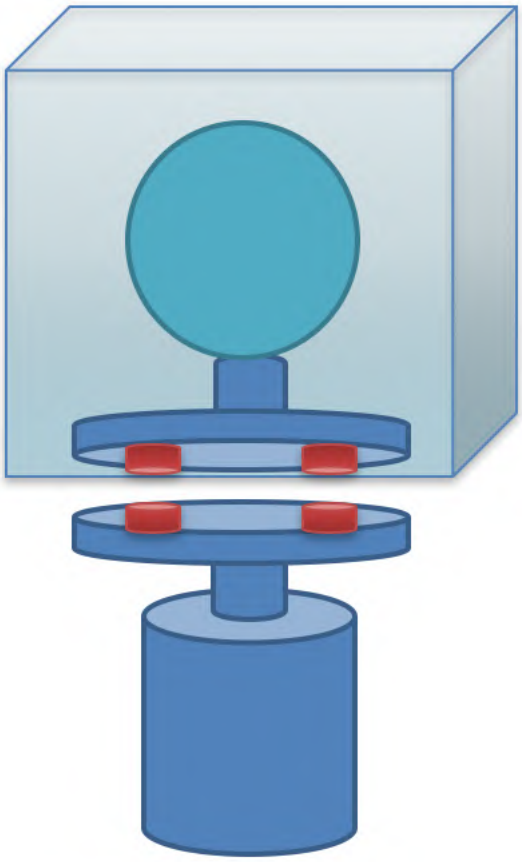

Figure 2.8: Motor-Magnet Coupler Setup (The four orange columes indicate the positions of the four magnets; the eye model (sphere) sits on the top is immersed in a water tank.

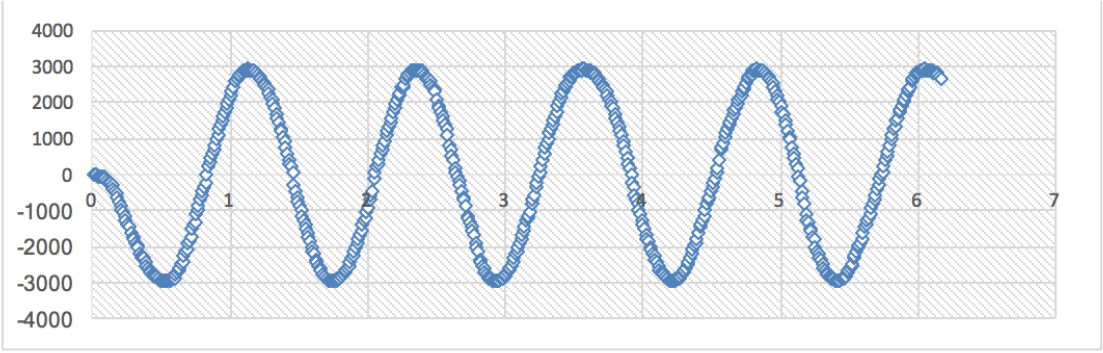

Figure 2.9: Example of a plot of the actual motor trajectory (5 cycles rotations)

Drug Delivery Method

As mentioned earlier, LIF could assist with the observations of drug mixing profile in the eye model. Fluorescein/0.9% Saline mixture of 100 microliters were slowly injected into the eye model that was filled with 0.9% saline at the desired injection spot using a syringe pump (Harvard Apparatus). The entire injection process took about 1 min in total, which was very slow and did not cause the drug to splash inside the eye model. This injection process reproduced the intravitreal injection procedure of injecting microliter-scale of drugs (fluorescein/saline mixture in our study) into the vitreous humor (saline in our study).

2.3 Results

Velocity Vector Plots

Figure 2.10 shows a typical image captured during a PIV visualization session. The white dots are fluorescence particles excited by the 445-nm blue laser light. Note that we wanted to observe fluid motions after the lateral movement stopped. This could help with understanding the duration of mixing after each set of movements. Therefore, during a PIV visualization session, image capturing began before the eye model started to rotate and stopped after the fluid motion completely decayed. However, during a PIV analysis session, only images taken after the eye rotation stopped were analyzed. This also ensured that PIV analysis was performed on the same 2D plane because the visualization plane kept switching when the eye model was moving. In our study, we made comparisons between 5 cycle rotations (rotating a full cycle for five times) versus 10 cycle rotations (rotating a full cycle for ten times).

The average velocity vector plot obtained from a PIV analysis is shown in Figure 2.11. It was obvious to observe from this vector plot that four circulations were formed during the rotation and still sustained after the rotation stopped. To understand whether the duration that circulations sustained was different between less movements (5 cycles) and more movements (10 cycles), a sequence of vorticity plots was made. Figure 2.12 summarized the first sets of vorticity plots (5 cycles on the left and 10 cycles on the right), which were taken right after the rotation stopped. In these plots, vorticity appeared to be stronger after 10 cycles movements as compared with 5 cycles movements. The circulations also sustained for a bit longer after 10 cycles movements, although this information was hard to show in Figure 2.12. It was also worth noting that circulations sustained for quite a short duration in both cases: approximately 5 seconds after 5 cycles movements and 10 seconds after 10 cycles movements.

Figure 2.10: Example of an image captured during a PIV visualization session

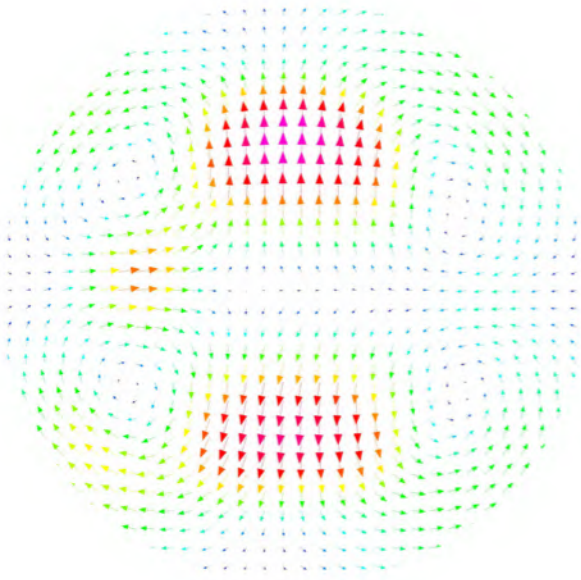

Figure 2.11: Average Velocity Field Obtained from PIV analysis (5 cycles)

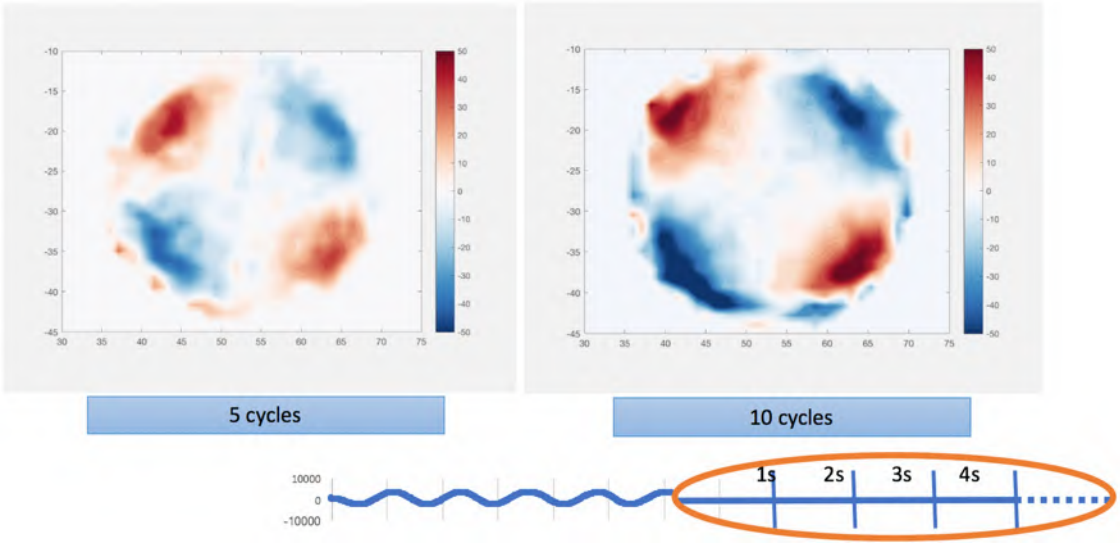

Figure 2.12: First Sets of Vorticity Plots: 5 cycles vs 10 cycles (Note these were taken right after the movements stopped)

Particle Pathline Visualization (0.9% Saline)

Particle pathline visualization is very helpful for understanding the actual particle trajectory. After performing PIV analysis on raw images using the software PIV3CView, files containing flow field information were obtained. Because the flow images were taken at a programmed rate of 10 frames per second, these files were also ordered in a sequential manner. Important flow information contained in these files includes physical coordinate (x,y), velocity components (x,y), velocity gradient (du/dx, du/dy, dv/dx, dv/dy), and vorticity component. (Figure 2.13)

Using these velocity field information, the Lagrangian path of fluid flow can be tracked to create a pathline visualization using MATLAB. At first, locations of particles of interests were defined to obtain and plot the initial position. Then the files containing velocity field were referred at each instance of time to plot the following positions. This same process was repeated over a certain period of time. This is essentially the same as overlaying a sequence of actual particle images onto a single image.

A detailed explanation of the algorithm is shown in Figure 2.14. In Figure 2.14, U is the velocity, which is a function of position (x) and time (t); delta t is the time interval between two adjacent images captured; T_0 is the initial time, $T_1 = T_0 + \delta t$, and so on. After determining the initial position, the next position at T1 is calculated based on the velocity field of the previous position (which is $U(x_0, t_0)$ in this case). This gives the particle position at T_1. The same procedure is used at successive time steps to generate the pathline field for the following positions and that's how we obtain the pathline.

Velocity Field	$\bar{V}$ $\bar{x}$	$\bar{V}$ $\bar{x}$	$\bar{V}$ $\bar{x}$	$\bar{V}$ $\bar{x}$	$\bar{V}$ $\bar{x}$	…
	T_0	T_1	T_2	T_3	T_4	…
Time	T_0	T_1	T_2	T_3	T_4	…

Figure 2.13: PIV analysis can generate a series of files that contain flow property information in a sequential manner

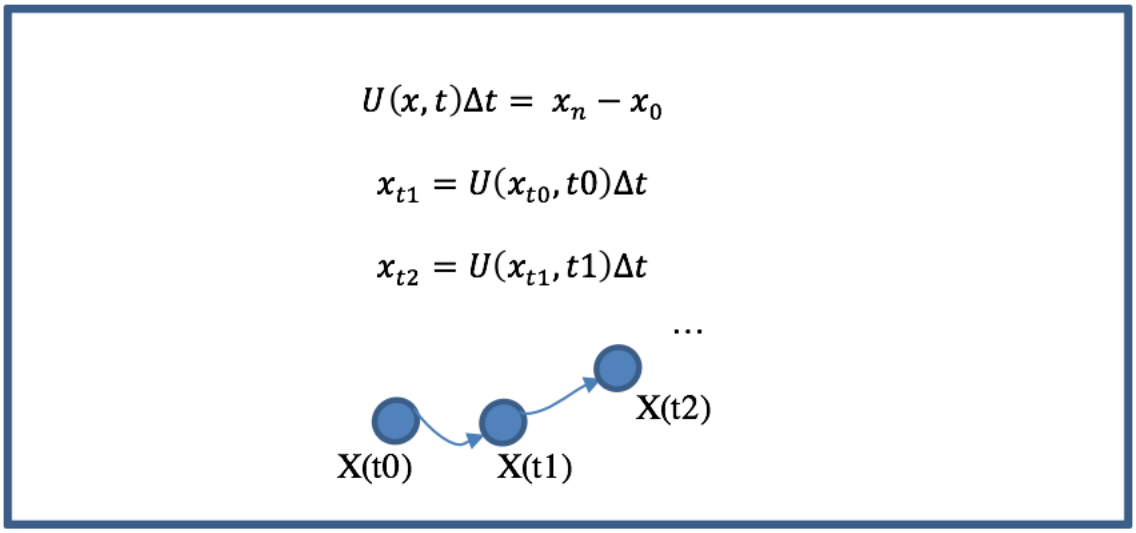

Figure 2.14: Detailed explanation of pathline visualization algorithms (Blue circles indicates particles at different instances of time.)

An example of such pathline visualization is shown in Figure 2.15, which demonstrates the particle trajectories in a total of 8 seconds after 10 cycles lateral movements. Again, the particle pathline tracking begins after the rotation stops and ends when circulations completely decay.

As it is highlighted in Figure 2.16, there are four circulations in the flow and one in each quadrant, which is consistent with the observations from the vorticity plots shown in Figure 2.12. Another important takeaway message from the pathline visualization and vorticity plots is that the initial position of the particle is very likely to affect the final position of the particle. This insight will be discussed further in the discussion section.

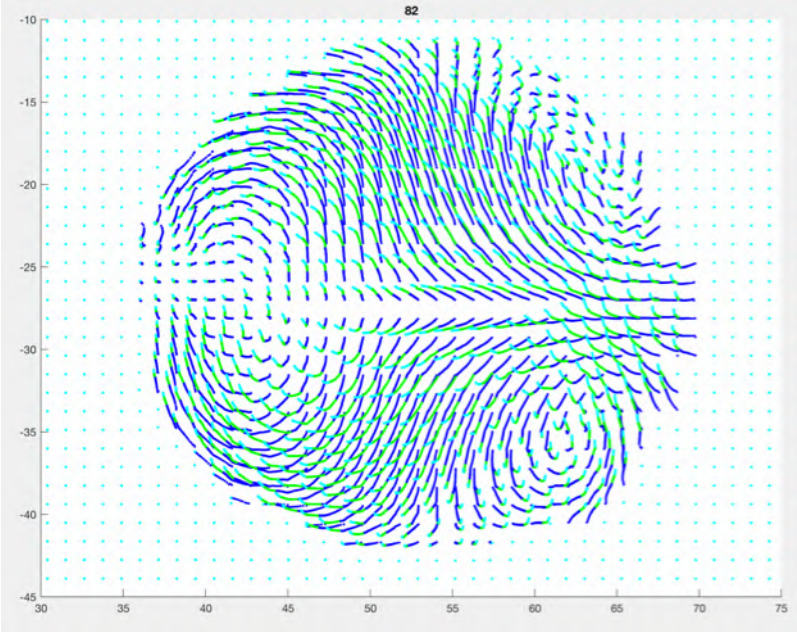

Figure 2.15: Particle pathline demonstration (The beginning of the time is color-coded in dark blue, then green, and finally light blue)

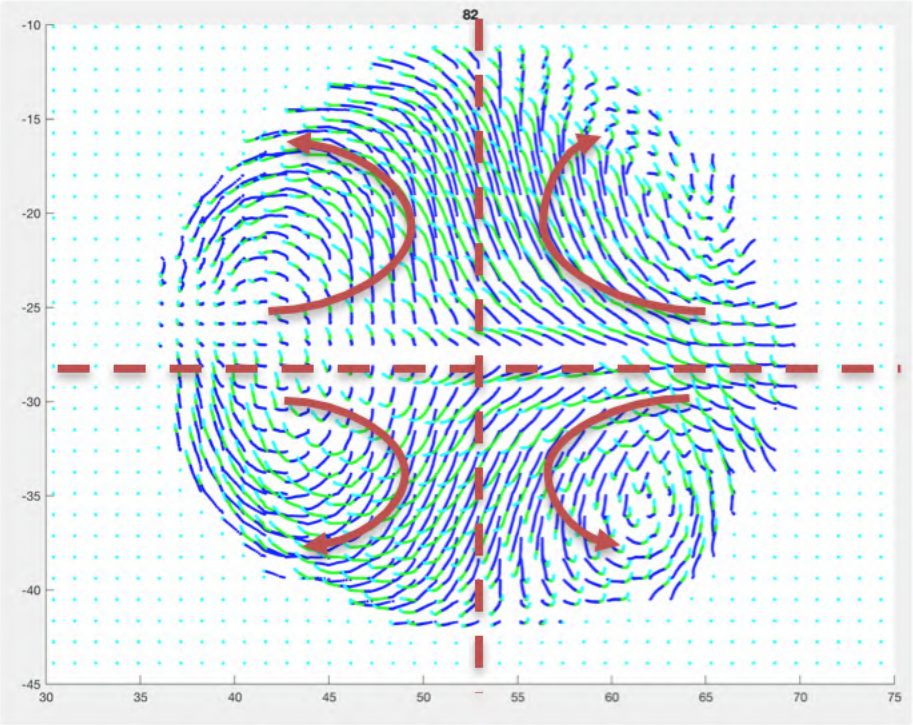

Figure 2.16: Four circulations and one in each quadrant

LIF Visualization – Different Injection Sites

To understand whether injecting drugs at different sites can make a difference to the final drug mixing profile, a LIF visualization experiment was performed. Drugs (mixture of 0.9% saline and fluorescein) were injected at the bottom, center, and side locations of the eye model. In this set of experiments, the eye model went through a series of 10 cycles lateral movements intermittently: after the initial injection, the eye model was rotated for 10 cycles. The magnitude of drug mixing was then observed and recorded by the camera before another 10 cycles of rotations was performed. This process was repeated until drugs were well mixed in the entire chamber. The resulting images were summarized in Figure 2.17. By examining the images carefully, it was obvious to see that center injection took the shortest amount of time as well as the least amount of movements for the drug to mix well in the eye. Bottom injection and side injection took a longer duration and more movements to achieve complete drug mixing in the eye.

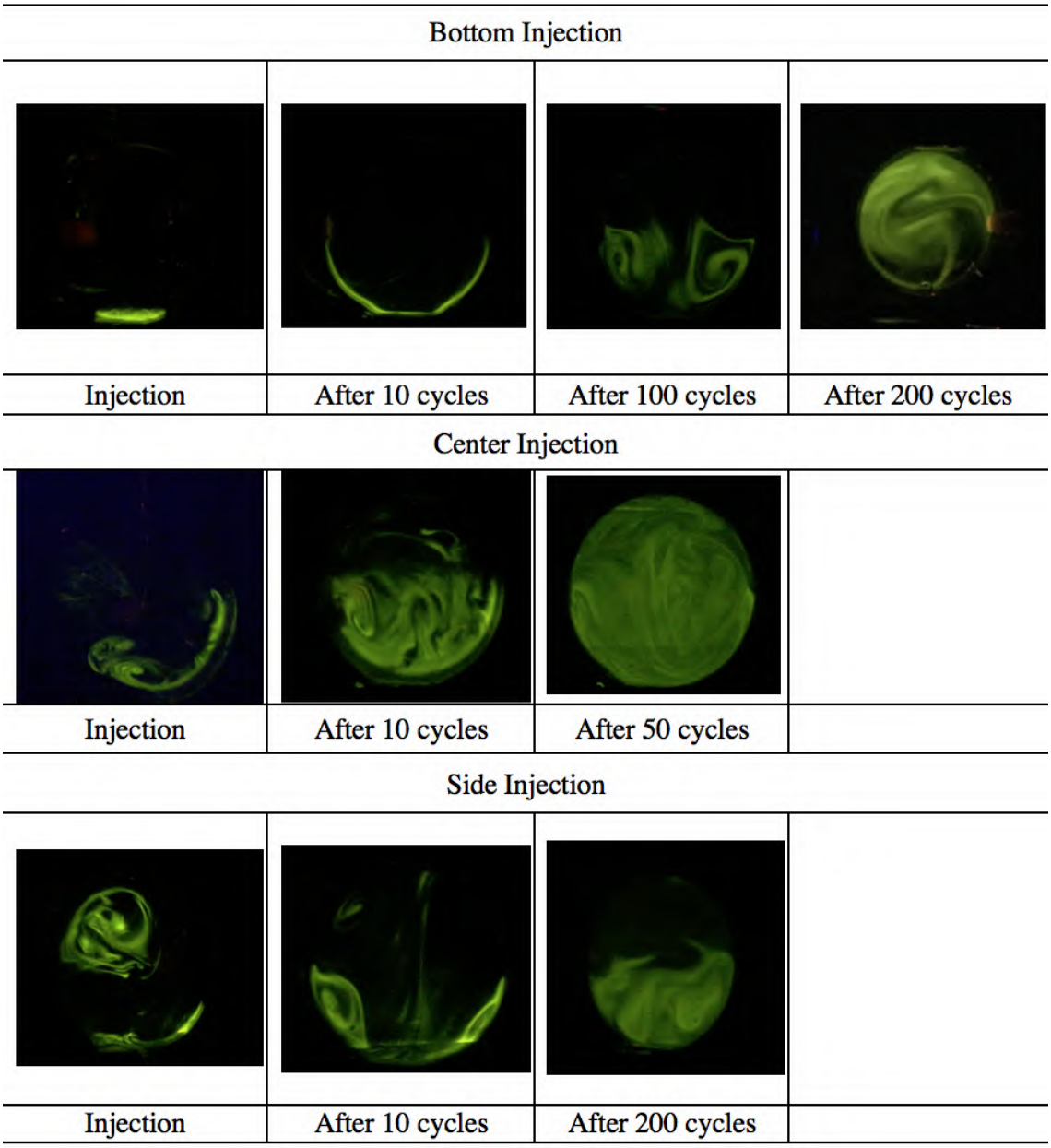

Figure 2.17: Dye visualization images from varying injection sites (From top to bottom: bottom injection, center injection, and side injection)

LIF Visualization – Viscosity Effects

As mentioned in the background section, human eye's vitreous humor property varies among different individual and changes as a person ages. To study the effect of solution property on the mixing process in the eye, glycerol and water are mixed together to generate a series of solutions with various viscosity and density. Therefore, in this set of experiments, the glycerol/water mixture was used in place of 0.9% saline to help with understanding whether lateral movements can also promote drugs mixing in a vitreous humor that is more gel-like.

After injecting drugs (glycerol/water/fluorescein mixture) into the eye model (filled with glycerol/water mixture), 10 cycles of lateral movements were introduced to the eye model in the "lateral rotation" experiment. A flow image was taken at every 10 mins for 30 mins in total. Overall, observations were made at the following five instances of time: the moment right after injection, the moment right after lateral movements stop, 10 mins after injection, 20 mins after injection, and 30 mins after injection. The same process was repeated in the "no rotation" experiment, although no rotation was involved in this process. Therefore, the second image was taken at 1 min after injection instead. (Figure 2.18)

Particle concentration is a good indicator for the mixing process, which can be reflected by the pixel intensity. In geohydrology, people use fluorescein in situations where there is insufficient lighting but precise quantitative data is required. The intensity of visible spectrum fluorescence after excitation by a certain spectrum light is measured by a fluorimeter to identify the presence and the amount of specific molecules in a medium. Taking the same idea, in our quantification process, the pixel intensity (grayscale value) was used to indicate the concentration of drug (glycerol/water/fluorescein mixture)

Pixel intensity was measured using the open source software image J. The grayscale reading function in Image J can quantify the maximum grayscale value in a defined region. As demonstrated in Figure 2.19, the area of interest was defined first so the program only calculated pixel intensity within the defined region. The location of this defined region corresponds to the location of macula in a human eye. Quantification results are summarized in Figure 2.19. Apparently, for a more viscous vitreous humor, introducing lateral movements can still promote drug mixing in the eye.

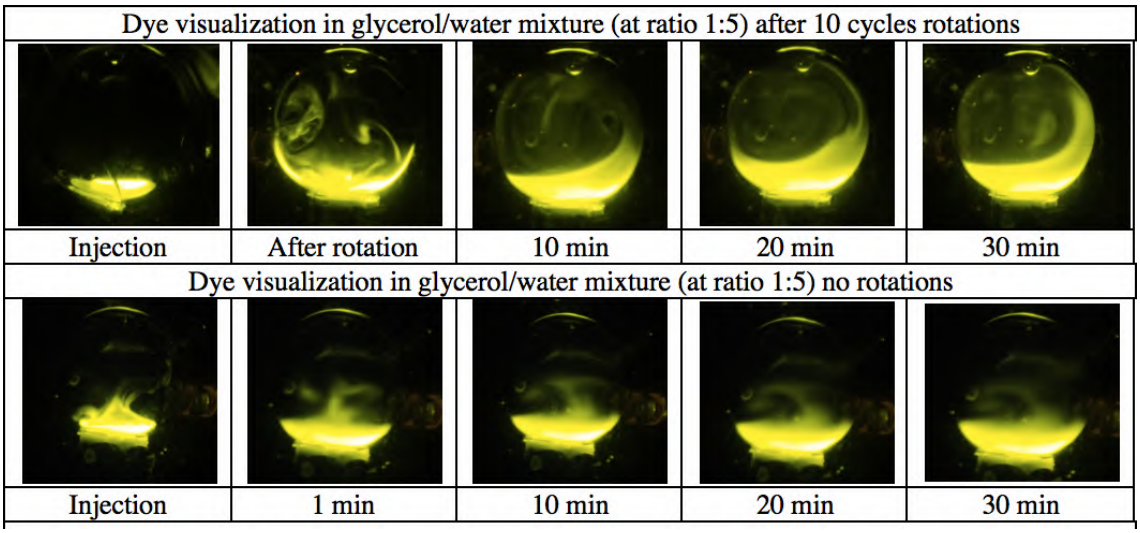

Figure 2.18: Dye visualization images (It shows observations over the course of 30 mins. Image sequence is taken immediately after injection, the moment after rotation stops, and every 10 mins afterwards.)

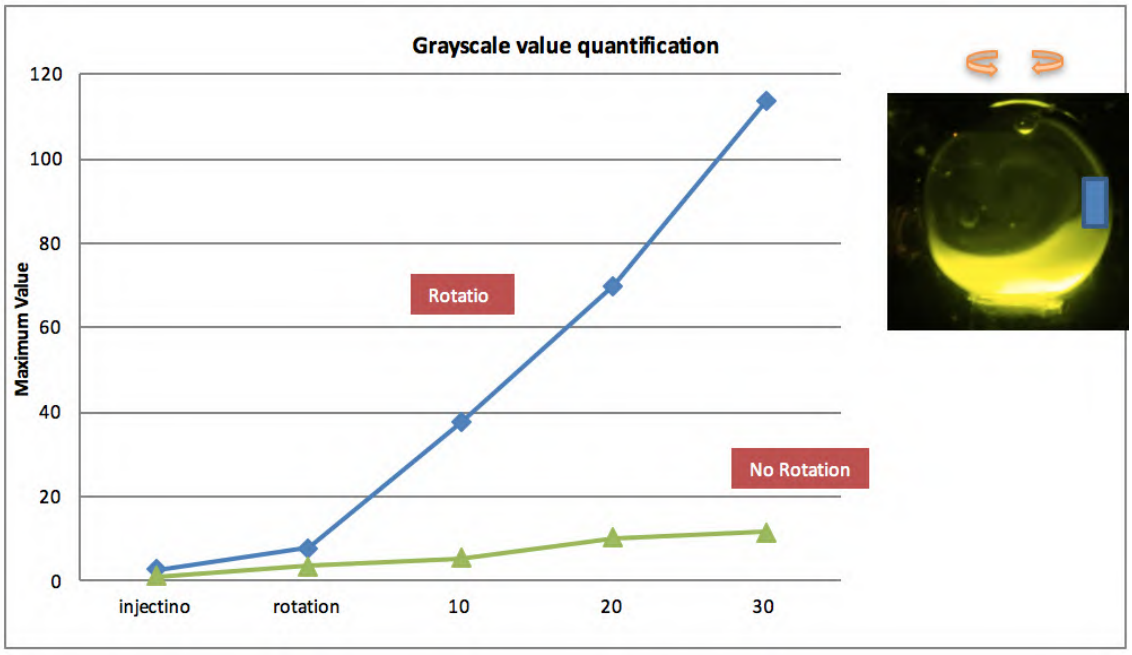

Figure 2.19: Fluorescent particle concentration reaching the target tissue (This quantifies the amount of fluorescein (drugs) that reaches the target tissue over the course of 30 mins after 10 cycles of lateral rotation)

Particle Pathline Visualization (glycerol/water mixture)

Results from previous sections show that intermittently introduced lateral rotations can facilitate a faster drug mixing in the eye. We also learned that lateral movements can be helpful even with vitreous humor of higher viscosity/density. However, in the glycerol/water mixture LIF visualization images, the four circulations weren't observed. Therefore, this inspired us to repeat the flow visualization (with fluorescent particles) that has been done with 0.9% saline, although with glycerol/water (1:5) mixture this time.

PIV visualization and PIV analysis were performed for the following three time intervals: after the first 10 cycles of lateral movements, after another 10 cycles of lateral movements, and finally after a final 200 cycles of lateral movements. The resulting raw images were then analyzed following the same PIV analysis procedures and particle pathlines were visualized in MATLAB. The resulting particle pathline visualizations were summarized in Figure 2.20, Figure 2.21, and Figure 2.22 below. Similarly, the initial positions of particles were color-coded in dark blue, then green, and finally light blue. The entire duration of particle tracking was 10 seconds, which was consistent with the analysis with 0.9% saline. During the actual experiments, no obvious circulation was observed visually. Not surprisingly, these particles didn't move as much as indicated in the pathline visualization results below: it's even hard to tell a difference between particle pathlines after 10 cycles of movements and after 200 of cycles movements.

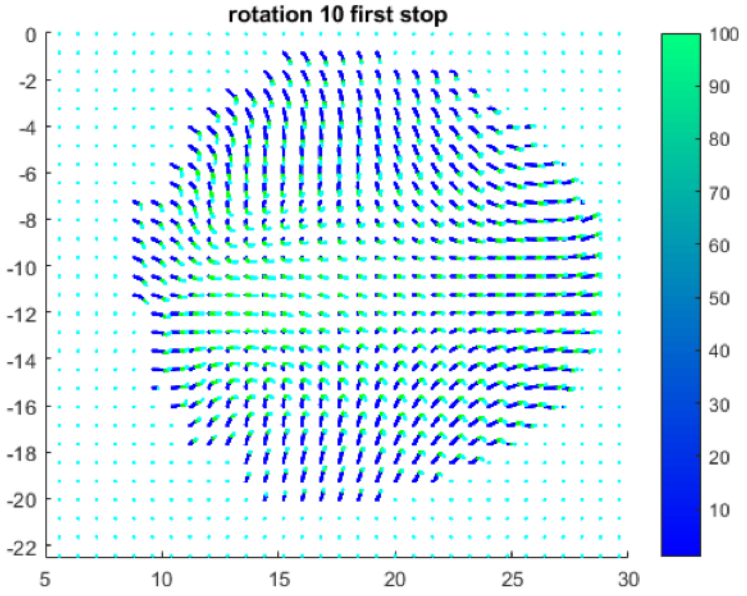

Figure 2.20: Particle pathline tracking after 10 cycles of rotation (glycerol/water mixture)

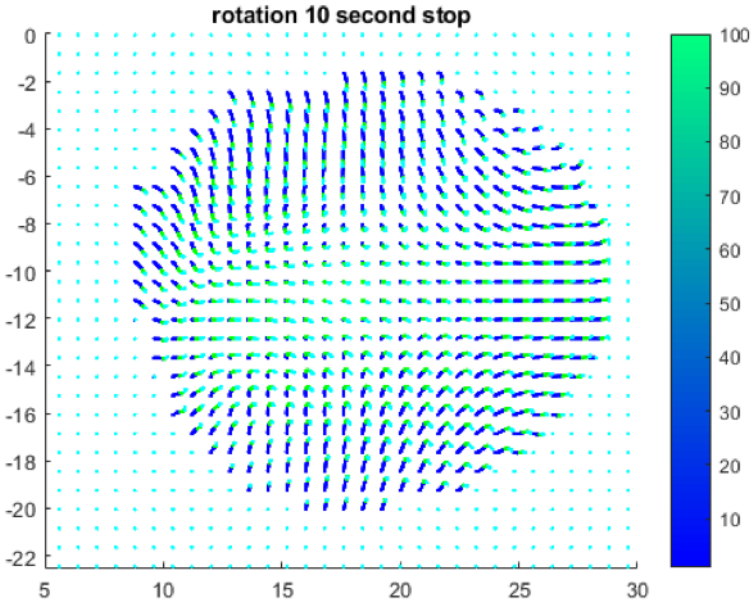

Figure 2.21: Particle pathline tracking after a second 10 cycles of rotation (observation continued from2.20

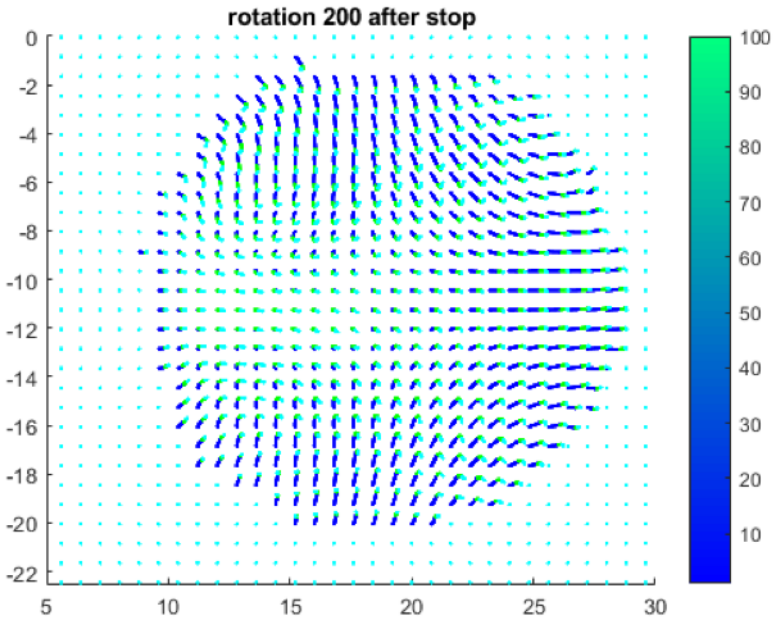

Figure 2.22: Particle pathline tracking after 200 continuous rotations (Using glycerol/water mixture)

2.4 Discussion

Dye visualization (varying injection sites)

The dye visualization results summarized in the previous sections show that center injection takes the shortest amount of time as well as the least amount of movement to mix the drug well in the eye. The bottom injection and side injection take a similar amount of movement and duration to achieve complete drug mixing in the eye. This observation could be explained further by comparing it with the results from particle pathline visualization.

We learned that lateral movements can induce four circulations. To make direct comparison, particles in the three regions of interests are highlighted in Figure 2.23 below. It is obvious that particles in the side and bottom regions are "trapped" around their initial locations. Particles that are initially in the center region have more flexibility to move towards other regions. As it was described earlier, in the clinical setting ophthalmologists tend to inject drugs at a location that is very close to the front of the eye. This might not be an optimal spot because it directly puts drug at a "side" location, which might not be so helpful in facilitating drug deliveries to the back of the eye.

Since all the previous observations of fluid patterns are made after the rotation stops, and these circulations apparently don't sustain for long enough. It has triggered our curiosity to explore an imaginary scenario where the circulations don't decay, and this could be achieved easily via MATLAB simulation. To simulate the case where circulations don't decay, the first fluid velocity field from the moment right after lateral movement stops was taken to be projected for the following instances of time. In this way, it was assumed that the velocity field with the strongest circulation was sustained (Figure 2.24). The simulation result was summarized in Figure 2.25. Similar observations can be made from this simulation result: particles that start from the center regions have more freedom to move towards other regions, whereas particles in the side/bottom regions tend to stay.

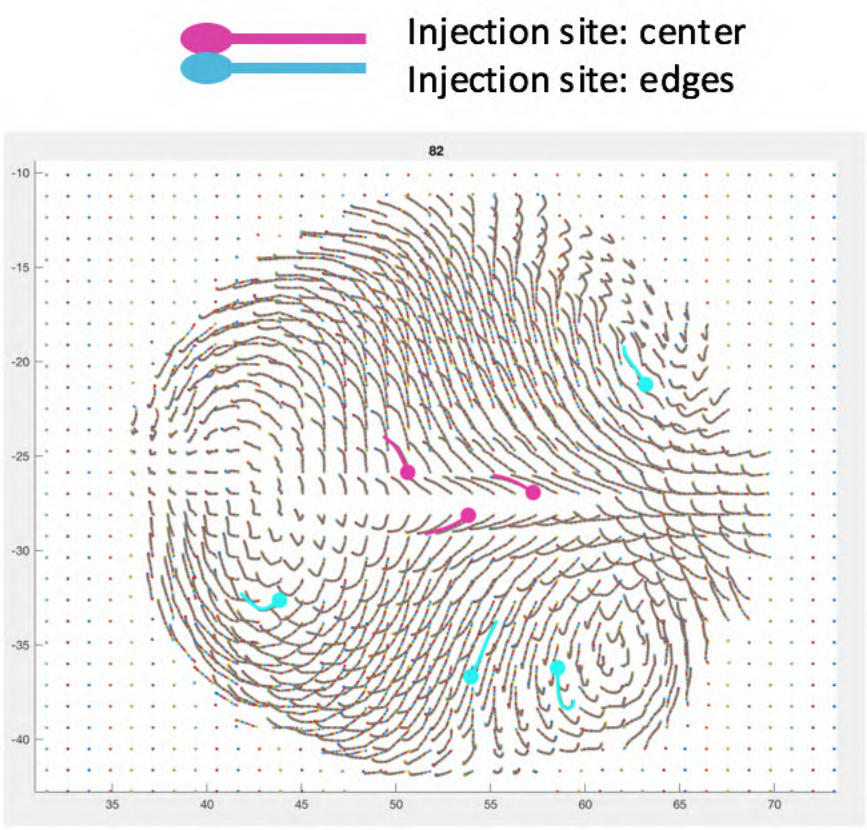

Figure 2.23: Highlighted particles in the center, bottom, and side regions. (Pink color labels particles in the center region; blue color labels particles in the side and bottom regions)

Velocity Field	$\bar{V}$ $\bar{x}$	$\bar{V}$ $\bar{x}$	$\bar{V}$ $\bar{x}$	$\bar{V}$ $\bar{x}$	$\bar{V}$ $\bar{x}$	…
	T_0	T_0	T_0	T_0	T_0	…
Time	T_0	T_1	T_2	T_3	T_4	…

Figure 2.24: Demonstration of the simulation methodology (The first velocity field is projected throughout the rest of the instances of time.)

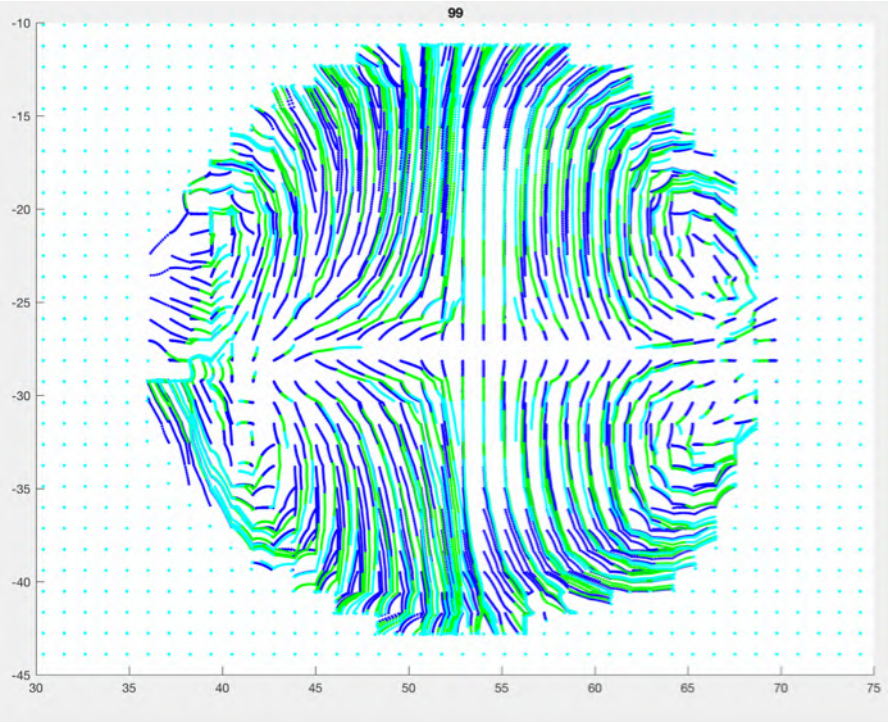

Figure 2.25: Particle pathline if the circulation doesn't decay (The velocity field is taken from the first instance of time from the PIV analysis results; particle pathline starts from dark blue to green and finally light blue.)

Variations in particle pathline tracking results (0.9% saline vs glycerol/water mixture) and the implication for the choice of eye movement frequencies

As mentioned before, four circulations were observed after introducing lateral movements to 0.9% saline but the same mixing pattern wasn't observed in the glycerol/water mixture. This discrepancy is possibly an effect of Reynolds number. Reynolds number describes the convection process over diffusion process in the flow motion. If Reynolds number is large, the convection process dominates over the diffusion process. Reynolds number can be calculated as

$$Re = \rho UD/\mu$$

where ρ is the density of fluid, U is the velocity of flow, D is the characteristic length, and μ is the dynamic viscosity.

Using the material properties as indicated in Table 2.2, Reynolds number is around 400 in the 0.9% saline case, whereas in the glycerol/water mixture case, Reynolds number is around 200 or smaller. There is likely a transition point in the range 200 < Re< 400, which determines whether the circulations can be turned on. Since ρ, μ, and D varies among different individuals and these parameters also changes over time to the same person with aging process, it's not certain that lateral movements of the eye can facilitate drug mixing for everyone, although with higher rotation speed (U), Reynolds number is higher and a possibly better mixing effect may be achievable. However, the feasibility in real life requires future in-depth studies. After all, the morphology-related factors (ρ, μ, and D) play stronger effects. Therefore, if a patient has a very viscous vitreous humor, simply increasing the eye movement frequency can hardly affect the mixing outcome.

Summary

Although applying lateral movements can introduce convective flow into the vitreous chamber and facilitate improved drug mixing, it might not be an optimal solution for the following two reasons:
1) The overall circulation effects induced by lateral movements don't sustain for long enough to ensure a continuous mixing;
2) Whether the circulations can be turned on or not depends largely on each individual's eye properties.
Since our goal is to achieve good drug mixings with minimal efforts required for the patients, we need to look for a better method. This is where thermal-driven method comes in.

Chapter 3

THERMAL EFFECTS ON FLUID MIXING IN THE EYE

3.1 Introduction

Background Introduction

This part of the study explores thermal effects on promoting drug mixing in the eye. Specifically, the following three factors are investigated to understand their effects on thermally promoting drug mixing in the eye:
1) varying temperature difference,
2) varying heating position,
and 3) varying density difference between the drug and vitreous humor.
As mentioned before, there hasn't been much study on drug mixing in the eye in the past. Limitations are primarily due to two reasons. On one hand, anatomy and physical properties of living animal vitreous structure are neither fully understood nor representative; on the other hand, since too many factors are involved and many parameters are unknown, numerical simulation is difficult.

Therefore, in our study, we approach the topic from the experimental perspective. The study outcomes will not only be meaningful for achieving fundamental understandings of fluid dynamics in the eyes, but also be helpful for ophthalmologists to optimize operation procedures for improved patient experience.

Variables of interests

The same eye model from the previous study was used in this part. To determine what temperature differences to study, it is necessary to understand the heat tolerance of the human subject first. For human beings, eyes are sensitive and thus cannot endure high temperatures for a long time. Given that the temperature limit for a human being to feel pain is 10 Celsius above body temperature, it makes sense to pick in the range of 0 – 10 Celsius temperature difference. Therefore, 5 Celsius and 10 Celsius temperature difference are selected to apply between the eye model and the heat source.

In addition, heating position is another variable to study. Different fluid motions are stimulated by placing the heat source at different positions around the eye. Some might be more aggressive than others. Therefore, this study outcome can also promote the idea of precision heating, making it possible to achieve optimal fluid mixing results without having to introduce too much temperature change to the eye. In this case, five heating positions are defined as marked in Figure 3.1. Note that the heads-up position simulates the scenario of a person who lays on the chair with his/her head facing upwards, whereas the heads-down position means the opposite.

In the previous study, drug (fluorescein/solution of interests mixture) is added to the vitreous solution (solution of interests) of the same density/viscosity. However, in this study, the effects of introducing density/viscosity difference between the injected drug and the vitreous are studied. This can give us a more realistic angle in understanding how drugs are delivered in various environments. More details regarding solution preparations are explained in the following sections.

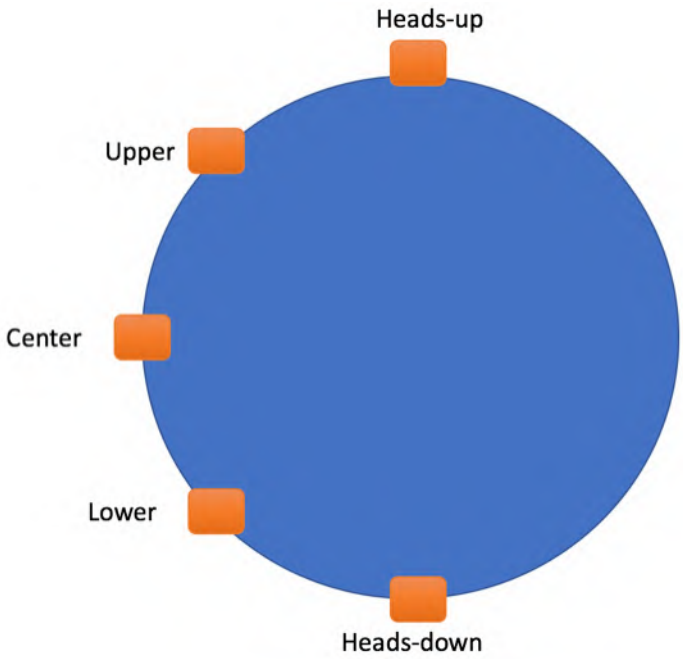

Figure 3.1: Five heating positions around the eye (Upper, center, and lower positions are defined in terms of a person sitting upright; the heads-up position simulates the scenario of a person who lays on the chair with his/her head facing upwards, whereas the heads-down position means the opposite.

3.2 Materials and Methods

Vitreous Humor Preparation

To prepare for liquid that goes into the container, glycerol and water at various water-to-glycerol ratios (5:1, 5:2, and 10:1 respectively) were made in bulk. Each set of mixtures was placed in the room temperature for more than 48 hours to ensure a consistent initial temperature. It is worth noting that glycerol/water (1:5) mixture has physical properties (density and viscosity) that are most similar to vitreous humor in the eye. Table 2.2 should be revisited to make reference to the water/glycerol mixtures that are used in this study and their respective physical properties.

Heat Source Fabrication

The heat source for inducing temperature gradient was composed of a steel stick, a polyimide flexible heater (OMEGA Engineering, KHLVA-0502), an aluminum piece, and a voltage box. The aluminum piece was made at the Caltech GALCIT machine shop. The curvature was customized and tested a few times until the aluminum piece could make a good contact area with the existing eye model. The effective contact area was approximately 5 mm by 5 mm. A demonstration of the entire heating element assembly is shown in Figure 3.2 below. After successfully putting the parts together, the heating element assembly was then completely covered by black tape. This ensured that the metal part would not interfere with the laser path during a visualization session. (Figure 3.3)

A calibration experiment was designed to obtain a voltage-temperature relationship. This facilitated an indirect but accurate temperature control via voltage reading. During the calibration process, voltage input was increased incrementally by 2 Volts at a time. Temperature readings were obtained using a digital thermometer. After each voltage adjustment was made, a temperature reading was recorded after it became stabilized for at least 10 mins. Temperatures at two locations were measured, denoted as A and B in Figure 3.2. The calibration process was repeated a few times to ensure its accuracy. This voltage-temperature curved was referenced for temperature control throughout this study.

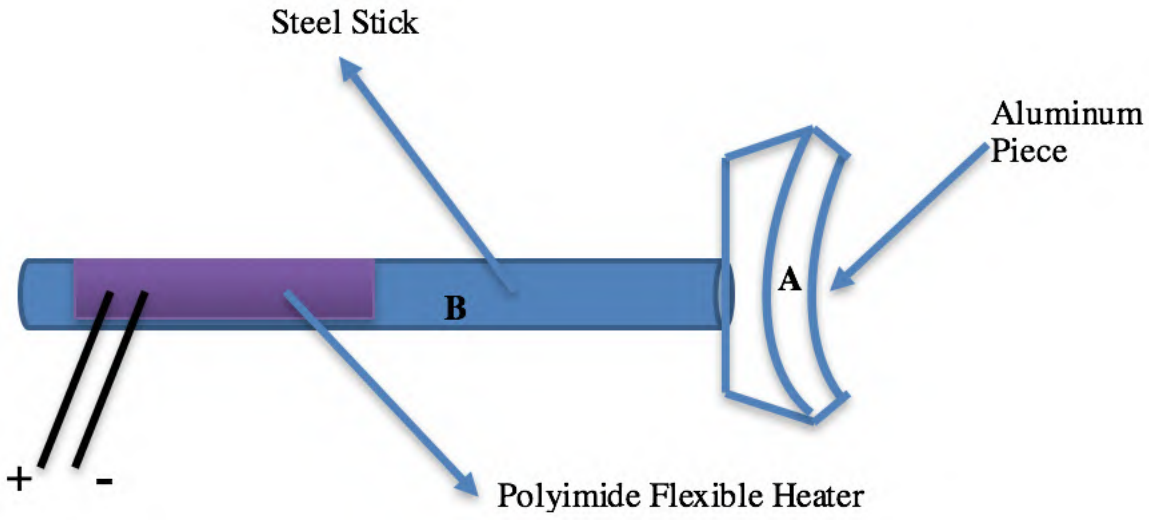

Figure 3.2: Key components of the heating source (There are three major components: the solid blue part represents the steel stick; the yellow part represents polyimide flexible heater which sits on top of the steel stick, the two cables are connected to the power box, and the hollow blue part represents the customized aluminum piece.)

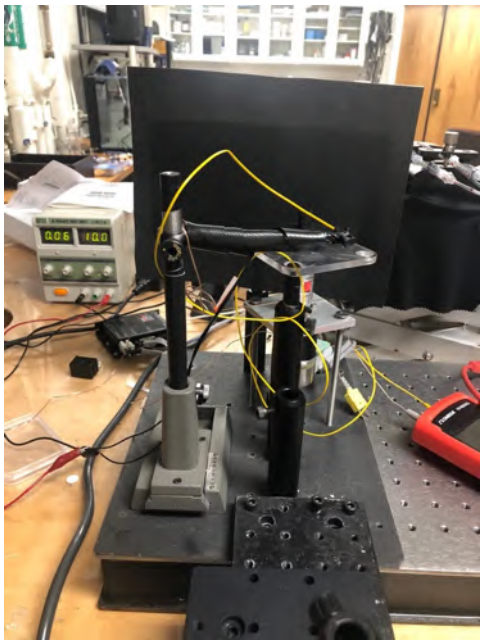

Figure 3.3: Heating element assembly wrapped with black tapes

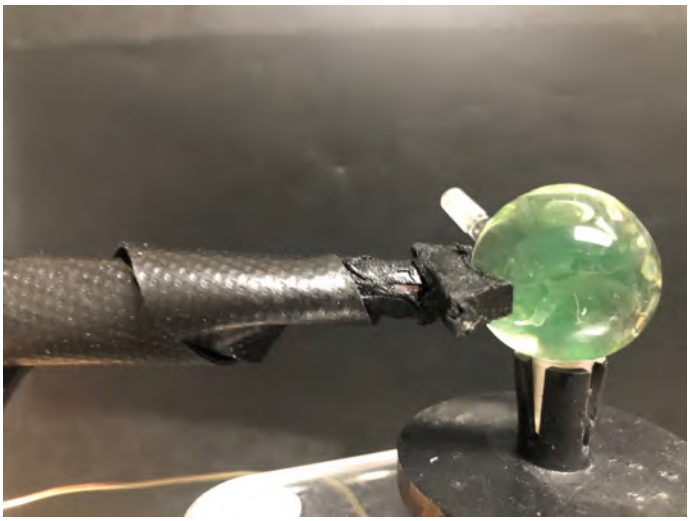

Figure 3.4: Heating element at the “center” heating location

PIV Visualization

Same imaging techniques were used in this study. Therefore, most of the PIV visualization procedures were the same as before, and thus the same set-up details would not be repeated in this section. For fluorescence particles, silver coated fluorescence particles were used in place of Kodak fluorescence particles. The silver coated fluorescence particles were heavier. To prepare for solutions for PIV visualizations, a spoonful of silver coated fluorescence particles was mixed with the solution of interests. After these particles were settled and stratified in the solution, only the middle layer was captured for use in PIV visualization. (Figure 3.5) The flow profile was observed and captured at 10 frame per second (fps) for a duration of 10 mins after the heat source was applied.

For laser induced fluorescence visualization (FIL), fluorescein was first dissolved in water and then mixed with solution of interests at 1:50 ratio (fluorescein to solution of interests = 1:50). Since density and viscosity of glycerol/water (1:5) mixture is the most similar to those of human vitreous humor’s, glycerol/water (1:5) mixture is the primary working solution to fill up the eye model. Glycerol/water (1:10) mixture and glycerol/water (2:5) mixture were mixed with fluorescein at 1:50 (fluorescein: solution) ratio. Adding glycerol/water/fluorescein (2:5) mixture to the eye model simulates the process of adding drug that is heavier and more viscous than the vitreous humor to the eye; whereas adding glycerol/water/fluorescein (1:10) mixture to the eye model simulates the process of adding a lighter and less viscous

drug to the eye.

As mentioned before, pixel intensity is correlated with drug (glycerol/water/ fluorescein mixture) concentration. Therefore, to quantify the amount of drug (glycerol/water/fluorescein mixture) that have entered target treatment region, the image tool in MATLAB was used for pixel intensity quantification. MATLAB was used in place of ImageJ here because it facilitated mass processing of thousands of images. Figure 3.6 below shows a screenshot of imaging processing using the image tool in MATLAB. The area of interest was defined as a 5-pixel by 20-pixel rectangle located near the center of the eye model on the right side. The location of this region corresponds to the actual position of the macula, which is the desired AMD treatment spot in the eye. The size and location of this region were kept the same throughout all image quantifications.

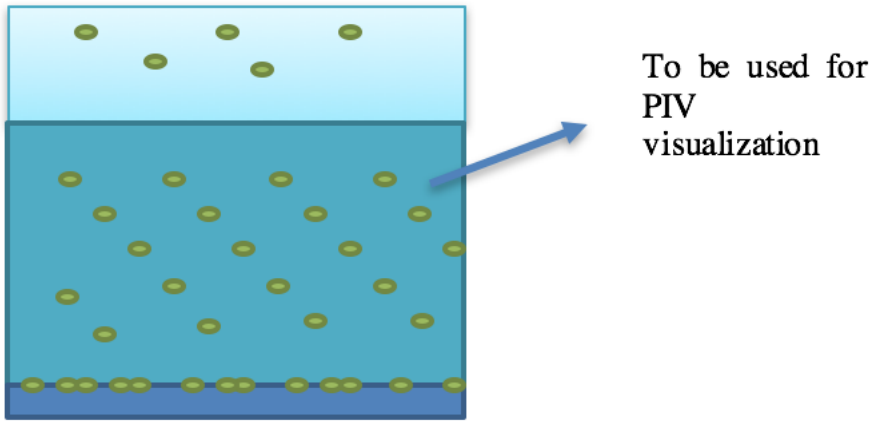

Figure 3.5: Stratified silver-coated particles/glycerol/water mixture The heaviest particles stay at the bottom whereas the lightest ones float in the top region. Only the middle portion is suitable for visualization purpose as particles in this region share approximately the same density with the glycerol/water mixture.

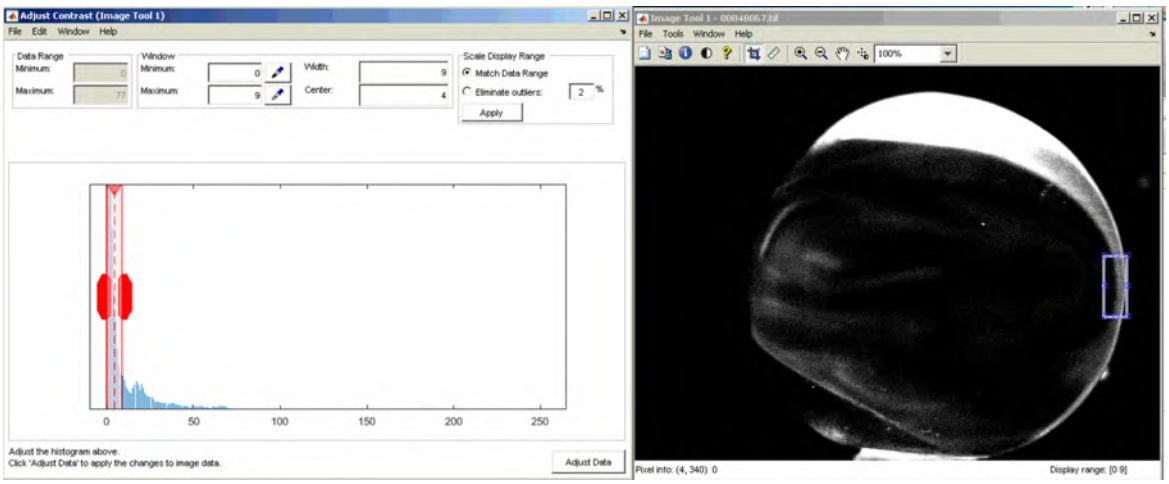

Figure 3.6: Pixel intensity quantification using the image tool in MATLAB (The purple box highlighted in the picture on the right defines the area of interests for pixel intensity quantification. When fluorescein is excited by the laser, it becomes bright/white in the image. In this image, fluorescein is distributed in the top right region.)

Pathline Visualizations Using ImageJ

The idea of using ImageJ to visualize particle pathline is the same as using MATLAB programming to track particle pathlines. The "Grouped Z Project" tool in ImageJ allows for overlaying a particle image sequence onto a single image (z-projection), and the overall range of time of the image sequence can also be determined. The total duration of each flow visualization session was 10 mins at 10 fps. Therefore, a total of 6,000 images were taken for each flow visualization session. Using the "Grouped Z Project" tool, these 6,000 images were segregated into 60 groups. Then a z-projection was performed on the 100 images in each group. The result was a new stack of images, one slice for each group.

CFD Simulation Using FEATool Multiphysics

A computation study was conducted with the aid of FEATool Multiphysics/MATLAB. The fluid has thermal diffusivity α and viscosity ν. Rayleigh number for this flow is defined as

$$Ra = \frac{g\beta\delta T x^3}{\alpha\nu} = 8300$$

for water/glycerol (5:1) mixture at δT= 10 Celsius, and Prandtl number is defined as

$$Pr = \frac{C_p\mu}{k} = 13.48$$

for water/glycerol (5:1) mixture. Note that δT is the temperature difference between the heat source and the eye model. All lengths are non-dimensionalized with respect to D, the diameter of eye model; all velocities with respect to α/D ; time with respect to D^2/α; vorticity with respect to α/D^2 temperature with respect to δT. The study object was modeled as a two-dimensional viscous Boussinesq fluid in a circular domain, and the equations for numerical modeling are listed below: ((Moore and Davis, 1984))

$$\frac{\partial U}{\partial X} + \frac{\partial V}{\partial Y} = 0 \tag{3.1}$$

$$\frac{\partial U}{\partial \tau} + U\frac{\partial U}{\partial X} + V\frac{\partial U}{\partial Y} = -\frac{\partial P}{\partial X} + Pr(\frac{\partial^2 U}{\partial X^2} + \frac{\partial^2 U}{\partial Y^2}) \tag{3.2}$$

$$\frac{\partial V}{\partial \tau} + U\frac{\partial V}{\partial X} + V\frac{\partial V}{\partial Y} = -\frac{\partial P}{\partial Y} + Pr(\frac{\partial^2 V}{\partial X^2} + \frac{\partial^2 V}{\partial Y^2}) + RaPrT \tag{3.3}$$

$$\frac{\partial T}{\partial \tau} + U\frac{\partial T}{\partial X} + V\frac{\partial T}{\partial Y} = \frac{\partial^2 T}{\partial X^2} + \frac{\partial^2 T}{\partial Y^2} \tag{3.4}$$

3.3 Results

Pathline Visualization Using Image J

This section summarizes pathline visualization results using Image J. The algorithm was explained in the previous section. Flow visualization was performed on the following six cases:
1) 5-degree temperature difference (center position heating, Figure 3.7),
2) 10-degree temperature difference (center position heating, Figure 3.8),
3) 10-degree temperature difference (lower position heating, Figure 3.9),
4) 10-degree temperature difference (upper position heating, Figure 3.10),
5) 10-degree temperature difference (heads-up heating, Figure 3.11),
and 6) 10-degree temperature difference (heads-down heating, Figure 3.12).
During each session, a total of 6,000 images were taken. After performing a z-projection, there were 60 slices of 100 images in each slice for every case. Only one slice from each case was selected to be included in this section, and these slices are all captured during 5 mins to 5 mins and 10 second in each experiment. In addition, a slice of 100 images taken before the heating source was applied was also included as a control case. (Figure 3.13)

Figure 3.7: Pathline visualization from 5-celsius temperature difference (center heating) These 100 images were taken from 5 mins to 5 mins and 10 secs. Note that most of the flow behavior was happening on the left half of the eye model.

Figure 3.8: Pathline visualization from 10-celsius temperature difference (center heating) These 100 images were taken from 5 mins to 5 mins and 10 secs. Note that the flow was stronger compared with the one in Figure 3.7a, although circulation was relatively weak at the very bottom of the eye model.

Figure 3.9: Pathline visualization from 10-celsius temperature difference (lower heating) These 100 images were taken from 5 mins to 5 mins and 10 secs. Note that circulations were fully activated across all regions in the eye model.

Figure 3.10: Pathline visualization from 10- Celsius temperature difference (upper heating) These 100 images were taken from 5 mins to 5 mins and 10 secs. Note that most of the flow behavior was happening on the top part of the eye model.

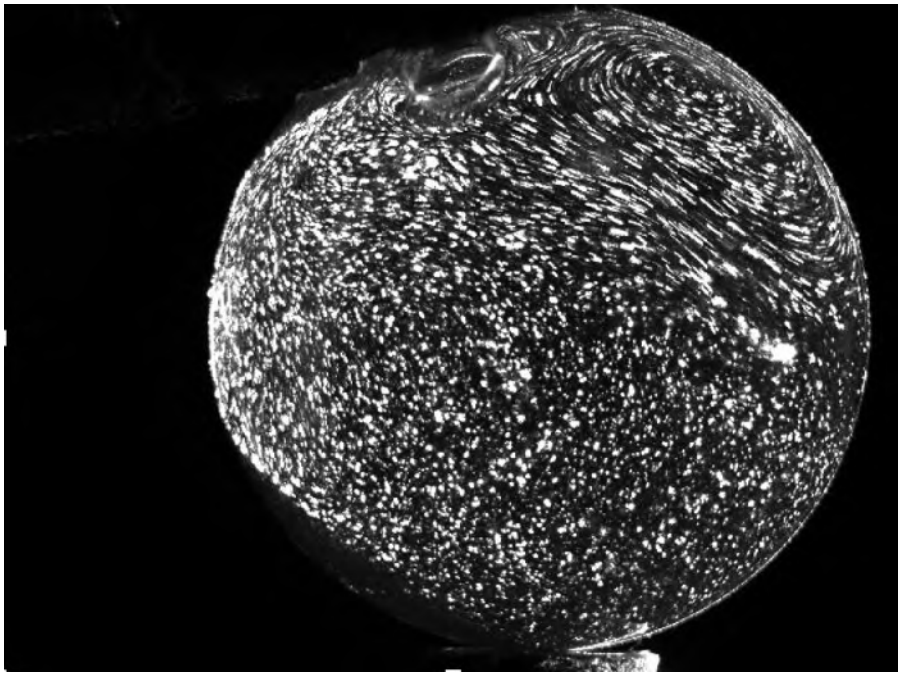

Figure 3.11: Pathline visualization from 10- Celsius temperature difference (heads-up heating) These 100 images were taken from 5 mins to 5 mins and 10 secs. Note that the overall flow behavior was not quite strong.

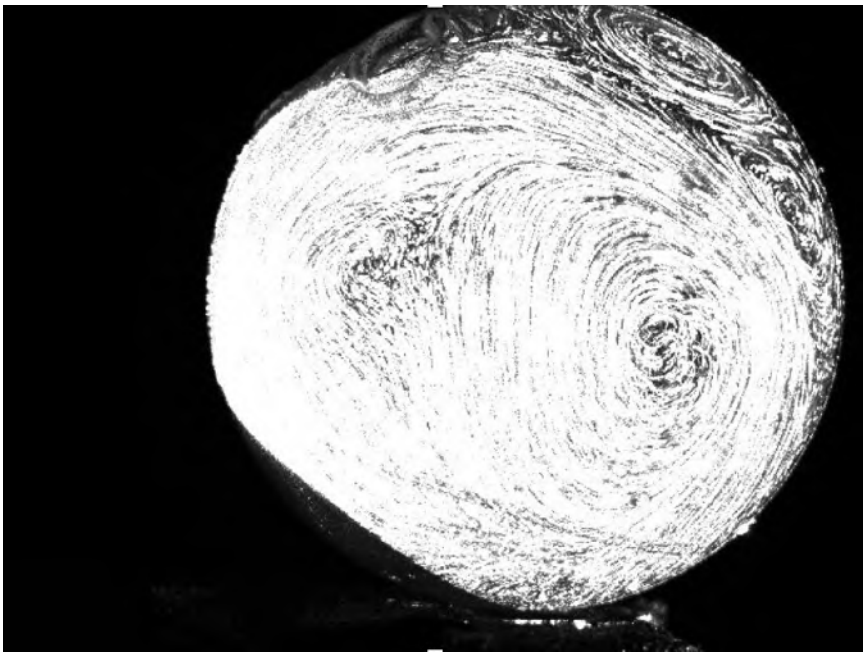

Figure 3.12: Pathline visualization from 10-Celsius temperature difference (heads-down heating) These 100 images were taken from 5 mins to 5 mins and 10 secs. Note that the flow behavior was very strong. It's very hard to describe a distinct pattern from this image.

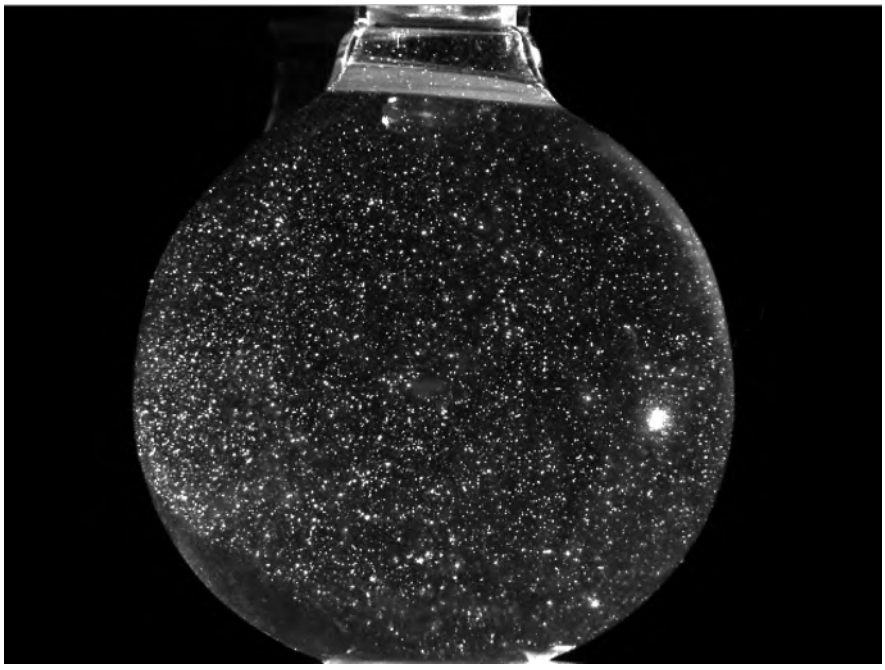

Figure 3.13: Pathline visualization before the heat source was applied. These 100 images were taken for a duration of 10 seconds.

Apparently, a greater temperature difference can activate stronger circulations in the eye model. For a person who's standing/sitting in the upright position, heating from the lower position can activate mixing in the entire eye model, whereas center and upper heating can only activate partial mixing in the eye model. For a person who's laying down on the chair with his/her head facing up, placing a heat source on top of his/her eyes doesn't seem to help with mixing, whereas having his/her head facing down instead can possibly induce very aggressive mixings in his/her eyes. The same conclusion can be drawn from quantification of flow circulation as shown in figure 3.14. Clearly, both heating from lower position at = 10 Celsius and heating at the heads-down position induce strong rotational motions of the flow in the eye model.

In summary, lower heating for someone in the upright position as well as heating from a heads-down position can be very helpful in achieving our goal to facilitate efficient drug mixing in the eye after an intravitreal injection.

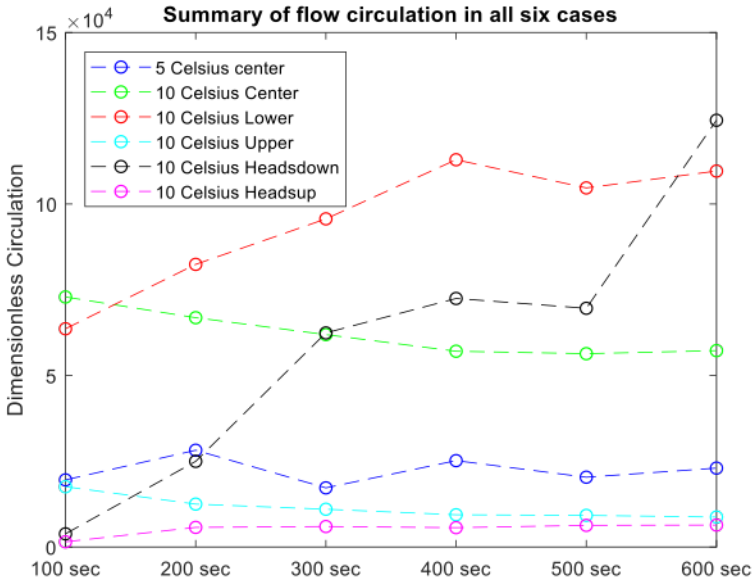

Figure 3.14: Circulation represents the rotational motion of flow in the eye model. Here, we took the absolute value of circulation in each case.

Pathline Visualization Using MATLAB

Vorticity plots can help us understand the intensity of mixing. Regions of high vorticity magnitude typically correspond to regions of stronger shear or fluid circulation. The sign of the vorticity provides the direction of fluid circulation. The average magnitude of vorticity in each case over the course of 5 seconds (from 5 mins to 5 mins and 5 seconds) is summarized in the vorticity plot below. In comparison, particle pathline tracking for the same duration was generated using MATLAB. (Figure 3.15) The algorithm for generating pathline visualization using MATLAB was described in the previous section. This pathline tracking is slightly different from the pathline visualization using ImageJ since the resulting images are more explicit in showing the particle trajectories. However, the fundamental idea is the same. Overall, observations obtained from vorticity plot and pathline visualization are consistent with the conclusions in the previous section.

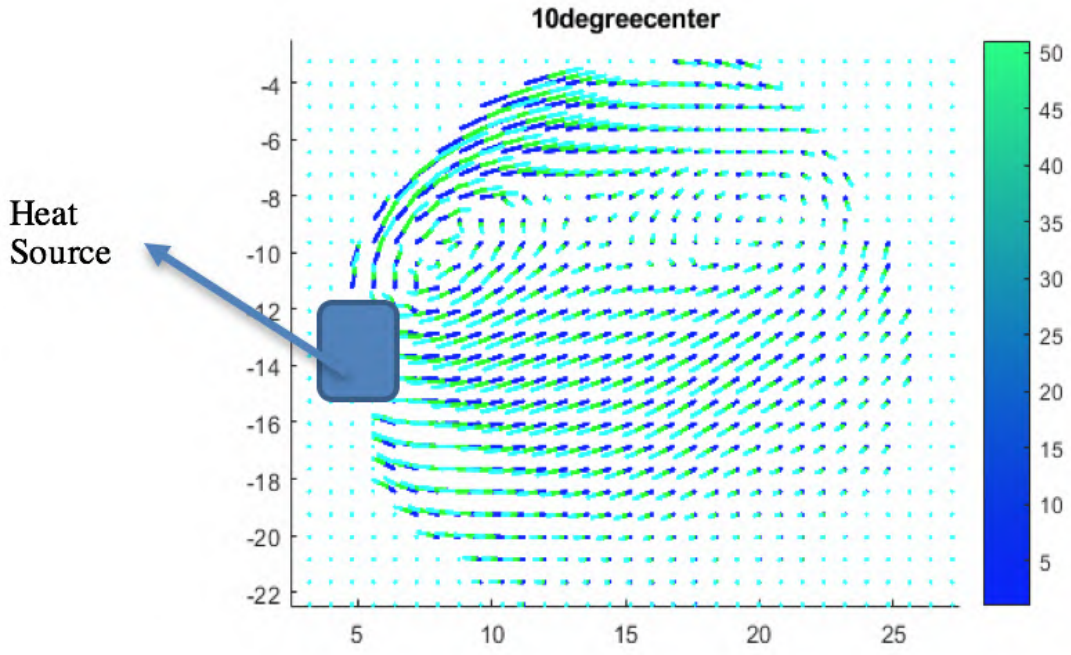

Figure 3.15: An example of pathline visualization using MATLAB. (The position of heat source is marked in the plot.)

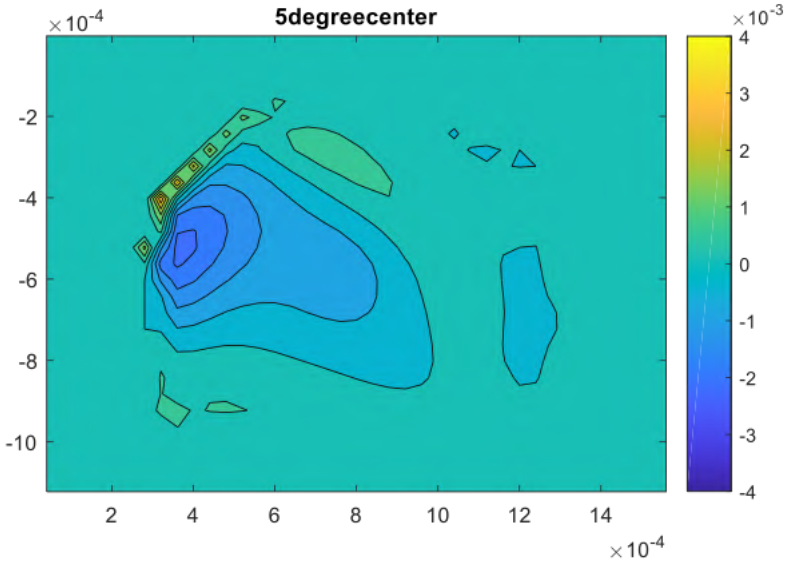

Figure 3.16: Average vorticity plot from $\delta T = 5$ Celsius (center heating)

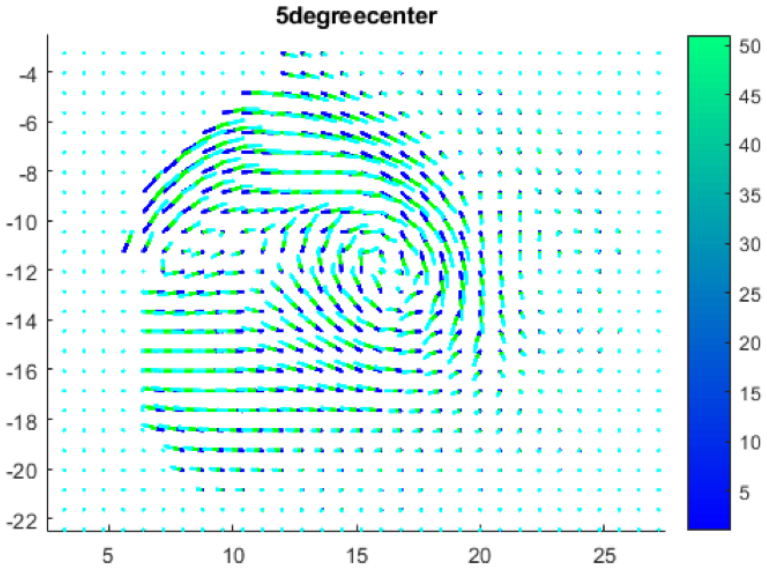

Figure 3.17: Pathline visualization from $\delta T = 5$ Celsius (center heating)

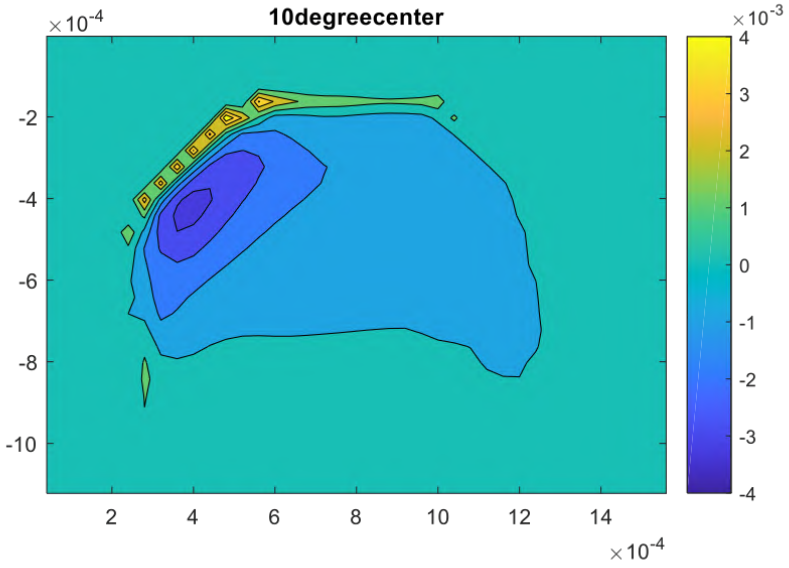

Figure 3.18: Average vorticity plot from $\delta T = 10$ Celsius (center heating)

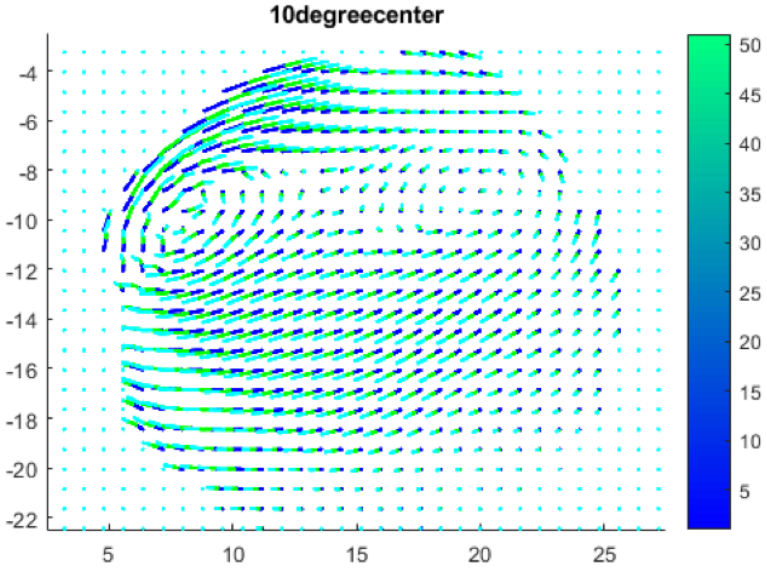

Figure 3.19: Pathline visualization from $\delta T = 10$ Celsius (center heating)

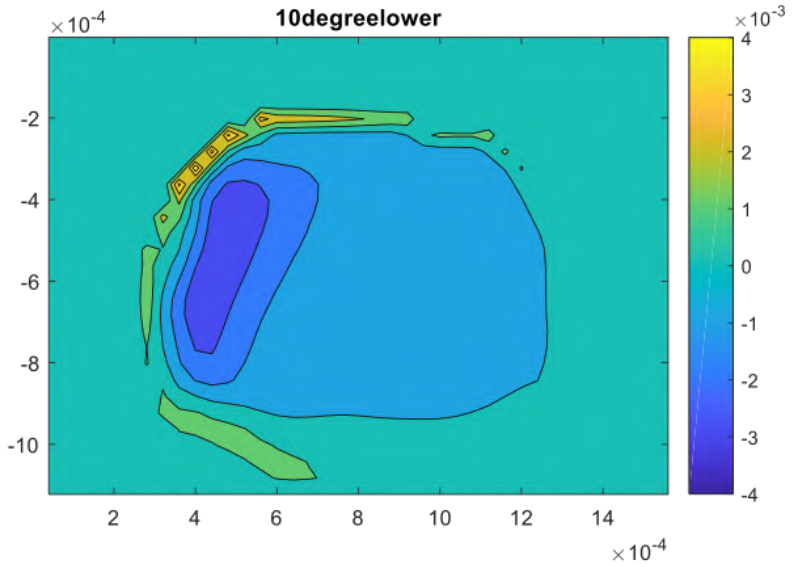

Figure 3.20: Average vorticity plot from $\delta T = 10$ Celsius (lower heating)

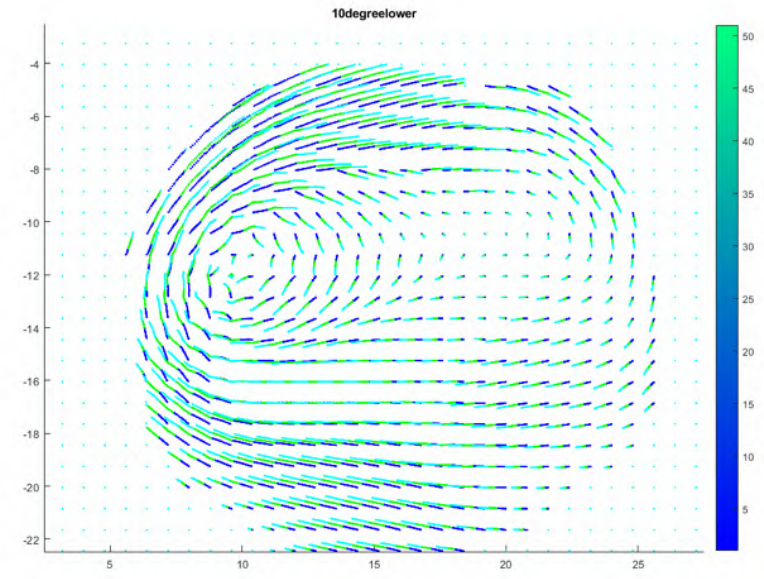

Figure 3.21: Pathline visualization from $\delta T = 10$ Celsius (lower heating)

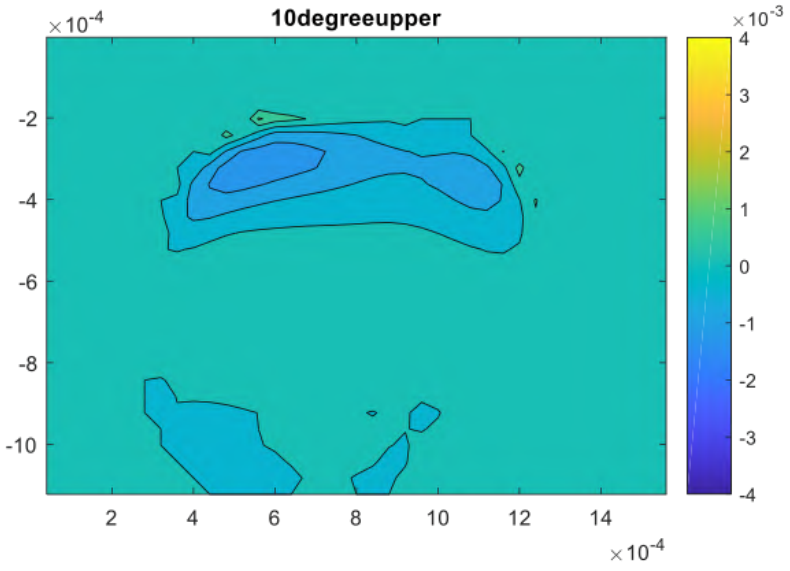

Figure 3.22: Average vorticity plot from $\delta T = 10$ Celsius (upper heating)

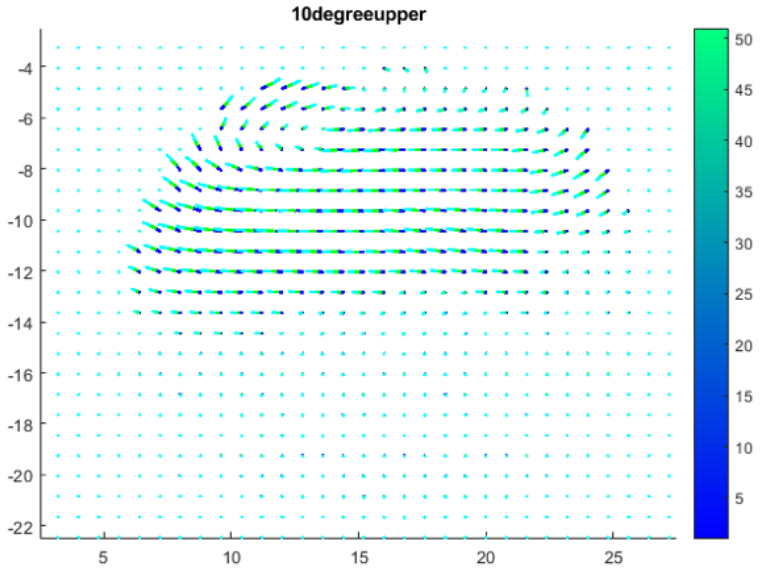

Figure 3.23: Pathline visualization from $\delta T = 10$ Celsius (upper heating)

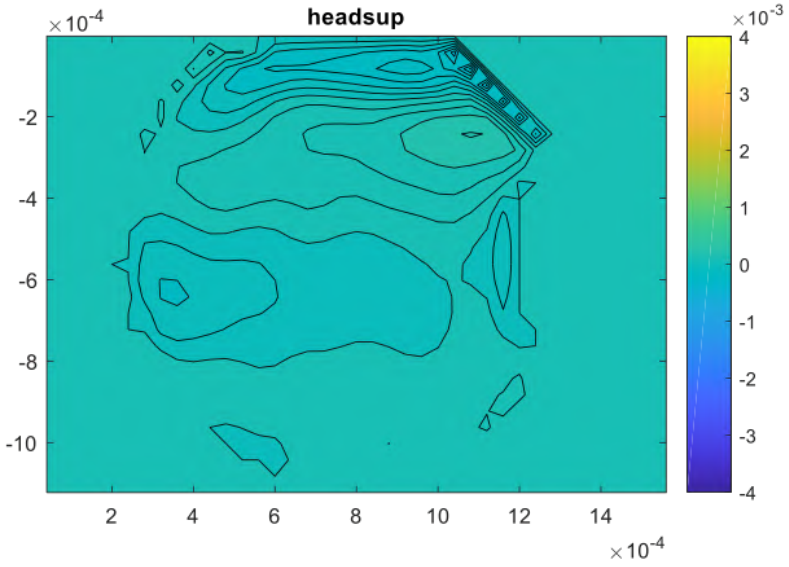

Figure 3.24: Average vorticity plot from $\delta T = 10$ Celsius (heads-up)

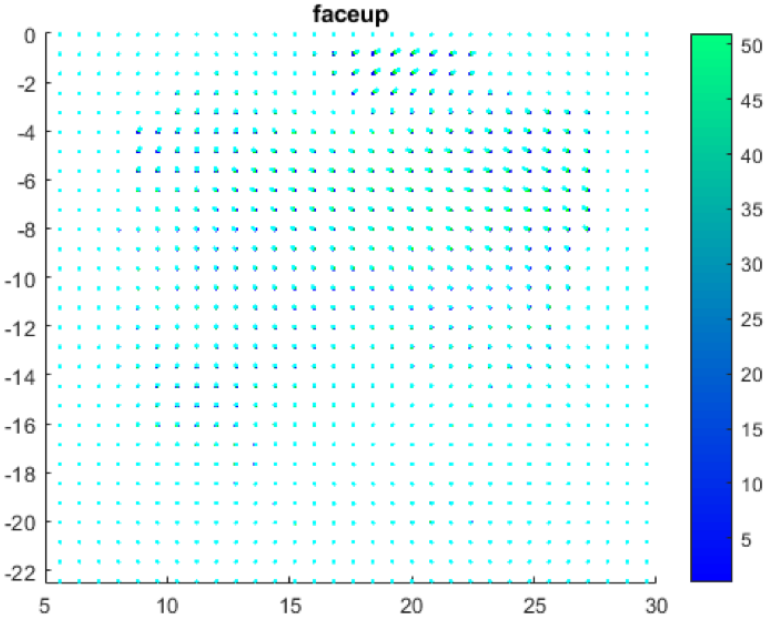

Figure 3.25: Pathline visualization from $\delta T = 10$ Celsius (heads-up)

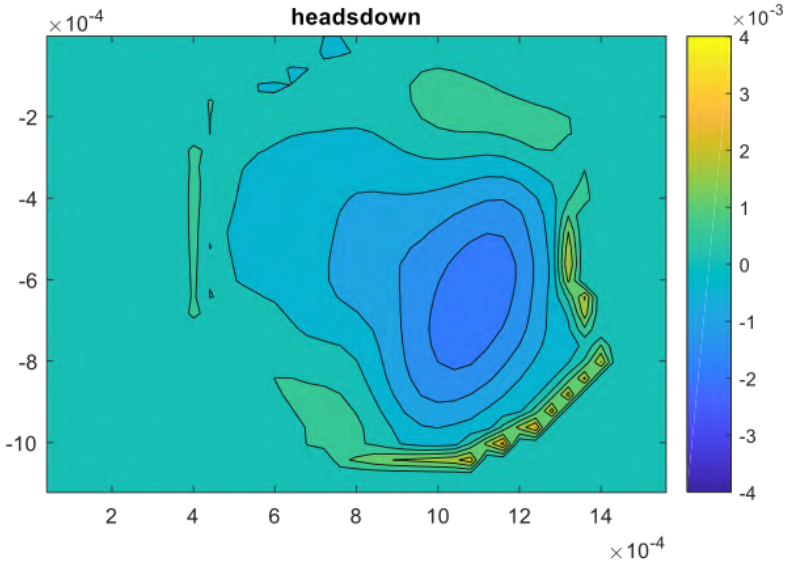

Figure 3.26: Average vorticity plot from $\delta T = 10$ Celsius (heads-down)

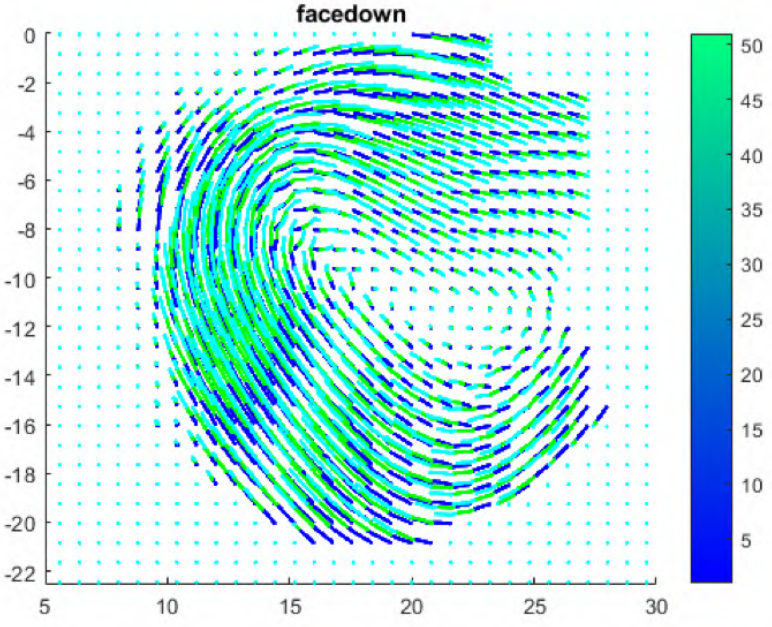

Figure 3.27: Pathline visualization from $\delta T = 10$ Celsius (heads-down)

To facilitate a better understanding of the impact of varying temperature gradient and heating position on the trajectory of individual particles, data obtained from PIV analysis were analyzed in MATLAB and variables including u, v, x, y, and t were coordinated to track individual particle behavior. Here, three scenarios were compared: $\delta T = 5Celsius$ center heating, $\delta T = 10Celsius$ center heating, and $\delta T = 10Celsius$ lower heating. The results are summarized in Figure 3.28,3.29,3.30. For a 2D analysis, it was assumed that a disk-shaped drug (radius = 0.4 cm) was injected into the center plane of the vitreous chamber (radius = 11 cm). The initial position of the drug in all three scenarios were kept the same and the goal was to observe the time duration it took for the particle to reach the back of the eye during the 10 mins heating process. The position of macula is in the back of the eye, which corresponds to the middle section of the right-side boundary of the circular domain. Since particles tend to move along the curvature once they are near the boundary, we claim that the particle delivery is successful as soon as it reaches the boundary on the right.

As it is demonstrated in Figure 3.28, 3.29, and 3.30, heating from a lower position at $\delta T = 10Celsius$ helped the particle to deliver within the shortest time (less than 200 seconds); heating from the center position at $\delta T = 10Celsius$ trapped the particle in a flow circulation during the first 400 seconds but the particle could delivery successfully by the end of 600 seconds (10 mins); heating from the center position at $\delta T = 5Celsius$ was not helpful. The results are consistent with observations from the previous pathline visualizations.

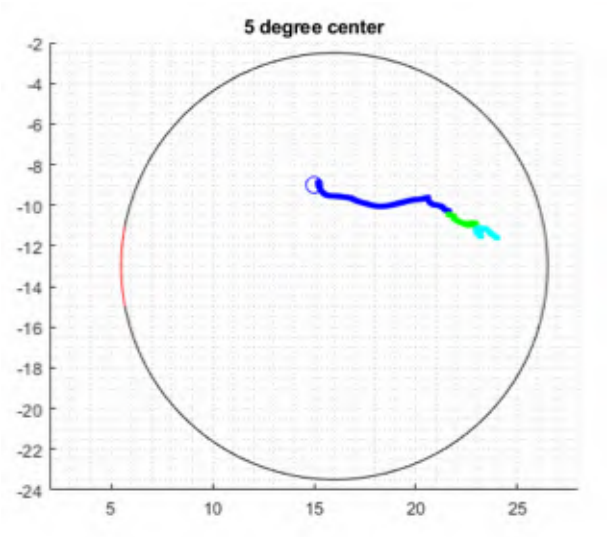

Figure 3.28: Individual particle tracking for $\delta T = 5Celsius$, heating from the center. The blue circle indicates the initial position of the particle; dark blue line indicates particle movements during the first 200 seconds; green line indicates particle movements during the second 200 seconds, and light blue line indicates particle movements during the last 200 seconds. Heating position is marked in red along the circular boundary.

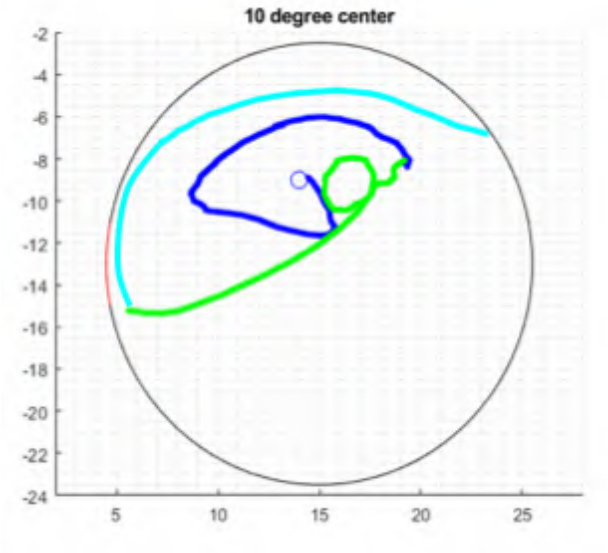

Figure 3.29: Individual particle tracking for $\delta T = 10Celsius$, heating from the center. The blue circle indicates the initial position of the particle; dark blue line indicates particle movements during the first 200 seconds; green line indicates particle movements during the second 200 seconds, and light blue line indicates particle movements during the last 200 seconds. Heating position is marked in red along the circular boundary.

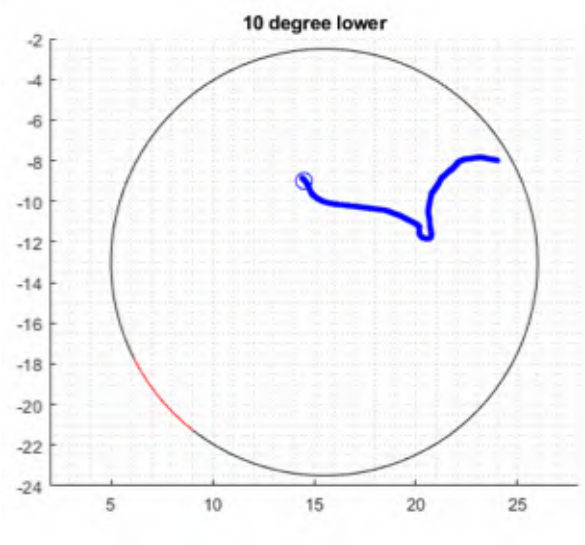

Figure 3.30: Individual particle tracking for for $\delta T = 10 Celsius$, heating from the lower position. The blue circle indicates the initial position of the particle; dark blue line indicates particle movements during the first 200 seconds; green line indicates particle movements during the second 200 seconds, and light blue line indicates particle movements during the last 200 seconds. Heating position is marked in red along the circular boundary.

Quantification Results from LIF Visualization

To simulate the actual drug delivery process, LIF visualization was performed on the following four cases:
1) Adding water/glycerol (5:2) drug mixture into water/glycerol (5:1) vitreous mixture with center heating; (Figure 3.31 and 3.32)
2) Adding water/glycerol (5:2) drug mixture into water/glycerol (5:1) vitreous mixture with lower heating; (Figure 3.33 and 3.34)
3) Adding water/glycerol (10:1) drug mixture into water/glycerol (5:1) vitreous mixture with center heating; Figure 3.35 and 3.36)
4) adding water/glycerol (10:1) drug mixture into water/glycerol (5:1) vitreous mixture with lower heating; Figure 3.37 and 3.38)

The maximum pixel intensity reading from each heating method is summarized in Table 3.1. In summary, when drugs are heavier than the vitreous humor, heating from the center is not so helpful for facilitating drug mixing in the eye. When drugs are lighter than the vitreous humor, both center heating and lower heating are useful and can induce strong drug mixing profiles within an hour. Lower heating can activate strong drug mixing regardless of the density of the drug.

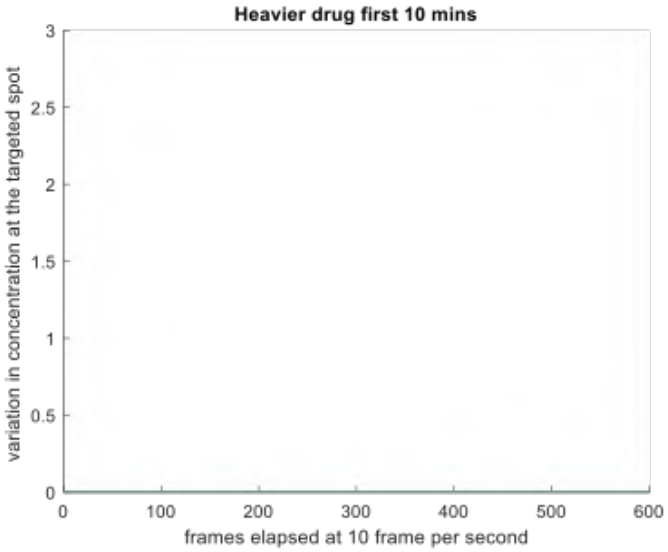

Figure 3.31: Pixel Intensity Quantification Results from LIF Visualization: Heavier drug and center heating during the first 10 mins.

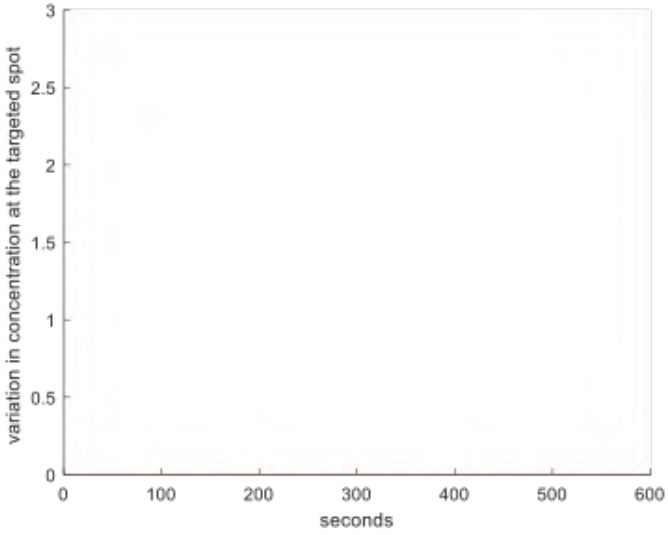

Figure 3.32: Pixel Intensity Quantification Results from LIF Visualization: Heavier drug and center heating during the last 10 mins.

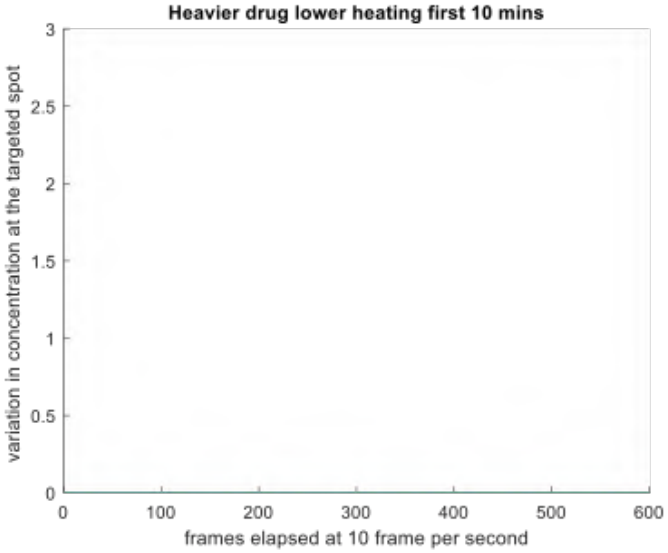

Figure 3.33: Pixel Intensity Quantification Results from LIF Visualization: Heavier drug and lower heating during the first 10 mins.

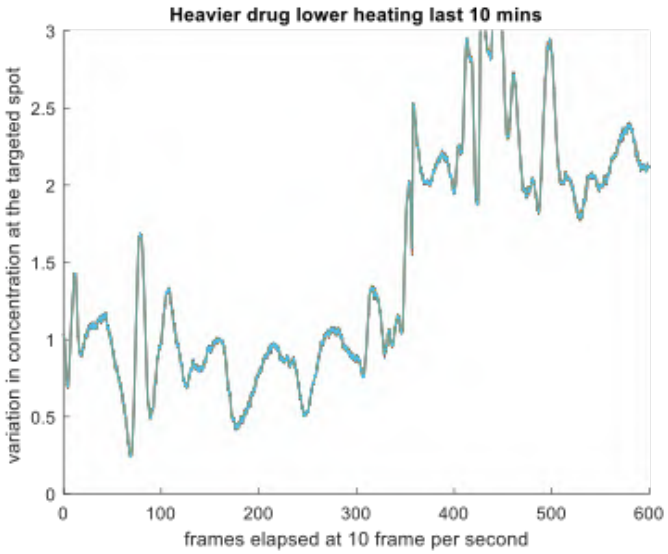

Figure 3.34: Pixel Intensity Quantification Results from LIF Visualization: Heavier drug and lower heating during the last 10 mins.

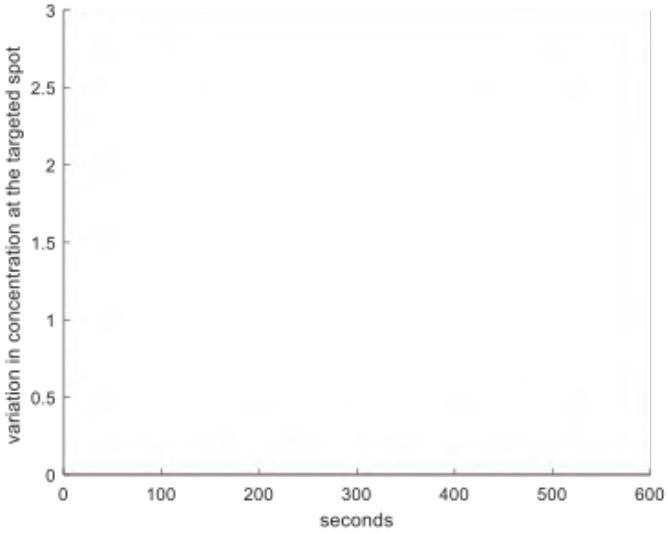

Figure 3.35: Pixel Intensity Quantification Results from LIF Visualization: Lighter drug and center heating during the first 10 mins.

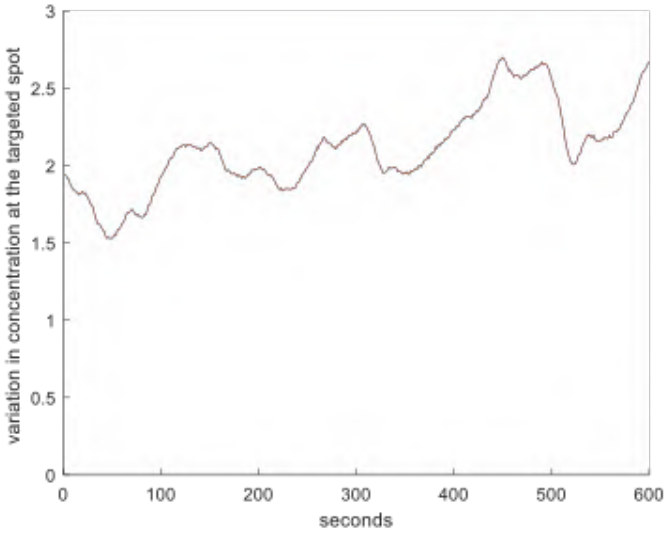

Figure 3.36: Pixel Intensity Quantification Results from LIF Visualization: Lighter drug and center heating during the last 10 mins.

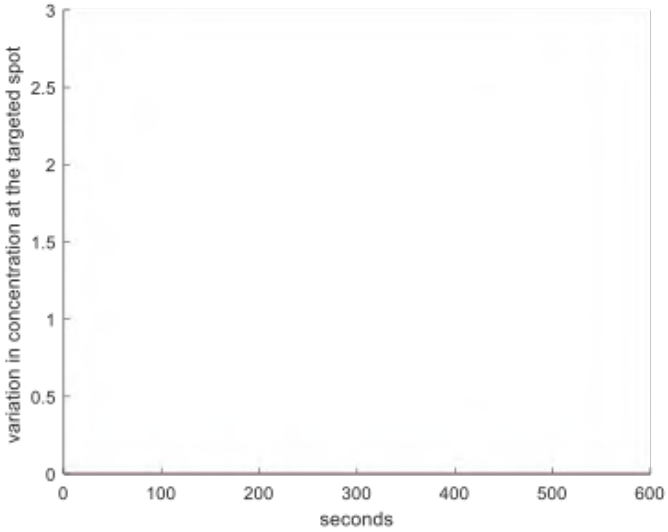

Figure 3.37: Pixel Intensity Quantification Results from LIF Visualization: Lighter drug and lower heating during the first 10 mins.

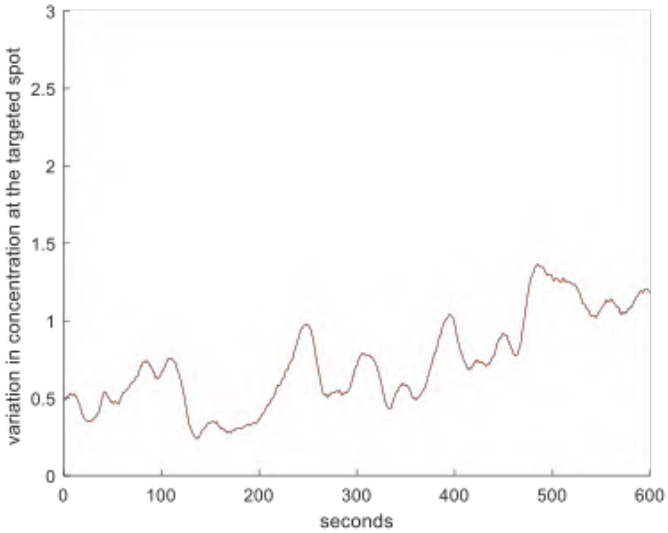

Figure 3.38: Pixel Intensity Quantification Results from LIF Visualization: Lighter drug and lower heating during the last 10 mins.

Heating Method	0-10 mins	40-50mins
Lighter drug, center heating	0	In the range of 1.4-2.6
Lighter drug, lower heating	0	In the range of 0.4-2.4
Heavier drug, center heating	0	0
Heavier drug, lower heating	0	In the range of 0.5-3

Table 3.1: Maximum Pixel Intensity in Each Heating Method

Computational Analysis (MATLAB/FEATool Multiphysics) (Tool:FEATool Multiphysics v1.11)

Both velocity profiles from experimental measurements and simulations are summarized in Figure 3.39 to 3.74 below. Velocity profiles at t = 2.5 min, 5 min, and 7.5 min from experimental measurements as well as T = 0.009, 0.0185, and 0.037 (equivalent as t = 45 s, 1.5 min, and 3 min) from numerical simulations are displayed. All the variables were non-dimensionalized with respect to the parameters described in the material and method section. Clearly, flow profile developed and became stabilized much faster in numerical simulations compared with experiments. This was because the experiments were conducted in 3D and numerical simulations were performed in 2D. However, the results are consistent in either method in terms of the velocity magnitude, flow direction, and movements of the center of the circulation. Therefore, numerical simulation method that was developed in this study could potentially be used in place of experiments for any future studies.

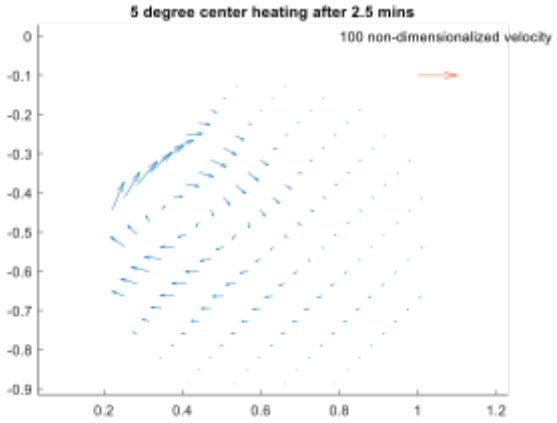

Figure 3.39: $\delta T = 5Celsius$ center heating (experimental results) at 2.5 min

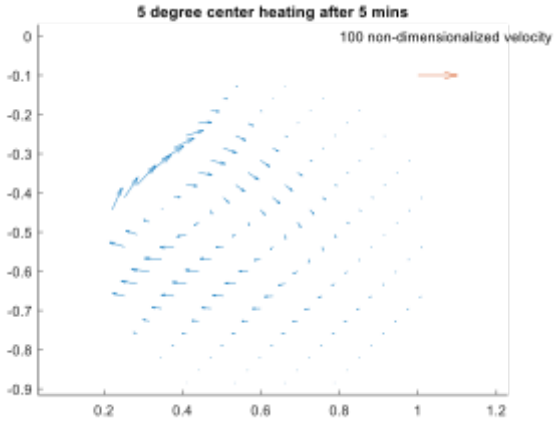

Figure 3.40: $\delta T = 5Celsius$ center heating (experimental results) at 5 min

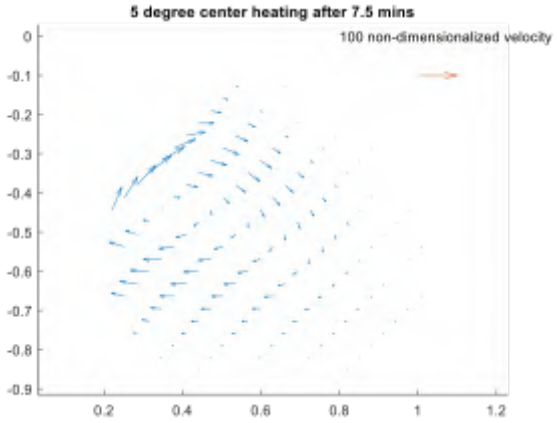

Figure 3.41: $\delta T = 5Celsius$ center heating (experimental results) at 7.5 min

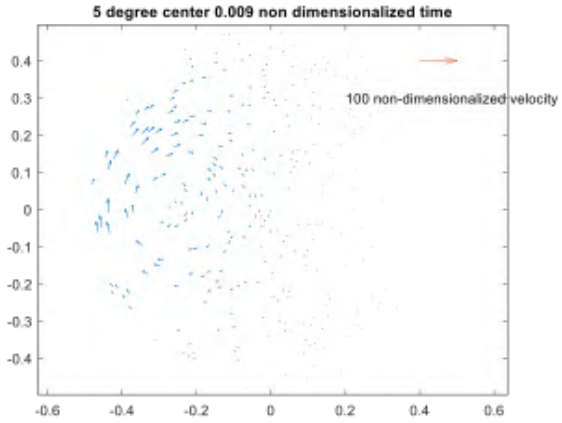

Figure 3.42: $\delta T = 5Celsius$ center heating (simulation results) at t=0.009

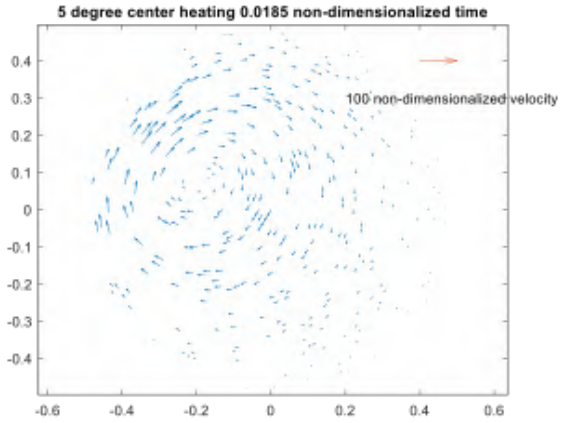

Figure 3.43: $\delta T = 5Celsius$ center heating (simulation results) at t= 0.0185

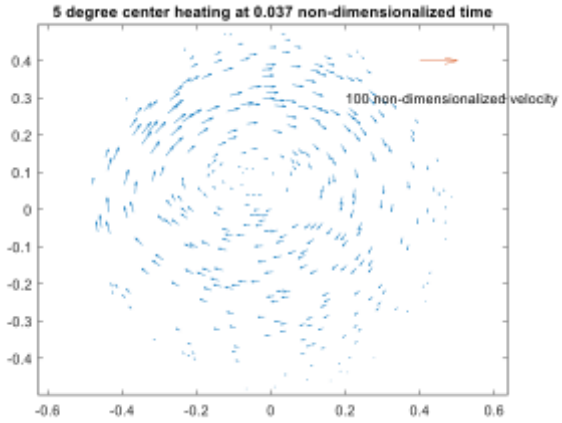

Figure 3.44: $\delta T = 5Celsius$ center heating (simulation results) at t = 0.037

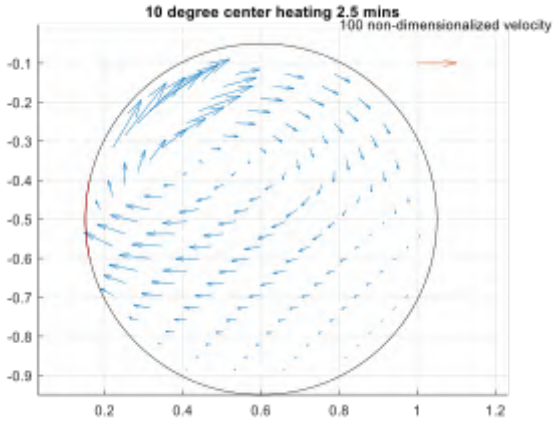

Figure 3.45: $\delta T = 10 Celsius$ center heating (experimental results) at 2.5 min

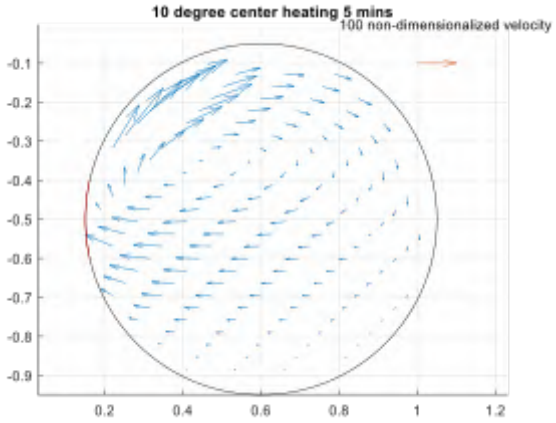

Figure 3.46: $\delta T = 10 Celsius$ center heating (experimental results) at 5 min

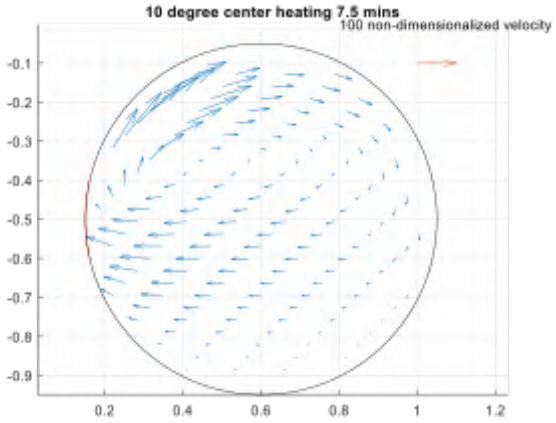

Figure 3.47: $\delta T = 10 Celsius$ center heating (experimental results) at 7.5 min

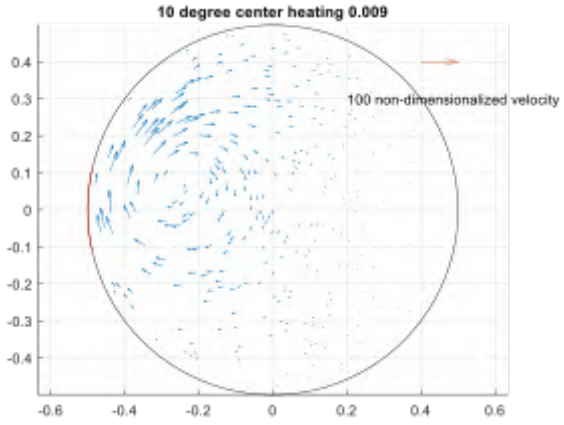

Figure 3.48: $\delta T = 10 Celsius$ center heating (simulation results) at t=0.0009

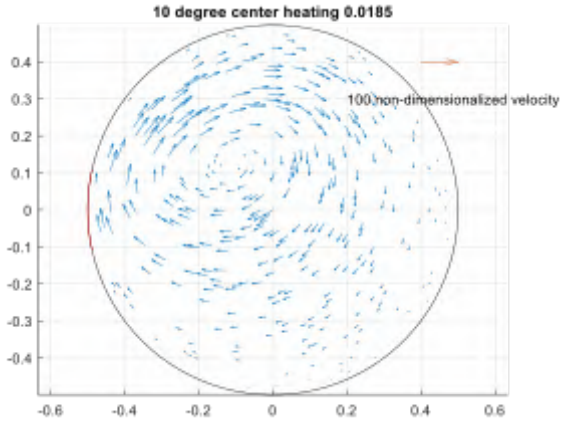

Figure 3.49: $\delta T = 10 Celsius$ center heating (simulation results) at t=0.00185

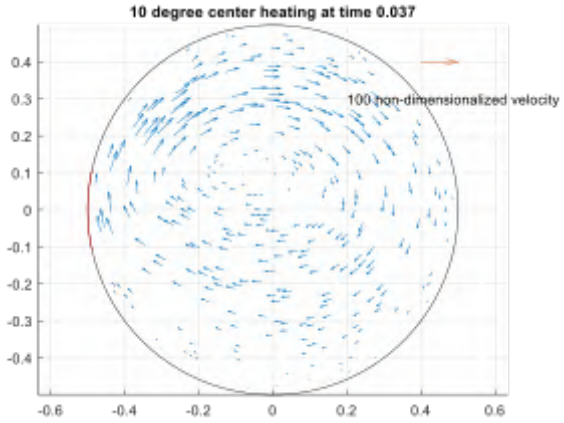

Figure 3.50: $\delta T = 10 Celsius$ center heating (simulation results) at t=0.0037

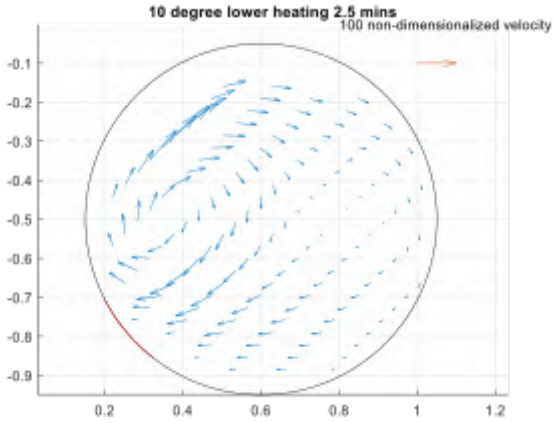

Figure 3.51: $\delta T = 10 Celsius$ lower heating (experimental results) at 2.5 min

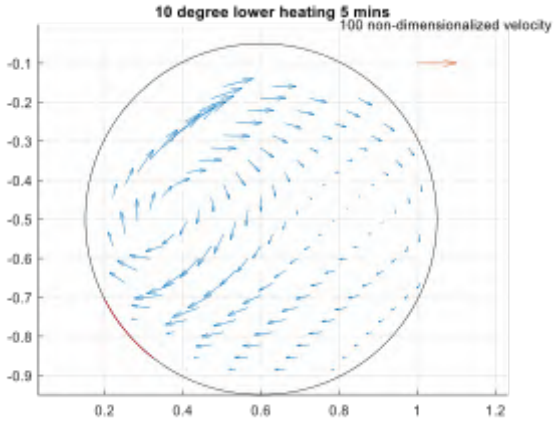

Figure 3.52: $\delta T = 10 Celsius$ lower heating (experimental results) at 5 min

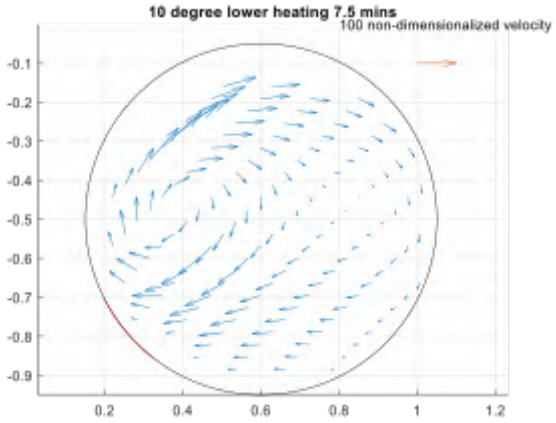

Figure 3.53: $\delta T = 10 Celsius$ lower heating (experimental results) at 7.5 min

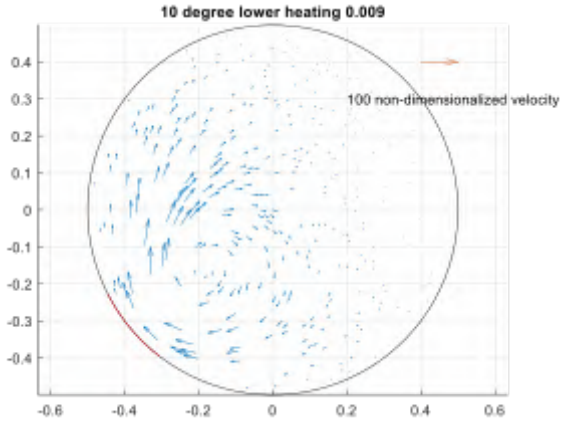

Figure 3.54: $\delta T = 10 Celsius$ lower heating (simulation results) at t=0.0009

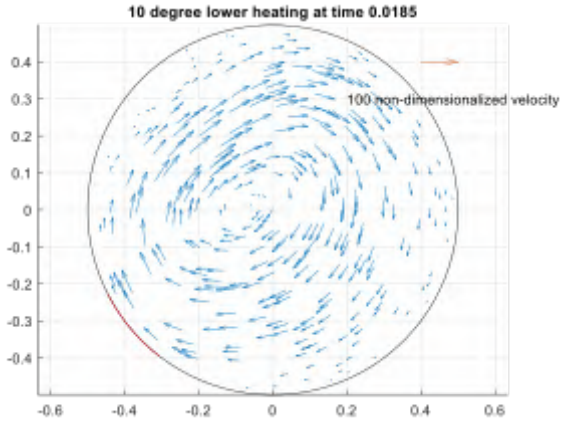

Figure 3.55: $\delta T = 10 Celsius$ lower heating (simulation results) at t=0.00185

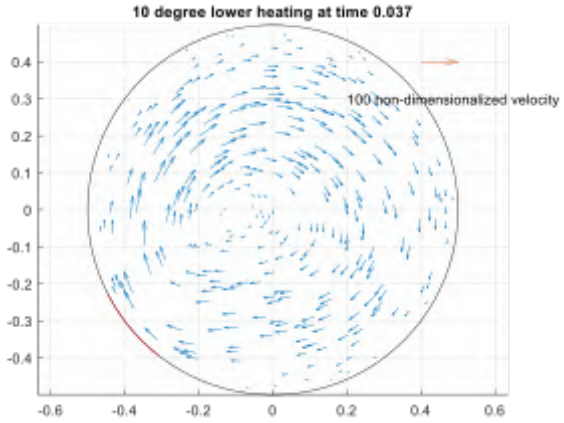

Figure 3.56: $\delta T = 10 Celsius$ lower heating (simulation results) at t=0.0037

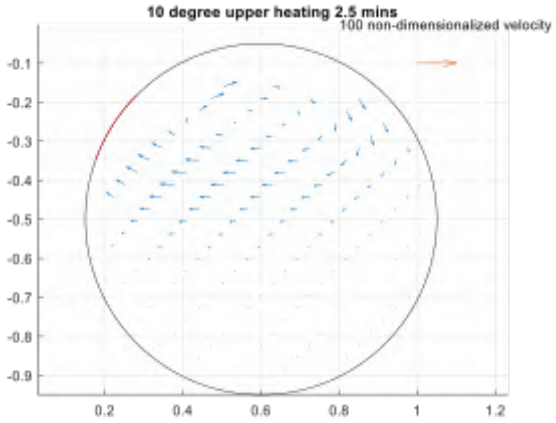

Figure 3.57: $\delta T = 10 Celsius$ upper heating (experimental results) at 2.5 min

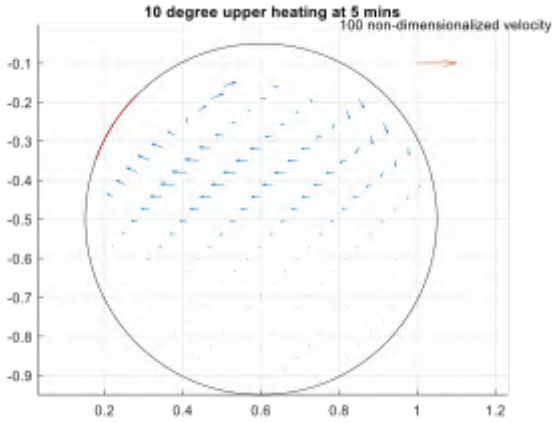

Figure 3.58: $\delta T = 10 Celsius$ upper heating (experimental results) at 5 min

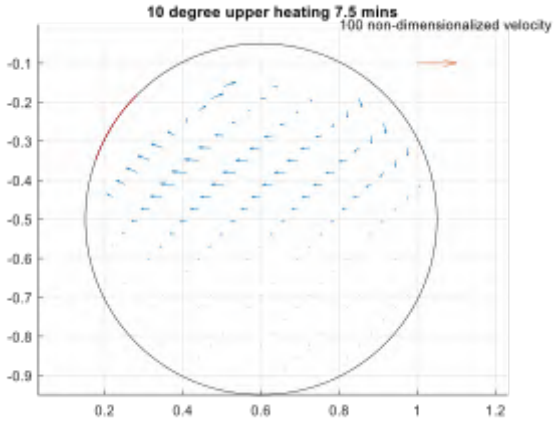

Figure 3.59: $\delta T = 10 Celsius$ upper heating (experimental results) at 7.5 min

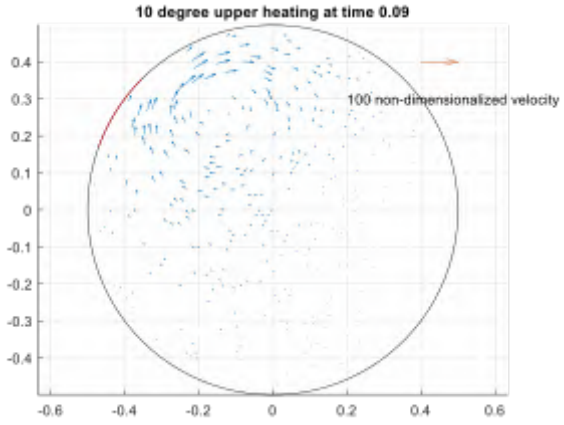

Figure 3.60: $\delta T = 10 Celsius$ upper heating (simulation results) at t=0.009

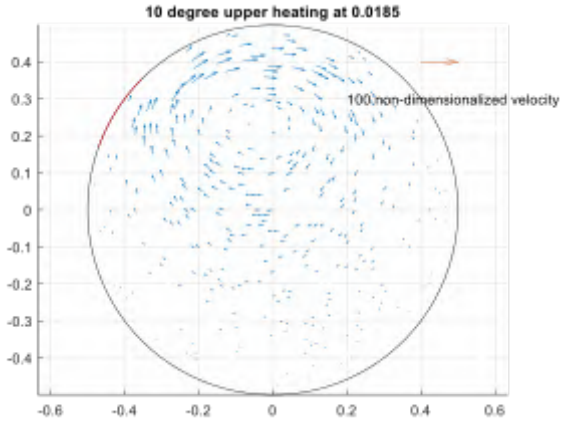

Figure 3.61: $\delta T = 10 Celsius$ upper heating (simulation results) at t=0.0185

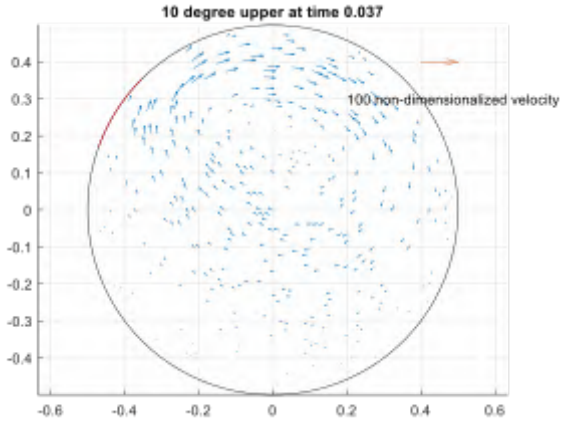

Figure 3.62: $\delta T = 10 Celsius$ upper heating (simulation results) at t=0.037

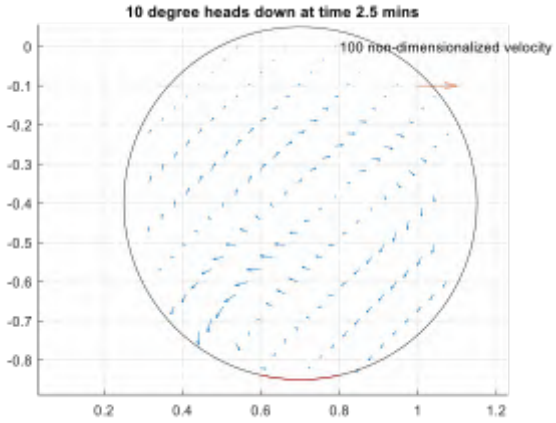

Figure 3.63: $\delta T = 10 Celsius$ heads-down heating (experimental results) at 2.5 min

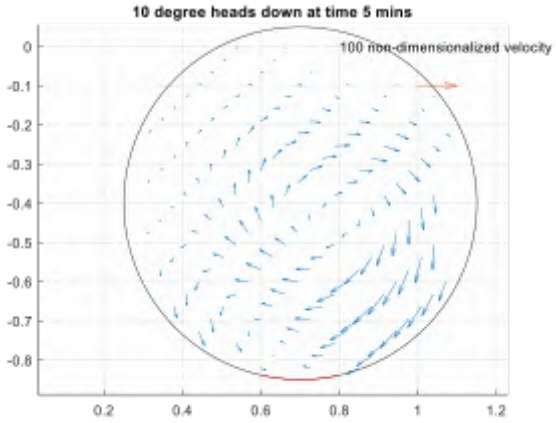

Figure 3.64: $\delta T = 10 Celsius$ heads-down heating (experimental results) at 5 min

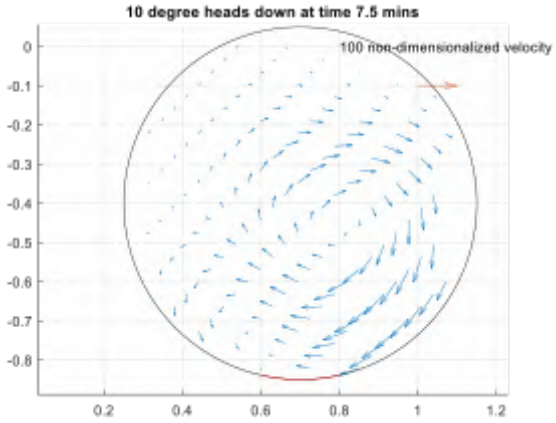

Figure 3.65: $\delta T = 10 Celsius$ heads-down heating (experimental results) at 7.5 min

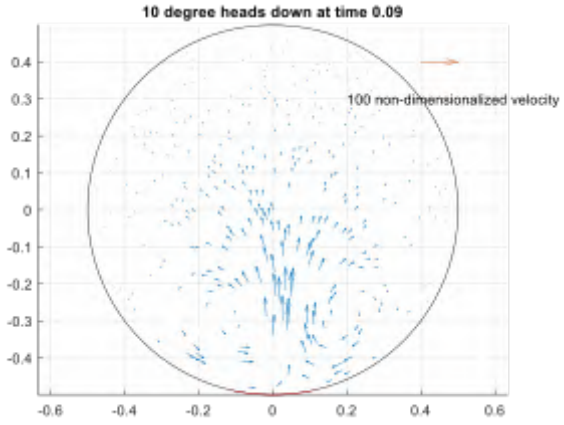

Figure 3.66: $\delta T = 10 Celsius$ heads-down heating (simulation results) at t = 0.009

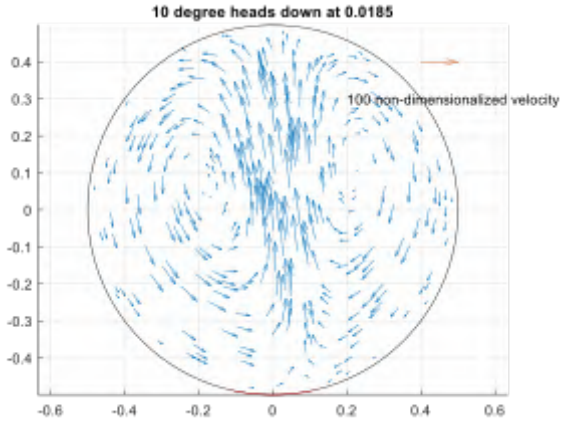

Figure 3.67: $\delta T = 10 Celsius$ heads-down heating (simulation results) at t = 0.0185

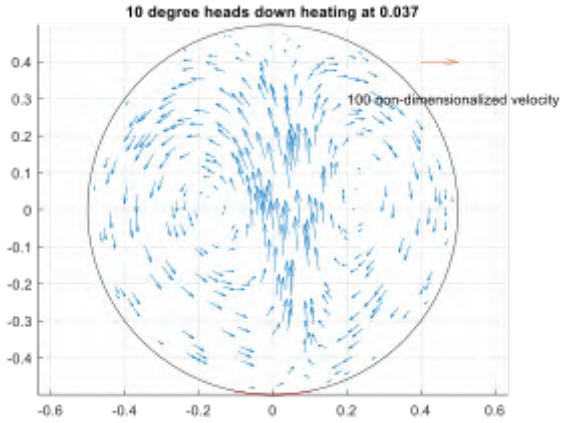

Figure 3.68: $\delta T = 10 Celsius$ heads-down heating (simulation results) at t = 0.037

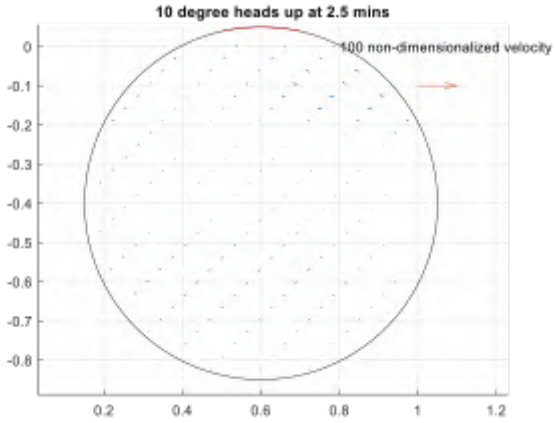

Figure 3.69: $\delta T = 10 Celsius$ heads-up heating (experimental results) at 2.5 min

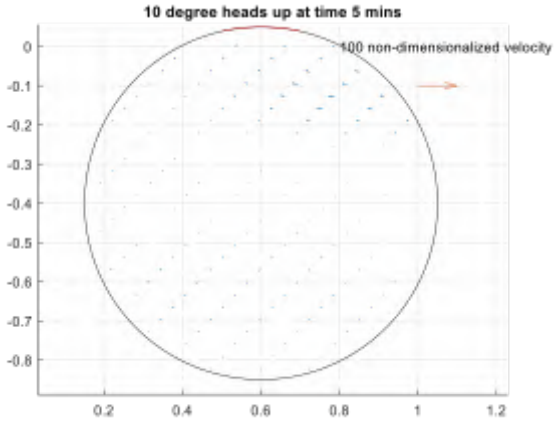

Figure 3.70: $\delta T = 10 Celsius$ heads-up heating (experimental results) at 5 min

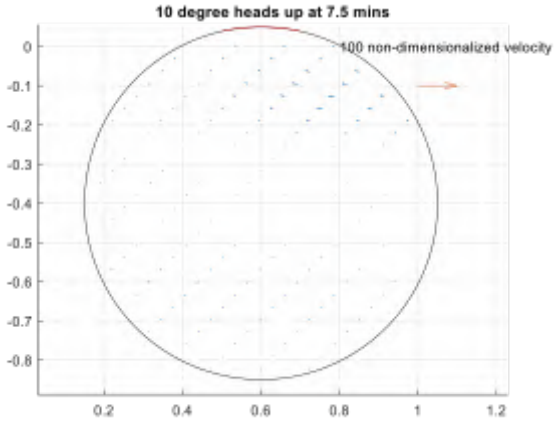

Figure 3.71: $\delta T = 10 Celsius$ heads-up heating (experimental results) at 7.5 min

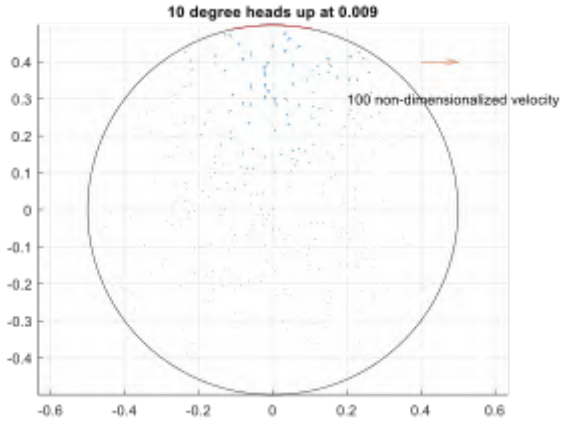

Figure 3.72: $\delta T = 10 Celsius$ heads-up heating (simulation results) at t=0.009

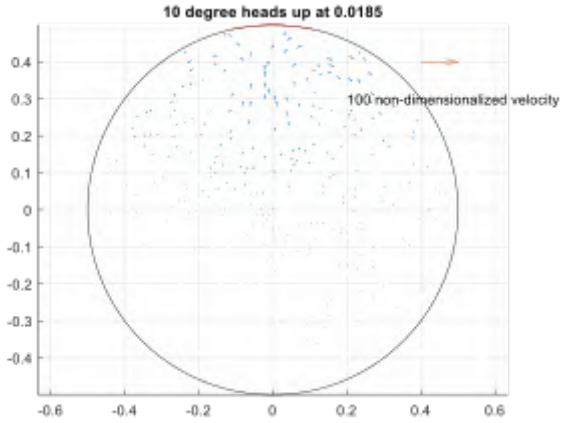

Figure 3.73: $\delta T = 10 Celsius$ heads-up heating (simulation results) at t=0.0185

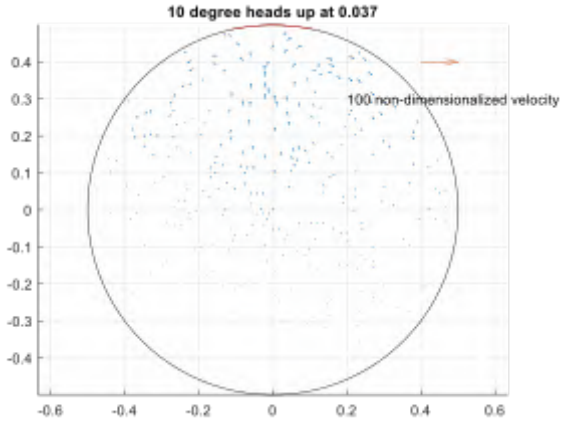

Figure 3.74: $\delta T = 10 Celsius$ heads-up heating (simulation results) at t=0.037

3.4 Discussion

Dimensional Analysis

To understand the physical properties that are relevant, a dimensional analysis was performed. The following parameters are important in describing the physical properties in this experiment and their physical meanings are summarized in Table 3.2

$$f(L, g, \beta, \delta T, \rho, \mu, C_p, U, k) = 0$$

Relevant physical properties for dimensional analysis:
L : characteristic length (diameter of the eyeball, length of heat source, etc) = [L]
g : gravitational acceleration = $[L][T]^{-2}$
β :volumetric thermal expansion coefficient = $[\Theta]^{-1}$
δT: temperature difference = $[\Theta]$
ρ : density = $[M][L]^{-3}$
μ : viscosity = $[M][L]^{-1}[T]^{-1}$
C_p : specific heat = $[L]^2[T]^{-2}[\Theta]^{-1}$
U : velocity = $[L][T]^{-1}$
k : thermal conductivity = $[M][L][T]^{-3}[\Theta]^{-1}$
M, L, Θ, T : fundamental dimensions, [M] for mass, [L] for length, [T] for time, $[\Theta]$ for temperature

There are nine variables and four fundamental dimensions. According to the Buckingham's Pi Theorem, five dimensionless groups are expected:
They are:
$\Pi 1$, Peclet number, which is a measure of the relative importance of convection versus diffusion:

$$\Pi 1 = \frac{L\rho C_p U}{k} = Pe$$

$\Pi 2$, thermal expansion with respect to temperature change:

$$\Pi 2 = \delta T \beta$$

Π3, Rayleigh number, associated with buoyancy-driven flow and can be regarded as a measure of the driving forces of natural convection. The magnitude of Rayleigh number is a good indication as to whether the natural convection boundary layer is laminar or turbulent:

$$Ra = \frac{C_p \rho^2 g \beta \delta T L^3}{k\mu} = Ra$$

Π4 Prandtl number, which is a dimensionless quantity that puts the viscosity of a fluid in correlation with the thermal conductivity. It therefore assesses the relation between momentum transport and thermal transport capacity of a fluid ((Ganji and Kachapi, 2015)):

$$\Pi 4 = \frac{C_p \mu}{k} = Pr$$

Π5 The Reynolds number is the ratio of inertial forces to viscous forces, it is usually used to determine whether a fluid is in laminar or turbulent flow:

$$\Pi 5 = \frac{\rho U L}{\mu} = Pr$$

Since Peclet number, Rayleigh number, and Prandtl number are most relevant to a natural convection problem, the actual values of these number for each of the three types of liquid at 21 Celsius were calculated and summarized in Table 3.3 below.

Solution	$C_p(KJ/kg.K)$	$\mu(mPas)$	$k(W/m \cdot K)$	$\rho(kg/m^3)$	$\beta(10^{-4}/K)$
Water	4.213	1.731	0.5642	999.9	2.07
Glycerol/Water Mixture (1:5)	3.826	3.282	0.4985	1051.5	3.18
Glycerol/Water Mixture (2:5)	3.610	4.647	0.4665	1077.9	3.91

Table 3.2: Corresponding physical property values for each solution

The Peclet number serves as the Reynolds number counterpart for thermal energy transfer. It represents the ratio of the convection and diffusion fluxes in a flow. In our study, the Peclet number is on the scale of 10^2, which indicates that convection plays a stronger role compared to diffusion in the heat/fluid transport phenomena.

Solution	Pe	Pr	Ra
Water	168	7.74	6,344
Glycerol/Water Mixture (1:5)	181	13.48	4,316
Glycerol/Water Mixture (2:5)	187	21.68	5,616

Table 3.3: Values of dimensionless numbers in each scenario (Note: L = 5 mm and delta T = 5 for the characteristic length and temperature difference in Rayleigh number calculation)

It is also worth noting that the Prandtl number that multiplies the Reynolds number is Peclet number.

The Prandtl number can be derived by introducing the concept of thermal diffusivity (α), which describes the rate of temperature spread through a material. It measures the ability of a material to conduct thermal energy relative to its ability to store thermal energy. Thermal diffusivity is calculated from the thermal conductivity and the heat thermal capacity as given below:

$$\alpha = \frac{k}{\rho C_p}$$

where k is thermal conductivity, ρ is material density, and C_p is specific heat capacity of materials. Therefore, using the idea of thermal diffusivity, the expression for Prandtl number is given below:

$$Pr = \frac{C_p \mu}{k} = \frac{\nu}{\alpha}$$

where ν is kinematic viscosity, which is the ratio of dynamic viscosity to density.

Therefore, Prandtl number measures the significance of diffusion of momentum relative to that of heat transfer. The larger the Prandtl number, the thicker will be the momentum boundary layer compared to the thermal boundary layer. In this study, Prandtl number is in the range of 10-20, indicating the momentum transport plays a stronger role compared with heat transport.

The magnitude of Rayleigh number is a good indication as to whether the natural convection boundary layer is laminar or turbulent. For a Rayleigh number in the range of 10^3 to 10^4, the natural convection boundary layer is laminar. Based on the value of Peclet number and Prandtl number, it is possible to deduce that heat is primarily transported via flow convection: fluid that is heated up as the heat source

carries heat and transports the heat with the flow. The flow circulation continuously brings colder solution to the heat source. Eventually, the entire solution inside the eye model is heated up, at which point circulation stops

Baroclinic Torque and Flow Circulation

As mentioned in the previous section, flow circulation patterns were observed regardless of heating position or temperature difference. To understand the formation of the flow circulation, it is useful to refer to the concept of baroclinic torque. Baroclinic torque is the source of vorticity, which arises from unequal acceleration as a result of miss-aligned density gradient and pressure gradient, as shown in the equation for the transport of vorticity:

$$\frac{D\omega}{Dt} = -\omega(\nabla \cdot V) + \frac{\nabla\rho \times \nabla p}{\rho^2} + (\omega \cdot \nabla)V + \frac{\nabla^2\omega}{Re}$$

where term 1 on the right-hand side represents the effects of expansion on the vorticity field, term 2 is the baroclinic torque, term 3 describes vortex stretching, and term 4 describes the effects of viscous diffusion on vorticity distribution. For the flow fields in our study, term 2 is the only reason that vortices are formed. The baroclinic torque is the largest when the pressure gradient is perpendicular to the density gradient. The lighter fluid will be accelerated faster than the heavier fluid, resulting in a shear layer, and thus generating vorticity. In our case, this variation in fluid density is caused by thermal heating, and vorticity is generated as a result of density gradient that is unparalleled with pressure gradient.

Insights from Numerical Simulation Results

To better understand flow activity around the heat source, we refer to the numerical study conducted by (Shu and Pop, 1997) Their numerical solution investigates the natural convection from inclined wall plumes that arise from a line thermal source imbedded at the leading edge of an adiabatic plate with arbitrary tilt angle between 0 and $\pi/2$, and embedded in a fluid-saturated porous medium. The physical model is demonstrated in Figure 3.75 below.

In our experimental setup, the contact area between the heat source and the eye model is very small. As we are mostly interested in understanding the fluid motion around the heat source, the physical model can thus be transformed into the study of

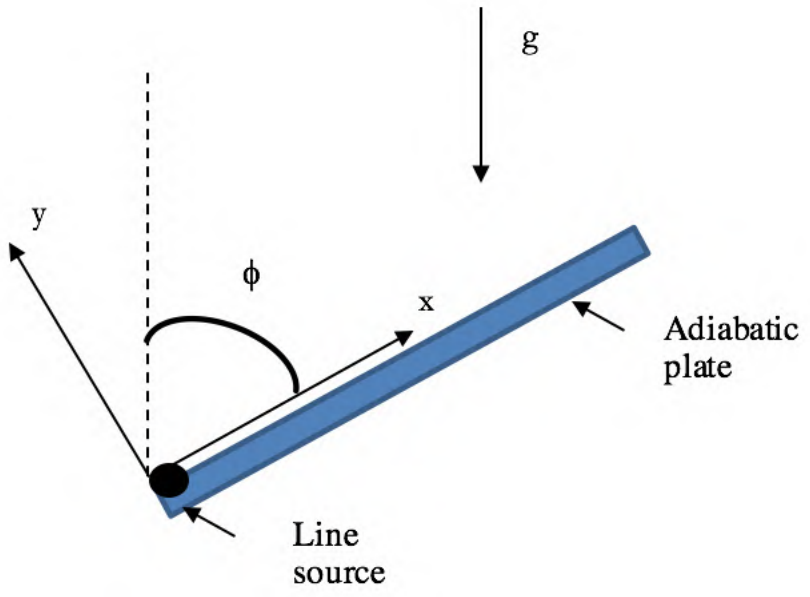

Figure 3.75: Physical model setup and coordinate system in (Shu and Pop, 1997)

natural convection from inclined wall plumes that arise from a line thermal source imbedded at the leading edge of a short adiabatic plate (5 mm) with a title angle of 0. This transformation is demonstrated in Figure 3.76 below.

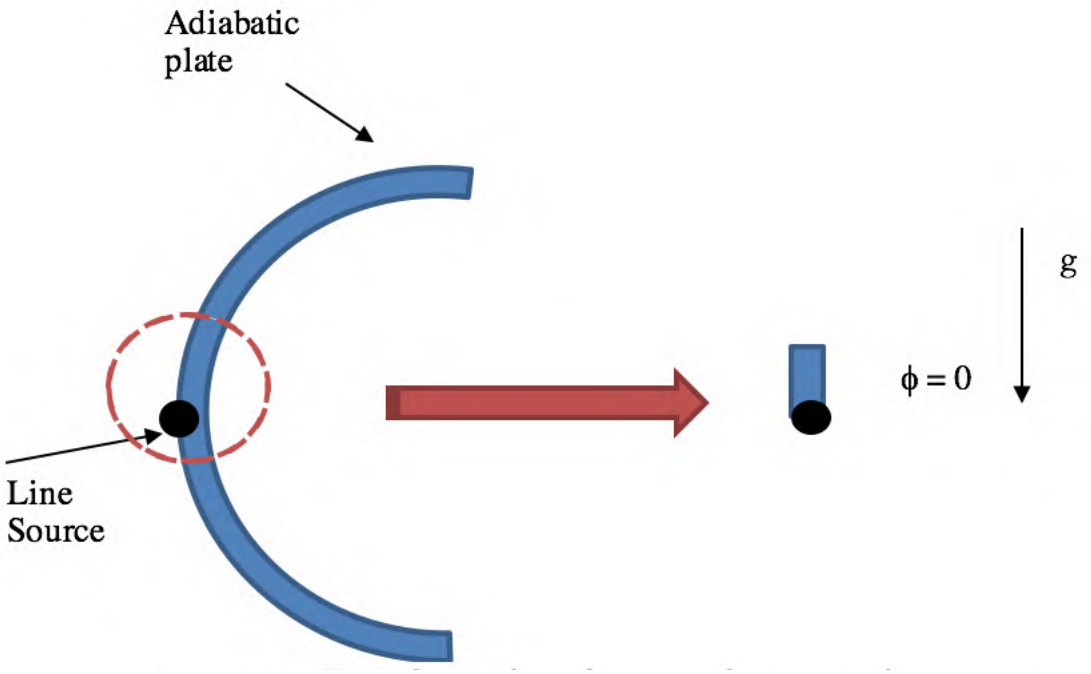

Figure 3.76: Transformation of the physical model in our study

The governing equations for this problem are set up as follows:

$$\frac{\partial u}{\partial x} + \frac{\partial v}{\partial y} = 0$$

$$\frac{\partial u}{\partial x} = \frac{gK\beta}{\nu}(\frac{\partial T}{\partial y}cos\phi - \frac{\partial T}{\partial x}sin\phi)$$

$$u\frac{\partial T}{\partial x} + v\frac{\partial T}{\partial y} = \alpha\frac{\partial^2 T}{\partial y^2}$$

where α is the effective thermal diffusivity of the porous medium, K is permeability of the porous medium, T is temperature, u,v are velocity components in the x, y directions, β is coefficient of thermal expansion, ϕ is the tilt angle measured from the vertical, and x,y are coordinates along and normal to the plate.

In fluid mechanics, permeability measures the ability of a porous material to allow fluids to pass through it. Since the only fluid medium in our study is either pure water or uniform water/glycerol mixture, it is thus assumed a 100% permeability. Figure 3.77 below shows one of the numerical simulation results: velocity profile for $R_a = 10^3$. The Rayleigh number here is defined as

$$R_a = \frac{gK\beta\delta T x}{\alpha\nu}$$

For a 100% permeability in our case,R_a is then modified to

$$R_a = \frac{g\beta\delta T x^3}{\alpha\nu}$$

where x is the effective contact length of the heating piece (x 5 mm). According to Table 3.3, for $\delta T = 5$ Celsius, Rayleigh numbers are 4 $\times 10^3$ for glycerol/water (1:5) mixture, and 5 $\times 10^3$ for glycerol/water (2:5) mixture. Both are on the order of magnitude of 10^3. It is seen from Figure 3.77 that if y (perpendicular to adiabatic plate) is fixed, then u velocity increases as it moves further in the longitudinal direction. For a fixed x (longitudinal along the adiabatic plate), u velocity drops as it moves further away into the fluid along the perpendicular direction. This is consistent with our observations from pathline visualizations.

As mentioned earlier, the contact length between heat source and the eye model was approximately 5 mm, and thus the characteristic fluid volume near the heat

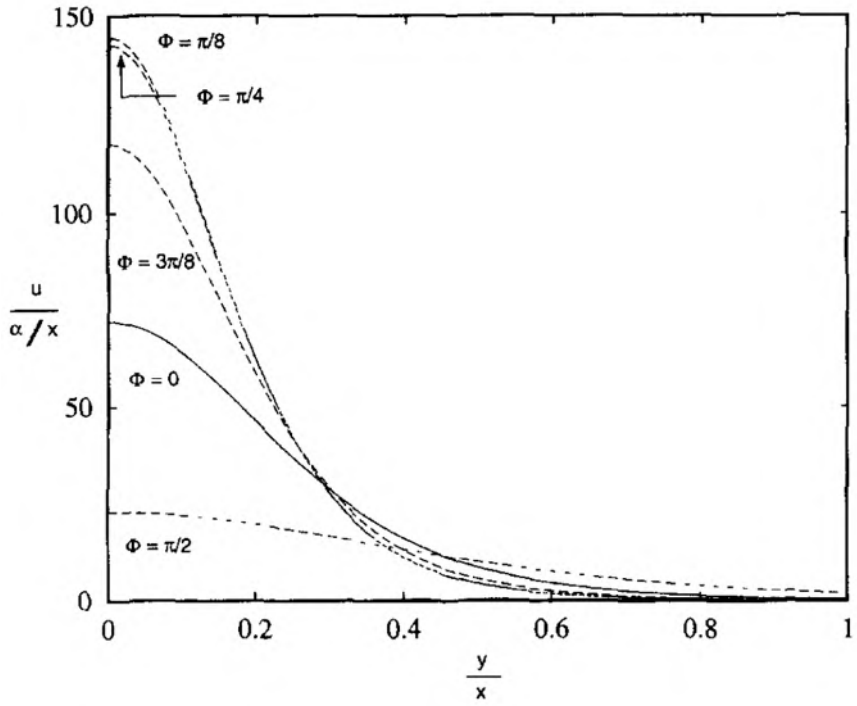

Figure 3.77: Representative velocity profiles for $R_a = 10^3$

source was determined to be $5^3 mm^3$. Within this volume, a quick calculation of u velocity can be performed based on information given in Figure 3.77. For example, in glycerol/water (1:5) mixture, $\alpha = 0.12 mm^2/s$. For y = 1 mm and x = 5 mm, and $\phi = 0$:

$$\frac{u}{\alpha/x} = 50$$

$$u = 50 \times 0.12/5 mm/s = 1.2 mm/s$$

This is approximately on the same order of magnitude compared with the actual maximum velocity reading from our PIV analysis (Table 3.4).

Heating Method	Maximum Velocity (mm/s)
δT = 5-degree center heating	0.2 mm/s
δT = 10-degree center heating	0.4mm/s
δT = 10-degree lower heating	0.4 mm/s
δT = 10-degree upper heating	0.1 mm/s

Table 3.4: Maximum Velocity Reading Near the Wall from PIV Analysis

Summary

In this chapter, facilitating drug mixing in the eye using thermal-driven method was explored experimentally and the result was successful. For a person sitting in the upright position, applying a heat source (at least 5 Celsius greater than the eye temperature) to the lower position of his/her eye can active a strong fluid mixing in the entire vitreous chamber. Moreover, this method requires the minimal amount of efforts from patients.

Chapter 4

CONCLUSION AND FUTURE WORKS

In this study, we explored two methods for inducing drug mixing into the eye after an intravitreal injection:
1) Motion-driven method: introducing lateral movements to the eye;
2) Thermal-driven: applying heat source to the eye at various heating positions.

The thermal-driven method appears to be more effective in agitating fluid mixings in the eye. It is also more flexible in dealing with the density variance among different individuals as well as age groups. In addition, it also provides an alternative to having a cooling pad in place of a heat source. The idea is the same although direction of fluid circulation will be the opposite in the case of using a cooling pad. Of course, whether the thermal-driven method is safe to be included into future clinical protocols will need more safety investigations. Ultimately, the conclusion we obtained is very insightful in inspiring us to think about possible minimally invasive ways to increase intravitreal injection efficacy.

Apart from intravitreal injections, the study outcome can also be useful for applications in other eye treatment methods, especially for drug-releasing ocular implants. Since the majority of these ocular implants are designed to provide a sustained release of medication for a long period which ranges from months to years, a well-established fluid mixing profile in the eye can certainly help in making sure that the small amounts of drugs being released can effectively reach the target issue and eventually achieve an optimal treatment efficacy.

Looking forward, performing the same experiments using animal eyes will certainly help in understanding the safety features. Based on the observations of important flow parameters from this study, developing numerical simulations to model the thermal-driven mixing profile can also be helpful for obtaining explicit understanding of the governing parameters that affect the flow mixing profile. An eye mask with precision heating ability can also be manufactured and tested to be included as part of the intravitreal injection protocol. Ultimately, we are hoping that the study outcome can inspire researchers and ophthalmologists to pay more attention to the

importance of convective flow in the eye as well as its great potentials in promoting drug mixing in the eye for improved patient care.

BIBLIOGRAPHY

Akinkunmi, Frederick O, David A Jahn, and Nicolas Giovambattista (2015). "Effects of Temperature on the Thermodynamic and Dynamical Properties of Glycerol–Water Mixtures: A Computer Simulation Study of Three Different Force Fields". In: *The Journal of Physical Chemistry B* 119.20, pp. 6250–6261.

Balazs, EA (1993). "Functional anatomy of the vitreous". In: *Duane's Foundation of Clinical Ophthalmology* 1, pp. 1–16.

Balazs, Endre A (1982). "Aging changes in the vitreous." In: *Aging and Human Visual Function.* Pp. 45–57.

Cristancho, Diana M et al. (2011). "Volumetric properties of glycerol+ water mixtures at several temperatures and correlation with the Jouyban-Acree model". In: *Revista colombiana de ciencias quimico-farmaceuticas* 40.1, pp. 92–115.

Del Amo Eva, M et al. (2017). "Pharmacokinetic aspects of retinal drug delivery". In:

Frederick, O, A David, et al. (2015). "Effects of Temperature on the Thermodynamic and Dynamical Properties of Glycerolâ Water Mixtures: A Computer Simulation Study of Three Different Force Fields". In: *Journal of physical chemistry*.

Ganji, Davood Domairry and Sayyid Habibollah Hashemi Kachapi (2015). *Application of nonlinear systems in nanomechanics and nanofluids: analytical methods and applications*. William Andrew.

Gaudana, Ripal et al. (2010). "Ocular drug delivery". In: *The AAPS journal* 12.3, pp. 348–360.

Geroski, Dayle H and Henry F Edelhauser (2000). "Drug delivery for posterior segment eye disease". In: *Investigative ophthalmology & visual science* 41.5, pp. 961–964.

Holz, Frank G, Steffen Schmitz-Valckenberg, and Monika Fleckenstein (2014). "Recent developments in the treatment of age-related macular degeneration". In: *The Journal of clinical investigation* 124.4, pp. 1430–1438.

Kim, Hyuncheol, Shaun B Robinson, and Karl G Csaky (2009). "FcRn receptor-mediated pharmacokinetics of therapeutic IgG in the eye". In: *Molecular vision* 15, p. 2803.

Kummer, Michael P et al. (2007). "Artificial vitreous humor for in vitro experiments". In: *2007 29th Annual International Conference of the IEEE Engineering in Medicine and Biology Society*. IEEE, pp. 6406–6409.

Locke, John C and WR Morton (1965). "Further studies of the viscosity of aspirated human vitreous fluid: with special reference to its use in retinal detachment surgery." In: *Transactions of the American Ophthalmological Society* 63, p. 129.

Maurice, DM and S Mishima (1984). “Ocular pharmacokinetics”. In: *Pharmacology of the Eye*. Springer, pp. 19–116.

Miller, Christina Cruickshank (1924). “The Stokes-Einstein law for diffusion in solution”. In: *Proceedings of the Royal Society of London. Series A, Containing Papers of a Mathematical and Physical Character* 106.740, pp. 724–749.

Milo, Ron and Rob Phillips (2015). *Cell biology by the numbers*. Garland Science.

Moore, EF and RW Davis (1984). “Numerical solutions for steady natural convection in a square cavity”. In: *NASA STI/Recon Technical Report N* 85.

Murthy, Krishna R et al. (2014). “Proteomic analysis of human vitreous humor”. In: *Clinical proteomics* 11.1, p. 29.

Purves, D et al. (2001). “The organization of the nervous system”. In: *Neuroscience. 2nd Edition. Sunderland, MA: Sinnauer Associates Inc*, p. 26.

Scott, Karen S and John S Oliver (1999). “Vitreous humor as an alternative sample to blood for the supercritical fluid extraction of morphine and 6-monoacetylmorphine”. In: *Medicine, science and the law* 39.1, pp. 77–81.

Shu, J-J and Ioan Pop (1997). “Inclined wall plumes in porous media”. In: *Fluid Dynamics Research* 21.4, pp. 303–317.

Stewart, Michael W (2018). “Extended duration vascular endothelial growth factor inhibition in the eye: failures, successes, and future possibilities”. In: *Pharmaceutics* 10.1, p. 21.

Wilson, ME and AW Scott (2013). “How to give intravitreal injections”. In: *EyeNet Mag*.

Yorston, David (2014a). “Anti-VEGF drugs in the prevention of blindness”. In: *Community eye health* 27.87, p. 44.

– (2014b). “Intravitreal injection technique”. In: *Community eye health* 27.87, p. 47.